Fredrik Grøvdal

A Dimensional-Decomposition Approach for Stochastic Scale-Resolving Simulations of Turbulent Reacting Flows

Doctoral Thesis

Fredrik Grøvdal

NTNU
Norwegian University of
Science and Technology

NTNU
Norwegian University of
Science and Technology

NTNU

Fredrik Grøvdal

A Dimensional-Decomposition Approach for Stochastic Scale-Resolving Simulations of Turbulent Reacting Flows

Thesis for the degree of Philosophiae Doctor

Trondheim, November 2018

Norwegian University of Science and Technology
Faculty of Engineering
Department of Energy and Process Engineering

NTNU
Norwegian University of
Science and Technology

Preface

This doctoral thesis was carried out at the Norwegian University of Science and Technology (NTNU) under the supervision of Prof. Terese Løvås and Dr. Sigurd Sannan. The work was performed within the HYCAP project (233722), led by SINTEF Energy Research and funded by the Research Council of Norway performed under the strategic Norwegian research program CLIMIT.

Abstract

High-fidelity and reliable numerical design tools are main keys to the development of novel gas turbines for hydrogen-rich fuels. However, state-of-the-art simulation tools for the most part only give a bulk approximation to the fluid flow and combustion processes. Direct Numerical Simulation (DNS) is a method that can provide detailed information about flow structures and turbulence-chemistry interactions but is computationally unaffordable for any large-scale applications. Numerical design tools that provide the capability of detailed predictive modeling of mixing and reaction at the needed scale and at a low computational cost are therefore highly in demand.

A unique new methodology for modeling and simulation of turbulent reactive flows is developed, relying on the dimensional-decomposition approach, decomposing 3D into 3×1D, and is further motivated, discussed and investigated. The model is developed on the basis of a 3D formulation of the Linear Eddy Model (LEM), thereby its name LEM3D. It involves three fully resolved orthogonally intersecting 1D LEM domains and their re-coupling, intended to capture 3D flow properties. As in the LEM framework, advection is treated in a Lagrangian manner with displacements of fluid cells, tree-dimensional advective turbulent stirring by one-dimensional stochastic rearrangements, and molecular mixing and chemical reactions are solved directly. LEM3D is currently implemented as a post-processing tool for an initial RANS simulation or experimental data. In this hybrid approach, LEM3D complements RANS/experiments with unsteadiness and small-scale resolution in a computationally efficient manner, regarding its fully resolved resolution. In the present modeling approach, mean-flow information from RANS/experiment provides model input to LEM3D, which returns the scalar statistics needed for more accurate mixing and reaction calculations.

Three different iteration procedures, a breadth-first search, a checker-board algorithm and a naive approach, as well as parameters of the model framework are examined and tested for sensitivity towards the result. It is found that LEM3D is able to show additional details compared to the RANS simulation with low computational cost, in comparison to traditional DNS or LES simulations. A drawback for the additional detail is that the results deviate from the average-profiles prescribed. The artifacts of the models, strongly linked to the dimensional-decomposition approach and the need for re-coupling are thoroughly investigated.

To demonstrate the RANS-LEM3D model, the hybrid model is applied to various configurations with equal variation in success. A thorough investigation based on a flame front in a freely propagating laminar premixed flame for the approach is conducted, concluding that the flame stabilizes at the upstream face of the initial

solution when both the advectional and auxiliary re-couplings are activated.

Capabilities of the model is demonstrated through simulations of both a lifted and attached turbulent N_2-diluted hydrogen jet flame in a vitiated co-flow of hot products from lean H_2/air combustion. The dependence of lift-off heights and flame structure on iteration schemes and model parameters are investigated in detail, along with other characteristics not available from RANS alone, such as the instantaneous and detailed species profiles and small scale mixing. Furthermore, results from LEM3D simulations of a vitiated co-flow burner are thoroughly examined adding a detailed discussion of the model artifacts.

The potential benefit of the hybrid model, once validated, compared to a corresponding DNS, is the huge cost saving factor of solving the reactive-diffusive equations on 1D domains, rather than in a full 3D computation. To leading order, the computational cost saving is estimated to be $\sim 10^4$ for the application to the lifted turbulent N_2-diluted jet flame. The present work has demonstrated that LEM3D, as a post-processing tool to RANS within the hybrid RANS-LEM3D framework, complements RANS with unsteadiness, detailed information on the flame structure, small-scale mixing of reactive flows and fine-scale resolution of scalar concentration profiles. Finally, the main finding of the present work is that the auxiliary coupling introduces an unacceptable amount of artificial diffusion. A suggestion for future work is given based on the Péclet number.

Extensions to the model framework, with respect to the the previous work by Sannan et al. [87, 88] and Weydahl et al. [108, 109], includes implementation of finite rate chemistry, parallel computing, re-gridding, mass-fluxes, wafer-tracking, breadth-first iteration scheme, minimization of deviations by least squares and post-processing tools.

Acknowledgements

Impostor syndrome: "Am I only good at deceiving others into thinking I am more intelligent than I actually am?" A lot of frustration and effort is put into this thesis. Numerous of scientists got lost in the mysteries of turbulence. I am grateful to be one among them; working with turbulent reacting flows for the past 3+ years. Often I've felt I'm not the right man for the job.

Special thanks to my supervisor Prof. Terese Løvås, for giving me the chance to work as a Ph.D-student in the ComKin group, always being encouraging, progressing the research forward and believing in the ability of me as her student.

I also would like to thank my co-supervisor, Dr. Sigurd Sannan, for all the delightful, challenging and helpful discussions we've had and for sharing his vast knowledge of research work. I appreciate all his contributions of time, ideas and funding to make my PhD experience productive and stimulating.

Thanks also to Dr. Alan Kerstein, who was available for conceptual discussions of the model and turbulence in general during my time as a Ph.D.-student.

I would like to express my gratitude to Prof. Jyh Yuan Chen and his students at the Combustion Modeling Lab at University of California, Berkeley, for including me in their research group during my stay August 2016 - July 2017.

My unlimited gratitude goes to my colleges and fellow scientists at NTNU: Christoph Meraner, Karl Oskar Bjørgen, 郭宁 (Ning Guo), Kathrin Weber, David Emberson, Jonas Krüger, Jingyuan Zhang and Vladimir Krivopolianskii. The collaborative and friendly environment where everyone can be the others' hand and resource have made my Ph.D. experience most fulfilling. Tian Li; I admire your knowledge and persistence, working day and night, always open for any questions, even as dumb it might be, you'll stay and explain.

I would like to thank my friends for (constantly) reminding me that there is life beyond work.

Thanks to my family for their unconditional love and for all their time whenever my responsibilities got too many, my efforts did not suffice and my time ran out.

I thank my fiancée, Pia, for always staying by my side during my ups and downs in the past three years. Your unending patience, company and encouragement was what provided me with stability during the past three years apart.

Lastly, thank you to the people I did not name, those that I've worked with and learned so much from over the years, and those whose countless hours of research I relied upon.

Scientific contributions

Selected articles included in this thesis

This thesis is based on the work presented in the following articles, which are referred in the text by Roman numerals:

I. Fredrik Grøvdal, Sigurd Sannan, Jyh-Yuan Chen, Alan R. Kerstein, Terese Løvås.
Three-dimensional Linear Eddy Modeling of a Turbulent Lifted Hydrogen Jet Flame in a Vitiated Co-flow.
Accepted for publication in Flow, Turbulence and Combustion (27.07.2018)

II. Fredrik Grøvdal, Sigurd Sannan, Jyh-Yuan Chen, Terese Løvås.
A parametric study of LEM3D based on validation with a Turbulent Lifted Hydrogen Jet Flame in a Vitiated Co-flow.
(Submitted to Combustion Science and Technology 04.07.2018)

III. Fredrik Grøvdal, Christoph Meraner, Sigurd Sannan, Tian Li, Terese Løvås.
Dimensional Decomposition of Turbulent Reacting flows.
(Prepared for submission to Combustion and Flame)

The author's contribution to selected publication

The articles listed above are co-authored. The authors have performed the following work for each publication:

I. The first author performed the literature research and implemented parallelization, re-gridding, mass-fluxes and optimized the least-square method for variable density flows into the in-house LEM3D code. Dr. Sannan conducted the ANSYS Fluent results provided to LEM3D and implemented chemistry into the in-house code, previously assuming constant-density. The findings were interpreted and summarized jointly with the co-authors through discussions in UC Berkeley, California and NTNU, Trondheim. The first author wrote the article, but all co-authors provided valuable input on the final version of the article.

II. The literature research and implementation of the new iteration scheme was conducted and suggested by the author. All LEM3D simulations were ran by the author, while the ANSYS Fluent simulations, and their sensitivities, providing initial fields for the simulations was conducted

by Dr. Sannan. Prof. Chen conducted the ignition delays with an in-house code at UC Berkeley. The authors of the article acknowledge the contributions made by Dr. Kerstein for providing valuable and constructive input. The publication was written by the author and critically reviewed by all co-authors.

III.   The literature research and LEM3D modeling work was conducted by the main author, excluding the LOGEresearch(TM) simulations which was conducted by Dr. Li. Valuable support was given by Christoph Meraner, in particular for the creation of the figures and development of the Péclet approach. The results were evaluated and discussed jointly with Dr. Sannan, Dr. Li and Christoph Meraner. The manuscript was written by the main author. All co-authors provided valuable input on the final version of the article.

Additional publications

In addition to the publications selected for this thesis, several other scientific contributiopns have been made thourghout the duration of the doctoral education. These are listed below.

Conference presentations

- F. Grøvdal, S. Sannan, T. Løvås, *LEM3D, SOLVING 3D as 3×1D*. The 37th International Symposium on Combustion. Dublin July 29 - August 3, 2018. (Visual presentation).

- F. Grøvdal, S. Sannan, A.R. Kerstein, J.-Y. Chen, T. Løvås, *A Hybrid RANS-LEM3D Model Applied to a Turbulent Lifted Hydrogen Flame in Vitiated Co-Flow*. Nordic Flame Days 2017. Stockholm October 10-11, 2017. (Conference proceeding / oral presentation).

- F. Grøvdal, S. Sannan, A.R. Kerstein, J.-Y. Chen, T. Løvås, *Three-dimensional Linear Eddy Modelling of a Turbulent Hydrogen Jet Flame in a Vitiated Co-flow*. Tenth Mediterranean Combustion Symposium. Naples September 17-21, 2017. (Conference proceeding / oral presentation).

- F. Grøvdal, S. Sannan, A.R. Kerstein, J.-Y. Chen, T. Løvås, *Three-dimensional Linear Eddy Modelling of a Turbulent Hydrogen Jet Flame in a Vitiated Co-flow*. SIAM- Sixteenth International Conference on Numerical Combustion. Orland April 3-5, 2017. (Oral presentation).

- F. Grøvdal, S. Sannan, A.R. Kerstein, J.-Y. Chen, T. Løvås, *HYDROGEN*

USE IN CO$_2$ CAPTURE TECHNOLOGIES. CLIMIT SUMMIT 2017. Oslo March 7-8, 2017. (Visual presentation).

- F. Grøvdal, S. Sannan, A.R. Kerstein, T. Løvås, *THREE-DIMENSIONAL LINEAR EDDY MODELLING OF COMBUSTION OF TURBULENT HYDROGEN FLAMES*. The 36th International Symposium on Combustion. Seoul July 31 - August 5, 2016. (Visual presentation).

Contents

Organization of the thesis

Chapter 1 gives introduction to the thesis work. The thesis framework is first set by motivating the work through a crude overview over turbulent combustion and turbulent mixing difficulties.

A description of the nature of turbulent eddies and the mathematical derivation behind the triplet map and its probability density functions are given in Chapter 2.

Chapter 3 states and describes the need for modeling within simulations of turbulent flows. Further the assumptions used within the LEM3D model framework are stated and discussed.

LEM3D is described in detail in Chapter 4. The Chapter includes illustrations of the operations in the model and presents the available options within the model framework.

Chapter 5 presents and discusses the main results found in the publications included in this work.

A conclusion of this work and incentives for future research activities are given in Chapter 6.

The three selected publications are reprinted and included in the thesis.

Abbreviations and Symbols

Functions

$[\ ]$	Units operator
$\lceil \cdot \rceil$	$= \min \{ \mathrm{n} \in \mathbb{Z} \mid \mathrm{n} \geq \cdot \}$ Ceiling of $\cdot$
$\langle \cdot \rangle$	Mean value
$\lfloor \cdot \rfloor$	$= \max \{ \mathrm{n} \in \mathbb{Z} \mid \mathrm{n} \leq \cdot \}$ Floor of $\cdot$
$\mathcal{O}(\cdot)$	Computational time
$\lvert \cdot \rvert$	Absolute value
$c(x,t)$	Concentration field at location x and time t
$d(x,y)$	Manhattan metric
$E(\kappa)$	Scalar energy distribution function per mass unit for a certain wave number value κ $\qquad$ [m^3/s^2]
F_l	CDF of the eddy sizes
f_l	PDF of the eddy sizes
F_s	CDF of the eddy location
f_s	PDF of the eddy location
F_t	CDF of the eddy time
f_t	PDF of the eddy time
$O(\cdot)$	Order of accuracy using big O notation

Greek Symbols

χ	Scalar dissipation rate	[1/s]
χ_b	Fraction of burning fine structures in EDC	[-]
Δt	Advective time step	[s]
Δt_D	Diffusion time step given by the linear stability condition	[s]
Δt_M	Molecular time step	[s]

Δt_{LEM}	Time instance of the next triplet map, locally defined within each 3DCV	[s]
Δx	3DCV cell size	[m]
Δx_w	LEM cell size	[m]
Δ	Discrete correction vector $\in \mathbb{Z}^6$	[-]
δ	Number of wafer displacements	[-]
Δ_l	Discrete corrections $\in \mathbb{Z}$	[-]
η	$= (\nu_M/\varepsilon)^{1/4}$ Kolmogorov micro length scale	[m]
η_B	Batchelor micro length scale	[m]
γ	$= c_p/c_V$ ratio of the specific heats	[-]
γ^*	Volume fraction occupied by fine structures in EDC	[-]
γ_λ	Fraction of the flow occupied by the fine structure regions in EDC	[-]
γ_l	Prescribed displacement	[-]
κ	Wave number	[1/L]
Λ	$= (\lambda \Delta x)^{-1}$ Mean value of f_t	[1/s]
λ	Eddy frequency per unit length	[1/(m·s)]
ν_M	Molecular kinematic viscosity	[m^2/s]
ν_T	Turbulent kinematic viscosity	[m^2/s]
ω_ϕ	Reaction rate (production rate)	[(kg)$_\phi$/kg/s]
ϕ	Reactive scalar	[kg]
ρ	Density	[kg/m^3]
$\Re$	The root(s) in breadth-first search	[-]
σ_T	$= \nu_T/D_T$ Turbulent Schmidt number	[-]
σ_h	Turbulent Prandtl number of the energy equation	[-]
σ_{Y_i}	Turbulent Schmidt numbers of the mass balance equations	[-]

τ	Residence time	[s]
ε	Dissipation term in the equation for turbulence energy	[m^2/s^3]
φ	Scalar	[*varying units*]
ξ	Mixture fraction	[-]
Ξ_l	The associated deviation for a 3DCV face	[kg/s]
Ξ_{flux}	$= \sum_{l=1}^{N_{\text{faces}}} \Xi_l$ The assosiated deviation for a 3DCV	[kg/s]

Superscripts

$-$	Mean value
$\cdot$	Flux
$\sim$	Mass-weighted average value
$'$	Fluctuating value

Latin Symbols

$\mathcal{U}$	Velocity constraint in Eulerian dilatation approach	[1/s]
$\mathbb{D}_{kj}$	Binary diffusion coefficients	[m^2/s]
A	Surface	[m^2]
C	Constant $\in \mathbb{R}$	[-]
c	Progression variable	[-]
C_μ	Constant in the k-ε model	[-]
C_K	Constant for the energy spectrum $E(\kappa)$	[-]
C_{rot}	Rotation frequency constant	[-]
d^2	Squared deviations	[*varying units*]
D_T^{rot}	Diffusivity induced by the auxiliary coupling	[m^2/s]
D_T^{TM}	Triplet map (effective) diffusivity	[m^2/s]
D_M	Molecular diffusivity	[m^2/s]
D_T	Turbulent diffusivity	[m^2/s]

$D_{\max}$	$= \max\left(D_{Y_i,l}\right)$ Largest value of the diffusion coefficients	[m^2/s]
D_{kj}	Multicomponent diffusion coefficients	[m^2/s]
D_k^T	Diffusion coefficient for thermal diffusion for species k	[m^2/s]
$D_{Y_i,l}$	Diffusion coefficient of species i at the lth cell location of a given LEM domain.	[m^2/s]
E	Activation energy	[J/mol]
f	Fraction of program which require serial operations	[-]
h_k	Enthalpy	[J]
k	Turbulent kinetic energy	[m^2/s^2]
$k_{\max}$	Largest numerical size of the triplet map	[-]
$k_{\min}$	Smallest numerical size of the triplet map	[-]
L	Integral length scale	[m]
l	Eddy size, $\eta \leq l \leq L$	[m]
N	$= \lambda l$ Number of random walk displacements per unit time	[1/s]
N_i	$= X/\Delta x$ Number of 3DCVs in an i-oriented LEM-domain	[-]
N_j	$= Y/\Delta x$ Number of 3DCVs in a j-oriented LEM-domain	[-]
N_k	$= Z/\Delta x$ Number of 3DCVs in a k-oriented LEM-domain	[-]
N_{LEM_d}	$= N_d \cdot \mathrm{LEM}_{\mathrm{res}}$ Number of wafers in a LEM-domain of direction d, $d \in [i,j,k]$	[-]
p	Scaling exponent in the linear eddy model	[-]
p_s	Number of processors	[-]
p_{rot}	Rotation probability	[-]
R	Specific gas constant	[J/(kg· K)]
r	Random number $\in [0,1]$	[-]
r_l	$= \Xi_l/\overline{\rho}$ Constant density deviation	[m^3/s]

R_u	Universal gas constant	[J/(mol·K)]
S	Computational speedup factor	[-]
t	Time	[s]
T_b	Adiabatic flame temperature	[K]
T_l	$= L/u'$ Turbulent timescale	[s]
u	Fluid velocity	[m/s]
V	Volume	[m^3]
V_w^g	Geometric wafer volume	[m^3]
V_w^t	Thermodynamic wafer volume	[m^3]
W	Molecular weight	[g/mol]
X	Size of the LEM3D domain in the x-direction	[m]
x_0	Position at which the concentration field is affected by a triplet map, where $x_0 + l/2$ is the center of the map	[-]
X_k	Mole fraction of species k	[(mol)$_k$/mol]
Y	Size of the LEM3D domain in the y-direction	[m]
Y_k	Mass fraction of species k	[(kg)$_k$/kg]
Z	Elemental mass fractions	[-]
Z	Size of the LEM3D domain in the z-direction	[m]
z	Displacement distance	[-]
fac	$= \Delta x_w/\eta$ Under-resolving factor	[-]
L	Length unit	[m]
p	Static pressure	[Pa=N/m^2]
p$^+$	Dilatation expansion criteria	[Pa=N/m^2]
Re	$= uL/\nu_m$ Reynolds number	[-]
T	Time unit	[s]

Abbreviations

TM	Triplet Map
3DCV	Control volume in LEM3D
BF	Breadth-first search
CCS	Carbon Capture and Storage
CDF	Cumulative distribution function
CFD	Computational fluid dynamics
CFL	Advective Courant-Friedrichs-Lewy number [-]
CFL_D	Diffusive CFL number [-]
CFL_{3DCV}	Loval Courant-Friedrichs-Lewy number of a 3DCV [-]
CV	Control volume
DNS	Direct numerical simulation
EBU	Eddy Break Up Model
EDC	Eddy Dissipation Concept
EDM	Eddy Dissipation Model
HYCAP	Hydrogen Use in CO_2 Capture Technologies
LBMS	Lattice-Based Multiscale Simulation
LEM	The standalone LInear Eddy Model
LEM_{res}	# of LEM wafers in each direction in 3DCV
LEM3D	The three dimensional linear eddy model formulation
LES	Large Eddy simulation
ODT	One Dimensional Turbulence Model
PDE	Partial Differential Equation
PDF	Probability density function
PIV	Particle Image Velocimetry

PSR   Perfectly Stirred Reactor

RANS   Reynold's averaged Navier Stokes equation

RILEM   Representative interactive linear-eddy-model

SBES   Stress-blended eddy simulation

TDMA   Tridiagonal Matrix Algorithm

Model - A thing used as an example to follow or imitate. [1]

A model is meant to illuminate certain characteristics of a phenomenon, without claiming to fully describe the phenomenon. It is important to realize that for every model there are assumptions, and to understand the prerequisites for these and how they restrict the range of acceptability. The acceptability of a model will vary with the physical conditions, what it is used for, and who is using it. Consequently, a model will not be "right" or "wrong"; it will only be a good or not as good approximation to the real world.

1. Introduction

The worldwide increase in demand of energy combined with the need to mitigate climate change necessitates technology (and lifestyle) changes; a nagging and contradicting problem of our generation. An aspect of the needed change is a decrease in the amount of anthropogenic carbon emissions into the atmosphere. A combination of solutions are needed, as the needed decrease cannot be expected to be achieved through a single technology or source of change. One possible technology is Carbon Capture and Storage (CCS) [20]. It is an important part of the of the total green-house mitigation efforts needed for 2010-50, as described in IEA's BLUE Map scenario [11, 29]. The realization of the next-generation CCS technologies depends on the development of viable and cost-competitive solutions both for carbon dioxide (CO_2) capture, transport and geological storage (see e.g., The Zero Emissions Platform [75]). CCS is likely to play some role due to its combination of mature and promising emerging technologies, such as the burning of hydrogen (H_2) in gas turbines created by pre-combustion CCS separation processes [31] with potential of negative emissions [68] through, e.g., bioenergy with Carbon Capture and Storage [28]. By the pre-combustion capture concept, the carbon is removed from the fossil fuel (which may be natural gas or coal) prior to the combustion, and the remaining hydrogen-rich gas is utilized for power production. Clean, efficient and safe burning of hydrogen and H_2-rich fuels is a key part to several pre-combustion CO_2 capture strategies.

The challenges of hydrogen combustion are linked to the specific thermo-physical properties of hydrogen, compared to natural gas, leading to a dramatically different combustion behavior, e.g. at stoichiometric ratios the hydrogen flame speed is nearly an order of magnitude higher (faster) than that of gasoline. Thus, the primary technology for low-nitrogen oxides (NO_x) power generation in stationary gas turbines, lean premixed combustion, has not yet been developed for hydrogen combustion. Issues related to auto-ignition, flame stabilization, flashback, and NOx control need to be resolved to achieve a clean, efficient, and safe burning of H_2-rich gases. The goal of the industry is to develop new gas turbine combus-

tors that can operate with low-carbon fuels, an achievement that will represent a considerable leap forward in environmental-friendly power generation from fossil fuels. Although the combustion of hydrogen in air theoretically emits only water, the high reactivity and elevated combustion temperature generate harmful and regulated nitrogen oxides, that to date, no commercial burner can mitigate sufficiently.

One of the main keys to the development of novel combustion technologies is numerical design tools with high predictive powers. For most industrial-scale combustions system under the prescribed operation conditions, the flow of interest will be turbulent with a large range of length and time scales [4, 18, 105]. *Turbulence itself is probably the most complex phenomenon in non-reacting fluid mechanics. Various time and length scales are involved and the structure and the description of turbulence remain open questions. The literature on this topic is enormous and probably proportional to the difficulty of the task* [76]. The needed fidelity for turbulent flows is available from Direct Numerical Simulation (DNS), i.e. numerical solution of the exact equation set. The cost of such detail is, unfortunately, unafordable for most practical applications. Therefore a reduced description in predictive modeling of mixing and reaction in turbulent flow environments is needed in order to accelerate the development of next-generation carbon capture and combustion technologies. The quest for such capability at the needed scale and level of detail confronts the fundamental scientific challenge of developing a reduced physical/mathematical representation of turbulence and its interactions with chemical reactions and related sub-processes.

A variety of combustion models exists, with variable capabilities of describing certain features in turbulent combustion, typically either premixed or non-premixed combustion [73]. As most industrial combustion systems are neither non-premixed, nor premixed, but rather a combination of those [14], i.e. partially premixed, regime-independent modeling is a widely recognized goal of turbulent combustion modeling. This goal is driven by the need to model configurations involving various combinations of regimes including the above in addition to extinction, re-ignition, recirculation, stratified premixed combustion, compression ignition, multi-stage ignition, and transition to detonation. Techniques involving coarse-graining, ensemble averaging, or stat-space modeling face difficulties due to the lack of detailed representation of regime specific advection–diffusive-reactive coupling [15].

Progress in addressing these difficulties can be anticipated, e.g., from the transported probability density function (PDF) framework [80] for turbulence chemistry interactions and the Stress-blended eddy simulation (SBES) for turbulence [65, 64, 66]. However, the challenge of regime-independent modeling suggests the concurrent pursuit of an alternative approach. Namely, the development of

a conceptually and computationally minimal model that resolves, in space and time, some plausible representation of the coupled advancement of advection, diffusion, and reaction in turbulent reacting flow. The potential advantages of this strategy motivated the formulation, three decades ago, of the linear-eddy model (LEM) [34]. Table 1.1 includes some of the commonly used turbulent combustion models. The rest of this chapter will focus on LEM-based models, through reviews of computational models for turbulent reacting flows can be found in, e.g., [17, 18, 73, 76, 104].

	Combustion Regime	
	Premixed	**Non-premixed**
Infinitely fast	Eddy Break Up Model (EBU) [95, 96]	Eddy Dissipation Model (EDM) [52]
	Bray-Moss-Libby Model [6]	Conserved Scalar Equilibrium Model (ξ) [73]
	Coherent Flame Model [53]	
Finite rate	Flamelet Model based on the G-equation (c) [91]	Flamelet Model Based on Mixture Fraction (ξ,χ) [72, 74]
		Conditional Moment Closure (ξ,χ) [3, 41]
	Eddy Dissipation Concept (EDC) [49, 50]	
	Linear Eddy Model [33]	
	One Dimensional Turbulence Model [37]	
	Flamelet generated manifold(c, ξ) [102]	
	PDF Transport [80]	

Table 1.1: Classification of turbulent combustion models in terms of chemistry and mixing, based on Table 1.1. in [73] but modified and extended from its original state.

LEM was originally formulated as a scalar mixing model for non-reacting flows [33], but was later adapted to a turbulent reactive framework [35]. Resolving all advective, diffusive and chemical time and length scales of turbulent combustion,

LEM does not rely on scale separation [73]. Nevertheless, mass species fractions and temperature transport between adjacent mesh cells have to be explicitly described from either experimental data or CFD. LEM formulations do however have some difficulties as viscous dissipation nor vortex stretching including flame front curvatures is accounted for. The latter one, inevitable in the one dimensional framework, play an important role in flame-turbulence interactions [77, 83]. Neglecting these effects, LEM has successfully simulated turbulent mixing [57], turbulent premixed combustion [60, 92] and turbulent non-premixed combustion [54, 63]. The representation of thermal expansion is implemented by means of dilatation of the 1D domain, but LEM does not model other aspects of feedback from combustion to turbulent motions, e.g, turbulence generation by expansion and viscosity variations.

In the lack of feedback from combustion to turbulent motions, the One Dimensional Turbulence model (ODT) was created, intended to have the capabilities of local, time-resolved interactions between turbulent eddy motions and combustion processes [36]. ODT, as LEM, is a one dimensional model whose standalone capabilities is restricted to the limitations of a robust 1D stochastic framework.

To mitigate the need of details outside of a one-dimensional domain, various extensions from one to three-dimensional formulations have been suggested and implemented both for ODT and LEM. Discussions on the ODT-based 3D flow simulation formulations can be found in, e.g., [37, 38, 55]. LEM was first implemented as a sub-grid model to Large Eddy Simulations (LES) in a temporally evolving two-dimensional mixing layer [59]. This framework was later extended to three dimensions and given the name LEM-LES [7, 61, 85]. The approach has successfully simulated turbulent scalar mixing [56], turbulent premixed combustion [62] and turbulent non-premixed combustion. Although LES-LEM treat molecular diffusion directly along "some" direction within the flow field, most turbulent flames have a strong multi-dimensional nature such that the ad hoc description of sub-grid scale turbulent convection via the triplet mapping procedure correspond to physical limitations of the model. This cannot necessarily be justified [67].

As an alternative to the non-oriented LEM domains of LEM-LES, a 3D formulation where the LEM domains have physical orientation was suggested and implemented [108, 109]. The model structure, based on some of the same concepts as the ODTLES model [89, 90], accounts for advection by Lagrangian coupling of domains and treats molecular diffusion, turbulent advection and reactions through the LEM framework. The non-reacting framework for LEM3D was assessed through a number of relative simple test cases in a previous study [108]. The model successfully simulated passive scalar mixing from a point source placed in grid turbulence and self-similar region of a turbulent jet in [88, 108]. The starting point of this

thesis is where the past work ended, at non-reacting flows implemented through volume-fluxes in a sequential code. The present work includes the extension to reacting flow, parallelization and mass-fluxes, in addition to investigations of the effects of random rotations, iteration schemes, flow fields and parameters.

The objective of the Hydrogen Use in CO_2 Capture Technologies (HYCAP) project, has been to focus on efficient and reliable energy conversion of hydrogen targeted to cost-reduction of the pre-combustion CO_2 capture concept. While the primary contribution from the study, as a part of the HYCAP project, has been to continue the development of LEM3D as a high-fidelity numerical design tool for hydrogen-fired gas turbines and combustion applications in general. With the objective of applying the novel numerical simulation tool to challenging flow configurations with high relevance to the development of H2-fired gas turbines.

Figure 1.1 is presented in order to illustrate the, theoretical difference in computational cost between LEM3D and DNS. DNS is even computationally too expensive, when solving canonical flows like homogeneous isotropic turbulence. For instance, in the case of homogeneous turbulence the number of grid points required in each direction must be of the order $Re_L^{3/4} \sim (L/\eta)$, following from Kolmogorov theory [43]. Thereby, the computational cost scales as $Re_L^{9/4} \sim (L/\eta)^3$ [80]. Unfortunately, most combustion processes of practical interest involve high Reynolds numbers ($Re > 10^6$) in addition to complex geometries. With Reynolds numbers of $Re = 10^4$ and $Re = 10^5$, keeping the integral scale at $L = X$, the plot in Figure 1.1 follows from table 4.1.

Computationally the description of chemically reaction systems often leads to reaction mechanisms with far above hundred chemical species (and, therefore, to more than a hundred partial differential equations), which possibly react within more than a thousand of elementary reactions. These kinetic processes cover time scales from nanoseconds to seconds, often being the typical bottleneck in CFD simulations. Assuming for simplicity that the that the computational cost equals the number of cells times a factor C, the cost for a fully resolved DNS is

$$\mathcal{O}(\text{DNS}) = \text{C} \left(\frac{\text{X}}{\eta} \right)^3 \sim \text{C} \, \text{Re}_{\text{L}}^{9/4}. \qquad (1.1)$$

In comparison, the computational cost for LEM3D is

$$\mathcal{O}(\text{LEM3D}) = \text{C} \frac{\Delta \text{x}}{\eta} \left(\frac{\text{X}}{\Delta \text{x}} \right)^3 \sim \text{C} \left(\frac{\text{X}}{\Delta \text{x}} \right)^2 \text{Re}_{\text{L}}^{3/4}. \qquad (1.2)$$

Even though the above estimates of computational cost make use of a crude approximation, it gives a good comparison in order of magnitude of the computa-
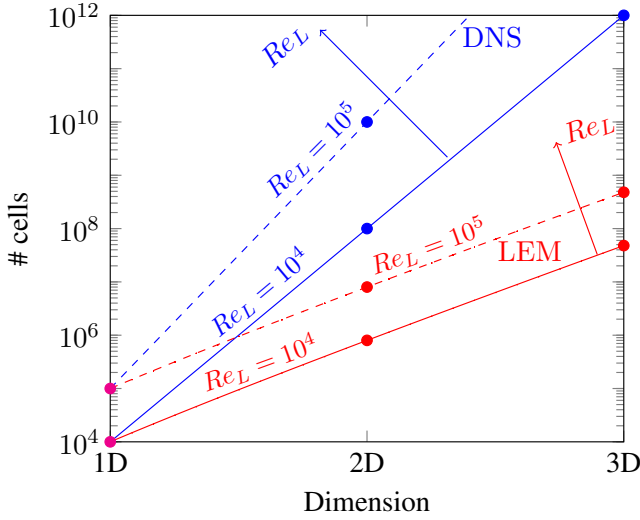
Figure 1.1: Number of computational cells versus spatial dimensions in turbulent flows for traditional fully resolved CFD, DNS, and the LEM3D approach, both plotted for two sets of Reynolds numbers. The dotted lines indicate the trends in number of cells by an increase in Re. It should be noted that the lines are shown for visualization and that the number of spatial dimensions is an integer.

tional cost relation between DNS and LEM3D

$$\frac{\mathcal{O}(\text{DNS})}{\mathcal{O}(\text{LEM3D})} = \frac{C\left(\frac{X}{\eta}\right)^3}{C\frac{\Delta x}{\eta}\left(\frac{X}{\Delta x}\right)^3} = \left(\frac{\Delta x}{\eta}\right)^2. \tag{1.3}$$

The fraction $\Delta x/\eta$ will later be defined as LEM_{res} which often is in the order 10^2, hence $\mathcal{O}(\text{DNS})/\mathcal{O}(\text{LEM3D}) \sim 10^4$. In other words, when a DNS simulation requires 3 years to run, LEM3D will only spend a single day. This can have enormous implications for the practical ability to study turbulent combustion in real applications.

2. Turbulent eddies

2.1 Turbulence

Before being able to discuss turbulent eddies, turbulence needs to be discussed. Anyone who has watched the smoke rising from a campfire has some conception of the nature of turbulence. Despite that turbulence is exceptionally difficult to grasp; being the most complicated kind of fluid motion and peculiarly resistant to mathematical treatment: *indeed, turbulence studies may be defined as the art of understanding the Navier-Stokes equations without actually solving them* [5]. No unified definition of turbulence exists. However, several definitions are accepted and frequently used. One among these is:

Bradshaw, 1971 [5]:   Turbulence is a three-dimensional time-dependent motion in which vortex stretching causes velocity fluctuations to spread to all wavelengths between a minimum determined by viscous forces and a maximum determined by the boundary conditions of the flow. It is the usual state of fluid motion except at low Reynolds numbers.

What is clear from the above definition is that in order to understand turbulence itself, the structures within the turbulence needs to be understood. Namely, the vortices, or turbulent eddies, and their behavior need to be described. A characteristic feature of turbulent flows is the occurrence of eddies of different length scales, often illustrated through the energy spectra; ranging from the smallest scales, the Kolmogorov η or Batchelor scale η_B, to the largest, the integral scale L, see, e.g., [17, 26]. A full review of turbulent eddies will not be given here, but can be found in, e.g., [26, 80].

Figure 2.1 illustrates the conceptual representation of turbulent eddies in one, two and three dimensions and their respective effect on iso-surfaces in one, two and three dimensional space. The bottom pictures motivate the use of a mapping in-
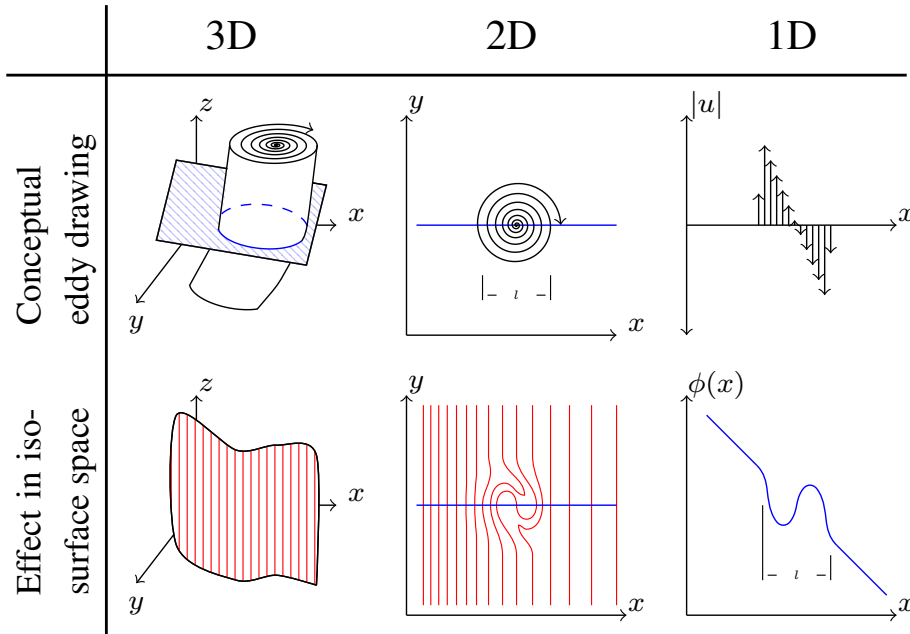
Figure 2.1: Conceptual illustration of eddies and their effect in iso-surface space for one, two and three dimensions. The top row illustrates an eddy in the given dimension, with the the red object being the outer shape of the cut by a plane or line, for two and three dimensions, respectively. The bottom row conceptually illustrate the effect of a single eddy in iso-surface space.

creasing the gradients in the flow based on its location and size. Specifically, the bottom right picture gives rise to the stochastic eddy event used in LEM, namely the triplet map.

2.2   Mathematical background for the Triplet Map

The rest of this chapter presents the mathematical formulation of and the representation of the triplet map itself. The triplet map is used in the one-dimensional Linear Eddy Model given by Kerstein [34, 35], and later in ODT [36, 40], OD-TLES [21, 90], Lattice-Based Multiscale Simulation(LBMS) [98], Representative interactive linear-eddy-model(RILEM) [45, 46] and LEM3D [88, 108] to name a few. The description given aims to increase the reproducibility and is structured in a different mathematical manner than the previous presentations as in e.g., [15, 58]. It can be skipped by readers only interested in the conceptual ideas of the model, which is described in Chapter 4.

The following description is written in a bottom-up manner. Firstly, Richardson's

hypothesis relating turbulent eddy sizes to their introduced turbulent viscosity is given in sub-subsection 2.2.1. Secondly, sub-subsection 2.2.2 states the definition of the triplet map together with the mean square displacement of a single triplet map. Then, sub-subsection 2.2.3 combine Richardson's hypothesis and the mean square displacement of triplet maps to give an expression for the eddy frequency and size distribution for triplet maps in the Linear Eddy Model. Lastly, a conventional implementation of the triplet maps are given in sub-subsection 2.2.4.

2.2.1 Richardson's hypothesis

Richardson [81, 82] was the first to introduce the concept of a continuous range of eddy sizes, where turbulent kinetic energy is being handed down from larger to smaller eddies and ultimately dissipated by the viscous action. In his study of the relative diffusion of particles from 1926, Richardson empirically found, using relatively crude data, the following relation relating the turbulent viscosity induced by a turbulent eddy to the mean length between two particles l (i.e. the characteristic size of a turbulent eddy):

$$\nu_T \propto 0.6\, l^{4/3}. \tag{2.1}$$

Taylor [99] later showed that the turbulent dissipation rate ε is a key parameter when considering turbulent flows. He claimed that ν_T depends only on the size l of an eddy and the dissipation rate ε. Dimensional analysis gives

$$\nu_T \approx \varepsilon^m \cdot l^p, \tag{2.2}$$

$$\left[\frac{L^2}{T}\right] = \left[\frac{L^2}{T^3}\right]^m \cdot [L]^p, \tag{2.3}$$

where [ ] is the units operator with L and T being is the length and time unit. This implies $m = 1/3$ and $p = 4/3$. Hence,

$$\nu_T \approx \epsilon^{1/3} \cdot l^{4/3}. \tag{2.4}$$

The more commonly used hypothesis of Kolmogorov [43] from 1941, in which the energy spectrum of turbulence was introduced, is quite similar to the Richardson/Taylor hypothesis. The main difference is that Kolmogorov expresses ν_T by the wave number $\kappa = \frac{2\pi}{l}$ instead of the eddy size l, i.e. the energy spectrum is

$$E(\kappa) = C_K\, \varepsilon^{2/3} \kappa^{-5/3}, \tag{2.5}$$

and

$$\nu_T(\kappa) \propto \varepsilon^{1/3} \cdot \kappa^{-4/3}. \tag{2.6}$$

It should be noted that an alternative argument for the scaling law $p = 4/3$ of the turbulent diffusivity can be given, as in e.g., [58]. This is done by additional scalings for the diffusivity, $D_T(l) \sim l^2/T_l$, where the time scale T_l for the turbulence is $T_l \sim l/u'$. This gives $D_T \sim u'l = \nu Re_l$. Using the fact that Re_l scales as $(l/\eta)^{4/3}$, we obtain $D_T \propto l^{4/3}$.

2.2.2 The Triplet map

Definition 1. Let l denote the size of the eddy mapping and $x_0 + l/2$ be the center. Further, let $c(x, t_n)$ and $c(x, t_{n+1})$ denote the concentration field before and after the map, respectively. The triplet map is defined as TM, where $c(x, t_{n+1}) = \text{TM}(c(x, t_n))$ and

$$
c(x, t_{n+1}) = \begin{cases} c(3x - 2x_0, t_n) & \text{if } x_0 \le x \le x_0 + l/3 \\ c(2l - 3x + 4x_0, t_n) & \text{if } x_0 + l/3 \le x \le x_0 + 2l/3 \\ c(3x - 2l - 2x_0, t_n) & \text{if } x_0 + 2l/3 \le x \le x_0 + l \\ c(x - x_0, t_n) & \text{otherwise.} \end{cases}
$$

As the triplet map is frequently assumed to instantaneous, it should be noted that the time index n and $n + 1$ in the current sub-subsection only is intended to denote the time instance before and after the triplet map, respectively. Further, notice that the map only affects the interval $x \in [x_0, x_0+l]$. Also, the map is surjective but not injective. Hence, for implementation purposes we will get some artificial diffusion for small l. The size l of a triplet map is frequently approximated by a multiple of three cells, denoted wafers, of size Δx_w through $l \approx k\Delta x_w$, where $k \in 3\mathbb{N}$. The map would typically be implemented by

$$
c(x, t_{n+1}) = \begin{cases} c(\frac{x-x_0}{3} + x_0, t_n) & \text{if } x - x_0 \equiv 0 \pmod 3 \\ c(\frac{2}{3}(l+1) - \frac{x-x_0-1}{3} + x_0, t_n) & \text{if } x - x_0 \equiv 1 \pmod 3 \\ c(\frac{x-x_0-2}{3} - \frac{2}{3}(l+1) + x_0, t_n) & \text{if } x - x_0 \equiv 2 \pmod 3 \end{cases}
$$

We now want to associate the diffusion induced by the random walk, as implied by the triplet maps, to turbulent transport. To do so, we examine the displacement for a given fluid element.

Definition 2. Let $z \in [-\frac{l}{2}, \frac{l}{2}]$ denote the distance from the center of a size l triplet map, i.e. $z = x - (x_0 + \frac{l}{2})$ and let $\delta(z|l)$ denote the displacement of the fluid element located at z after the map.

Lemma 1. The square displacement of an element from a triplet map of size l is

given by

$$\delta^2(z|l) = \begin{cases} 16z^2 & \text{if } 0 \leq |z| \leq \frac{l}{6} \\ (l - 2|z|)^2 & \text{if } \frac{l}{6} \leq |z| \leq \frac{l}{2} \\ 0 & \text{otherwise.} \end{cases} \tag{2.7}$$

Proof. Let us for simplicity, without loss of generality, assume that $x_0 = 0$. Since $z \in [-\frac{l}{2}, \frac{l}{2}]$, while $x \in [0, l]$ we have to add $l/2$ to calculate the displacement, i.e.

$$\delta(z|l) = (z + \frac{l}{2}) - x.$$

To prove the above, we consider the three different segments independently.

First, we look at the elements located at $z \in [-\frac{l}{2}, -\frac{l}{6}]$. During the map the elements moved to this segment was first compressed by a factor 3 and then shifted from $[-l/6, l/6]$ to $[-l/2, -l/6]$ by subtracting $l/3$. Mathematically, $z = (x - l/2)/3 - l/3$ or $x = 3l/2 + 3z$, which gives

$$\delta(z|l) = (z + \frac{l}{2}) - x = -l - 2z.$$

Since $z < 0$, $z = -|z|$ and we have

$$\delta(z|l) = -(l - 2|z|).$$

Second, we look at the elements located at $z \in [-\frac{l}{6}, \frac{l}{6}]$. During the map the elements moved to this segment was first compressed by a factor 3 and then flipped/mirrored by multiplying the segment $[-\frac{l}{6}, \frac{l}{6}]$ with a factor of -1. Mathematically, $z = -(x - l/2)/3$ or $x = l/2 - 3z$, which gives

$$\delta(z|l) = (z + \frac{l}{2}) - x = 4z.$$

Third, we look at the elements located at $z \in [\frac{l}{6}, \frac{l}{2}]$. During the map the elements moved to this segment was first compressed by a factor 3 and then shifted from $[-l/6, l/6]$ to $[\frac{l}{6}, \frac{l}{2}]$ by adding $l/3$. Mathematically, $z = (x - l/2)/3 + l/3$ or $x = -l/2 + 3z$, which gives

$$\delta(z|l) = (z + \frac{l}{2}) - x = l - 2|z|,$$

where $z = |z|$ as $z > 0$.

Now, squaring $\delta(z|l)$ for each of the segments we get Eq. (2.7). $\square$

Lemma 2. The mean square displacement of a single triplet map of size l is given by

$$\langle \delta^2(l) \rangle = \frac{4}{27} l^2.$$

Proof. Using the definition of the mean square displacement of a map of size l, we obtain

$$
\begin{aligned}
\langle \delta^2(l) \rangle &= \frac{1}{l} \int_{-l/2}^{l/2} \delta^2(z|l) \, dz \\
&= \frac{2}{l} \left[\int_0^{l/6} 16z^2 \, dz + \int_{l/6}^{l/2} (l - 2z)^2 \, dz \right] \\
&= \frac{2}{l} \left[16 \frac{z^3}{3} \Big|_0^{l/6} + \frac{-(l-2z)^3}{6} \Big|_{l/6}^{l/2} \right] \\
&= \frac{4}{27} l^2.
\end{aligned}
$$

$\square$

It is shown by Hinze [26] that the diffusivity associated with a random walk is dependent on the mean square displacement and the frequency parameter. I.e. let N denote the number of random walk displacements per unit time and $\langle \delta^2(l) \rangle$ the mean square displacement of a single triplet map event of size l. Then the associated diffusivity is given by

$$D_T = \frac{N \langle \delta^2(l) \rangle}{2}. \tag{2.8}$$

We now estimate the total diffusion induced by a single triplet map.

Lemma 3. Let λ denote the eddy event rate per unit length. The diffusivity associated with triplet maps of size l is

$$D_T(l) = \frac{2}{27} \lambda l^3.$$

Proof. The frequency of a triplet map is given by $N = \lambda l$. Inserting into Eq. (2.8) and using $\langle \delta^2(l) \rangle = \frac{4}{27} l^2$ gives the desired equation. $\square$

Finally, we have arrived at giving a relation between the diffusivity induced by triplet maps of all length scales. Using the fact that there only exist eddies in the range $l \in [\eta, L]$, i.e. from the Kolmogorov to the integral scale, the theorem below follows.

Theorem 1. Let $f_l(l; \eta, L)$ denote the probability density function of the eddy sizes. Then the turbulent diffusivity is given by

$$D_T = \int_\eta^L \frac{2}{27} \lambda l^3 f_l(l; \eta, L) dl. \tag{2.9}$$

2.2.3 The eddy distribution function

We here find the distribution function of the different eddy sizes.

Theorem 2. The probability density function of the eddy sizes is given by

$$f_l(l; \eta, L) = \frac{5}{3} \frac{l^{-8/3}}{\eta^{-5/3} - L^{-5/3}}. \tag{2.10}$$

Proof. From Richardson's hypothesis, the turbulent diffusivity D_T scales with l^p. We observe that $\int_\eta^L \frac{2}{27} \lambda l^3 f_l(l; \eta, L) dl \sim l^p$, i.e. $f_l(l; \eta, L) \sim l^{p-4}$. Hence, setting $f_l(l; \eta, L) = c \, l^{p-4}$ we get

$$\int_\eta^L f_l(l; \eta, L) dl = 1$$

$$\frac{c}{p-3} l^{p-3} \Big|_\eta^L = 1$$

$$c = \frac{1}{L^{p-3}} \frac{3-p}{(L/\eta)^{3-p} - 1}$$

Inserting c into $f_l(l; \eta, L)$, we get the eddy size distribution

$$f_l(l; \eta, L) = \frac{3-p}{(L/\eta)^{3-p} - 1} \frac{l^{p-4}}{L^{p-3}},$$

Finally, inserting $p = 4/3$ from Richardson's hypothesis yields Eq. (2.10). $\square$

Theorem 3. The eddy frequency per unit length is expressed as

$$\lambda = \frac{54}{5} \frac{D_T}{L^3} \frac{(L/\eta)^{5/3} - 1}{1 - (\eta/L)^{4/3}} \tag{2.11}$$

Proof. Insert the expression (2.10), for a general p, into Eq. (2.9) and integrating we get

$$\lambda = \frac{27}{2} D_T \left(\int_\eta^L l^3 f_l(l; \eta, L) dl \right)^{-1}$$

$$= \frac{27}{2} \frac{D_T}{L^3} \frac{(L/\eta)^{3-p} - 1}{1 - (\eta/L)^p} \frac{p}{3-p}$$
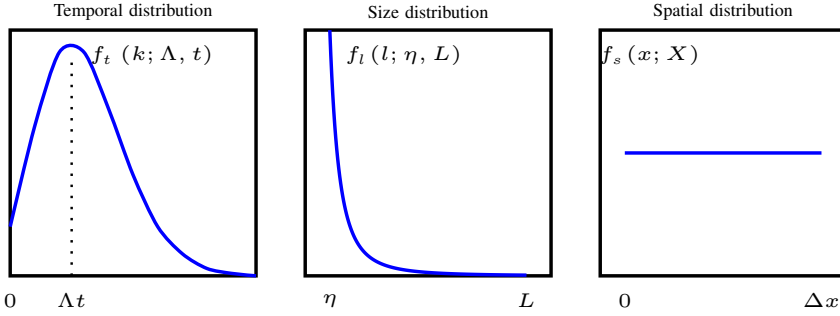
Figure 2.2: The three distributions used in the Linear Eddy Model. From left to right; the Poisson distribution used as temporal distribution, the eddy size distribution function, and the spatial distribution.

Now, inserting $p = 4/3$ this gives

$$\lambda = \frac{54}{5} \frac{D_T}{L^3} \frac{(L/\eta)^{5/3} - 1}{1 - (\eta/L)^{4/3}}. \tag{2.12}$$

$\square$

In the literature, an alternative expression of the eddy event frequency is often seen. Based on the turbulent Reynolds number and $Re_L = \frac{u'L}{\nu}$ the integral scale L is

$$\lambda = \frac{54}{5} \frac{\nu Re_L}{C_\lambda L^3} \frac{(L/\eta)^{5/3} - 1}{1 - (\eta/L)^{4/3}}, \tag{2.13}$$

where the model constant $C_\lambda = 15$ [93].

2.2.4 Implementation and usage of the distributions

In terms of implementation, the triplet map events are assumed to be instantaneous, statistically independent and following a Poisson process. Hence, the time t of the eddy events relates to the eddy event rate λ and the domain size Δx through a Poisson distribution with expectation/mean $\Lambda t = (\lambda \Delta x)^{-1} t$:

$$f_t(k; \Lambda, t) = \frac{(\Lambda t)^k}{k!} e^{-\Lambda t} \tag{2.14}$$

$$F_t(t; \Lambda) = e^{-\Lambda t} \sum_{i=1}^{\lfloor k \rfloor} \frac{(\Lambda t)^{-i}}{i!}, \tag{2.15}$$

where f_t gives the probability of k events in the time interval $[0, t]$, $\lfloor k \rfloor$ is the floor of k, i.e. it denotes the largest integer less than or equal to k and F denotes the cumulative distribution function (CDF), i.e. $F(t)$ is cumulative distribution function of the PDF f evaluated at t, it is the probability that $T \in [0, \infty\rangle$ will take a value less than or equal to t.

However, as f_t gives a discrete value of events in the time interval $[0, t]$, the arrival times in the Poisson process, i.e. the time between eddy events Δt_{LEM}, are calculated on-the-fly during the simulation. As the eddy events follow a Poisson process their arrival times follow an exponential distribution [84]. We hence sample Δt_{LEM} from

$$f_{\Delta t_{\text{LEM}}}(t; \Lambda) = \Lambda e^{-\Lambda \Delta t_{\text{LEM}}}, \tag{2.16}$$

$$F_{\Delta t_{\text{LEM}}}(t; \Lambda) = 1 - e^{-\Lambda \Delta t_{\text{LEM}}}. \tag{2.17}$$

A random number $r_t \in [0, 1]$ is drawn and the occurrence of the next triplet map is calculated from

$$\Delta t_{\text{LEM}} = F_{\Delta t_{\text{LEM}}}^{-1}(r_t; \Lambda) \tag{2.18}$$

Then size of the triplet map l is computed in a similar manner, i.e. $r_l \in [0, 1]$ is drawn and l is computed from the inverse of the cumulative distribution function of l, $F_l(l; \eta, L) = \int_\eta^L f_l(l; \eta, L) dl$:

$$l = F_l^{-1}(r_l; \eta, L). \tag{2.19}$$

The two distributions are given by:

$$f_l(l; \eta, L) = \frac{5}{3} \frac{l^{-8/3}}{\eta^{-5/3} - L^{-5/3}} \text{ and} \tag{2.20}$$

$$F_l(l; \eta, L) = \left(\frac{l}{L - \eta} \right)^{-5/3}. \tag{2.21}$$

Lastly, the eddy location is randomly sampled from a uniform distribution of eddies within coarse 1D (3D for LEM3D) control volumes in the domain prescribed from CFD or experiments. This spatial distribution is defined as

$$f_s(x; X) := \begin{cases} \frac{\Delta x_w}{\Delta x} & \text{if } x \in [X\Delta x, (X+1)\Delta x], \\ 0 & \text{else.} \end{cases} \tag{2.22}$$

That is, the eddy location is random within the coarse 1D (3D for LEM3D) control volume X and 0 elsewhere. Unless the domain boundary conditions are periodic, sampled eddies that extend outside the domain are not implemented. Figure 2.2 illustrates the three different probability density functions used in the LEM framework.

3. Modeling of Turbulence

3.1 Computational Fluid Dynamics

Computational fluid dynamics or CFD is the analysis of systems involving fluid flow, heat transfer and associated phenomena such as chemical reactions by means of computer-based simulations [103].

CFD enables scientists and engineers to perform "numerical experiments" in a "virtual flow laboratory". It is not intended to replace experimental measurements completely, but the volume of experiments and the overall cost can be significantly reduced. While experiments are able to provide quantitative descriptions, simulations provide predictions. Further, CFD gives insight into flow patterns that are difficult, expensive or even impossible to study using experimental techniques. This could be, for instance, consequences of a large scale fire on an oil platform or the effect of a detonation bomb. A flow field from CFD is so rich in information, even for a steady-state solution, that typically much of it is ignored in favor of near-field quantities such as surface temperatures, and force and moment coefficients. The accuracy of a CFD result is however, restricted by e.g., the mathematical model applied to the problem. Currently, the mathematics used in CFD are based on Partial Differential Equations (PDEs).

The general transport equation for a reactive scalar ϕ is given by the PDE as

$$\frac{\partial \rho \phi}{\partial t} + \frac{\partial \, \rho u_j \phi}{\partial x_j} = \frac{\partial}{\partial x_j} \left[\rho D_M \frac{\partial \phi}{\partial x_j} \right] + \rho \omega_\phi, \tag{3.1}$$

where ρ is the density, u_j is the velocity component in the coordinate direction x_j, D_M is the molecular diffusivity, and ω_ϕ is the chemical reaction rate. In the above equation, a gradient type model is assumed for the diffusive flux (Fick's law), and the molecular diffusivity D_M is assumed to be represented by a mixture-averaged quantity.

The governing equations of fluid dynamics are then discretized using any of a

variety of methods; finite volume, finite elements or finite difference methods, with several choices available for numerical flux approximations for all methods. *That such a variety of methods exists in CFD, with no clear winners and losers, after so many years of research is surprising indeed; this is not the case in other fields such as structural mechanics* [94]. As the accuracy of a CFD results is restricted by the available computational power, it is costume practice to settle on a given order of accuracy, a given resolution depending on the problem, and an appropriate physical model of turbulence which is used to describe the required turbulence detail. This indeed spans the spectrum of approaches, from Prandtl's mixing length model to Reynolds-Averaged Navier-Stokes (RANS) formulations which require turbulence to be modeled, and further to Direct Numerical Simulation (DNS) for which all the scales of turbulent motion are resolved and captured.

3.1.1 DNS

Stephen Pope [80] has given an excellent description of DNS: *Direct Numerical Simulations (DNS) consists in solving the Navier-Stokes equations, resolving all the scales of motion, with initial and boundary conditions appropriate to the flow considered. The DNS approach was infeasible until the 1970s when computers of sufficient power became available to simulate isotropic decaying turbulence. Even though it is a latecomer among modeling approaches, it is logical to discuss DNS first as it conceptually is solved similar to laminar flows, i.e. the Navier-Stokes equations are solved directly, by resolving all fluid motions by the mesh size. The cost is, however extremely high; and the computer requirements increase so rapidly with Reynolds number and domain size that the applicability of the approach is limited to flows of low or moderate Reynolds numbers of small spatial domains.*

When DNS can be applied, it is unrivaled in accuracy and in the level of description provided. However, due to the computational cost of DNS, additional modeling is often required when simulating turbulent reacting flows.

3.2 Modeling

Since about 99% of the computational workload goes to resolving the small-scale energy, with this making for only 20% of the total energy [80] it is evident that it would be preferable to model the small-scale energy instead of actually resolving these 20%. However, at the moment where the smallest scales of turbulence is no longer resolved, i.e. leaving the DNS framework, and entering the complex and enormous world of modeling, two immediate problems arises:

1. How do we model the turbulence not resolved?

2. How is the turbulence-chemistry interaction going to be treated?

There are several and wide spread answers to these two questions, and the reader is directed to other references for a thorough discussion [76, 80].

The most common approximation for turbulent flows is the Reynolds-averaged transport equation, below expressed in its most general form with Favre averaging, i.e.

$$\frac{\partial \bar{\rho} \widetilde{\phi}}{\partial t} + \frac{\partial \bar{\rho} \widetilde{u}_j \widetilde{\phi}}{\partial x_j} = \frac{\partial}{\partial x_j} \left[\bar{\rho} D_M \frac{\partial \widetilde{\phi}}{\partial x_j} - \bar{\rho} \widetilde{u_j'' \phi''} \right] + \bar{\rho} \widetilde{\omega}_\phi, \qquad (3.2)$$

where $\bar{\rho}$ denotes the mean of ρ, $\widetilde{\phi} = \overline{\rho\phi}/\bar{\rho}$ is the Favre-averaged scalar field, and $u_j'' = u_j - \widetilde{u}_j$ is the fluctuation of u_j about the Favre average $\widetilde{u}_j$. The term $\partial \left(\bar{\rho} \widetilde{u}_j \widetilde{\phi} \right)/\partial x_j$ gives the advective transport based on the velocity field $\widetilde{u}_j$.

Frequently used illustrations of the Reynolds average is a line of $\widetilde{\phi}$ with ϕ fluctuating around it. Under the Reynolds average approximation there are two unclosed terms in Equation (3.2), i.e. the Reynolds fluxes $-\bar{\rho} \widetilde{u_j'' \phi''}$ and the source term $\bar{\rho} \widetilde{\omega}_\phi$, corresponding to two issues addressed above namely turbulence closure and turbulence-chemistry interactions.

3.2.1 Turbulent advection

Since the turbulent flux term $-\bar{\rho} \widetilde{u_j'' \phi''}$ in equation (3.2) is unclosed, and the equations governing turbulent flow are very complicated, it is tempting and common practice to treat the diffusive nature of turbulence by means of a properly chosen effective diffusivity D_T. That is, through the gradient diffusion model with the gradient diffusion assumption, where $-\bar{\rho} \widetilde{u_j'' \phi''} = \bar{\rho} D_T \partial \widetilde{\phi}/\partial x_j$. For non-reacting flows the gradient diffusion assumption means that the averaged transport $\overline{\rho \mathbf{u}'' \phi''}$ of a scalar ϕ is oriented in a direction opposite to the normal gradient turbulent diffusion. By treating the diffusive nature of advective turbulence in a diffusive manner, the very idea of trying to understand the turbulence itself is partly discarded. *If we use an effective diffusivity, we tend to treat turbulence as a property of a fluid rather than as a property of a flow. Conceptually, this is a very dangerous approach. However, it often makes the mathematics a good deal easier* [100].

If we rely on the gradient diffusion assumption, however, we are able to express the Reynolds number as the ratio of turbulent and molecular viscosity [100]:

$$Re = \frac{uL}{\nu} \sim \frac{T_t}{T_m} \sim \frac{D_T}{D_M}. \qquad (3.3)$$
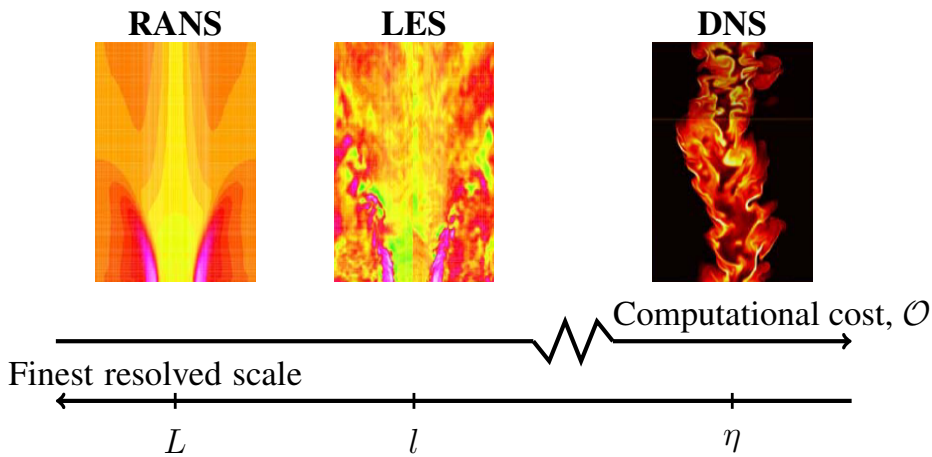
Figure 3.1: Different models have different resolutions, naturally affecting the computational time and details in the results. From left to right the computational cost increase and the resolution decreases. As DNS has substantially larger cost compared to RANS and LES the computational cost axis is truncated. Courtesy to SINTEF Energy for the plots used in the illustration.

Even though the complexity of the physical phenomena to be described is so complex that the gradient diffusion model is inevitable, it cannot be stressed too strongly that the eddy diffusivity D_T is an artifice which may or may not represent the effect of turbulence faithfully. This may be the case, for instance in inhomogeneous, anisotropic or streamline turbulence, since in such regions there could be counter-gradient diffusion which does not obey the gradient-diffusion assumption. Further, this sacrifice makes the two processes of molecular diffusion and advective turbulence indistinguishable. Unlike most of the other used models in reacting flows, and as described in Chapter 2, the Linear Eddy Model treats turbulence as turbulent advection through the one-dimensional rearrangement event. That is, rather than actually resolving all the turbulent eddies, the Linear Eddy Model aims to emulate their one-dimensional effect/impact on the scalar fields.

The k-ε model

The most frequently used model used to simulate mean flow characteristics for turbulent flow conditions models is the k-ε model. It is a two-equation model that gives a general description of turbulence by means of transport equations for the turbulent kinetic energy k and turbulent dissipation rate ε, respectively defined as $k = \overline{u'_i u'_i}/2$ and $\varepsilon = C_\mu k^{3/2}/L$, where $C_\mu = 0.09$ [47]. The original motivation

for the development of the k-ε model was to improve the mixing-length model, as well as to find an alternative to algebraically prescribing turbulent length scales in moderate to high complexity flows [30]. Within the k-ε framework the turbulence quantities needed for the LEM3D model, as described in Chapter 4, is given from the equation for k and ε through the below relations.

The turbulent diffusivity is given by the turbulent viscosity ν_t by

$$D_T = \frac{\nu_T}{\sigma_T} = \frac{C_\mu}{\sigma_T} \frac{k^2}{\varepsilon},$$ (3.4)

where σ_T is the turbulent Schmidt number (or the Prandtl number when referring to the temperature field).

Local values for the integral length scale L and the Kolmogorov scale η is prescribed to LEM3D. The integral and Kolmogorov scale are calculated from the k-ε model and given by

$$L = C_\mu \frac{k^{3/2}}{\varepsilon},$$ (3.5)

and

$$\eta = L \left(\frac{\nu_M}{\nu_T} \right)^{\frac{3}{4}}.$$ (3.6)

In order to obtain a more complete description of the physics, an alternative to the eddy/turbulent viscosity above is to derive a separate equation for each of the Reynolds stresses. Although such models, named Reynolds Stress Models (RSM), contain a more complete description of the physics, they are not widely used in turbulent combustion. Most industrial codes still rely on the k-ε model, which, by using an eddy viscosity, introduces the assumption of isotropy. It is known that turbulence becomes isotropic at the small scales, but this does not necessarily apply to the large scales at which the averaged quantities are defined. *The k-ε model is based on equations where the turbulent transport is diffusive and is therefore more easily handled by numerical methods than the Reynolds stress equations. This is probably the most important reason for its wide use in many industrial codes* [44].

3.2.2 Turbulence-chemistry interactions

Since the reactions occur at the small scales and resolution of all turbulent scales is prohibitively expensive, inertial range invariant quantities must relate properties defined at the small scales to those defined at the large scales, at which the turbulence models are formulated. That is, when only the largest scales of turbulence are modeled by, e.g., the k-ε model, we need a link between the *large*/integral length scale and the molecular scale. The chemical source term is particularly hard to

model as it is strongly nonlinear, includes a variety of timescales, and depends upon local concentrations and temperature (not on gradients):

$$\widetilde{\omega}_\phi(Y_i, \dots, Y_s, T).$$

There exists a wide range of approaches for solving the chemical closures and only three of the models will be discussed here. For a more detailed discussion on the subject, the reader is kindly pointed towards books on the topic, e.g., Fox [18], Ertesvåg [17] or Peters [73]. The three models are

– Moment methods, attempting to close the chemical source term by expressing the unclosed higher-order moments in terms of lower-order moments.

– PDF and PDF-like models, introducing micromixing models and solving the chemistry directly.

– Eddy cascade models

Moment methods

The moment methods for closing the chemical source term, also know as Arrhenius expansion models [17], are based on the Taylor expansion. With a better expansion follows higher momentum terms which is required to be closed. Typically, the source term is calculated through

$$\widetilde{\omega}_\phi(T) \approx \omega_\phi(\tilde{T}) \left(1 - \frac{T''}{T_b - \widetilde{T}} \right) e^{ET''/R_u \widetilde{T}^2}, \tag{3.7}$$

where T_b is the adiabatic flame temperature, E the activation energy (both from the Arrhenius expression), and R_u is the universal gas constant.

PDF and PDF like models

In PDF methods, exact transport equations for the scalars probability density functions are derived from the Navier Stokes equations. By constructing the transported PDF models assume the chemical reaction term is independent of closures and depend only on chemical variables. Unfortunately, the molecular diffusion term, often referred as the "micromixing term", is unclosed and difficult to model [80]. *This finding is not surprising: as the one-point PDF describes the chemical composition at any location, one-point quantities such as the chemical reaction rate, which depend only on the local composition, are naturally closed* [76].

Subramaniam and Pope [97] list a number of performance criteria for the micromixing models [108]:

(i) Decay of all variances towards and preservation of mean values.

(ii) Scalar values should not travel out of their bounds in composition space, i.e. boundedness.

(iii) A set of passive scalars should evolve independently and be linear with respect to the scalar field.

(iv) The scalar PDF should relax to Gaussian in homogeneous isotropic turbulence.

(v) Fluid elements that are separated in composition space should not mix, i.e. localness.

(vi) Differential diffusion effects should be taken into account.

(vii) Dependence on Reynolds number, shifting the energy spectrum towards higher wave numbers when Re increases.

(viii) The mixing should be dependent on turbulent length scales.

Several micromixing models have been developed, comprising both the deterministic and the stochastic models, to providing a closure of the micro-mixing term. It would be nearly impossible to go through all the micromixing models but two will be mentioned here. For each of the models, t_n denotes the time before mixing and t_{n+1} after mixing occurred.

First, the simplest mixing model is often considered to be the Interaction by Exchange with the Mean (IEM) [106], where all scalar values of individual particles are subject to relaxation toward the mean value. Letting $p \in [1, N_p]$, where N_p is the number of particles we have:

$$\phi_p(t_{n+1}) = \phi_p(t_n) + \Delta t \frac{\left(\widetilde{\phi}(t_n) - \phi_p(t_n) \right)}{\tau}, \tag{3.8}$$

where $\Delta t = t_{n+1} - t_n$ and τ is a constant often dependent on k and ε.

Second, the pairwise particle-interaction models named coalescence-dispersion (C-D) [12], where two and two particles, p_1 and p_2, are randomly selected and

mixed such that their new values are the mean of the two values before mixing:

$$\phi_{p_1}(t_{n+1}) = \phi_{p_2}(n+1) = \frac{1}{2}\left(\phi_{p_1}(t_n) + \phi_{p_2}(t_n)\right). \tag{3.9}$$

The relation of the micromixing model requirements with respect to LEM and LEM3D will be discussed in Section 3.3.

Eddy cascade models

The first attempt to provide a closure for the chemical source term through eddy cascades is due to Spalding [95], who argued that turbulent mixing may be viewed as a cascade process. Similar developments were independently conducted by Richardson [81], Kolmogorov [43], and Onsager [70, 71]. The existence of the energy cascade makes it possible to link the integral scale down to the molecular scales, a process which also controls the chemical reactions as long as mixing rather than chemistry is the rate-determining process [73]. This first model approach was called the Eddy-Break-Up Model. For this model, turbulent mean reaction rate of products is expressed as

$$\widetilde{\omega_p} = \rho C_{\text{EBU}} \frac{\epsilon}{k} \left(\overline{Y''^2_p}\right)^{1/2}, \tag{3.10}$$

where $\overline{Y''^2_p}$ is the variance of the product mass fraction and C_{EBU} is the Eddy-Break-Up constant.

The Eddy Dissipation Concept

Even though The Eddy Dissipation Concept (EDC) is included in the eddy cascade models presented above, it is devoted by its own subsubsection since this is the turbulence chemical-interaction used in the modeling of the vitiated co-flow burner in Article II and III. The description of EDC is here taken directly from [86].

EDC is a turbulence-chemistry interaction closure frequently used in turbulent combustion. It is an empirical method and conceptual model used for determining the mean reaction rate in the equations for the species mass fractions. EDC was developed by Magnussen and Hjertager [52], and later extended by Magnussen [49]. The basic idea of the model is the turbulent cascade concept for the transfer of energy from larger to smaller scales of a turbulent flow. The energy cascade model provides a connection between the smallest eddies of the flow, at the scale of the Kolmogorov dissipation scale, and the largest turbulent eddies at the scale of the integral length scale.

The characteristics of the larger scales is usually obtained from a standard turbulence model, such as the k-ε model or the Reynolds stress equation model. Hence,

chemical reactions, that are assumed to take place in small-scale regions where the dissipation of turbulence energy occurs, are described by large-scale quantities like the turbulence kinetic energy k, and the dissipation rate ε of k. In EDC, the regions where the dissipation of turbulence energy takes place are referred to as fine-structure regions. These regions consist of fine structures that typically are thin vortex sheets, ribbons, or elongated laments whose characteristic thickness is of the order of the Kolmogorov length scale. It is assumed that the molecular mixing and the chemical reactions are concentrated to the viscous fine structures of the turbulent flow. Thus, the fine structures provide the reaction space for the chemical reactions of the flow. The volume fraction of the turbulent flow occupied by the fine structures is expressed as

$$\gamma^* = \left(\frac{3C_{\mathrm{D2}}}{4C_{\mathrm{D1}}^2} \right)^{3/4} \left(\frac{\nu\varepsilon}{k^2} \right)^{3/4}, \tag{3.11}$$

where $C_{\mathrm{D1}} = 0.134$ and $C_{\mathrm{D2}} = 0.5$ are EDC model constants, and ν is the kinematic molecular viscosity [17]. In the turbulent flow, the fine structures tend to group in between the larger eddies, giving rise to the near structure regions. These regions have characteristic dimensions much larger than the fine structures themselves, and the fraction of the flow occupied by the fine structure regions is modeled as [50, 51]

$$\gamma_\lambda = (\gamma^*)^{1/3} = \left(\frac{3C_{\mathrm{D2}}}{4C_{\mathrm{D1}}^2} \right)^{1/4} \left(\frac{\nu\varepsilon}{k^2} \right)^{3/4}. \tag{3.12}$$

The volume fractions γ^* and γ_λ are types of intermittency factors and express the probabilities of finding fine structures or fine structure regions, respectively, at a given location. In the modeling context, the mass transfer rate between the fine structures and the surrounding fluid is also needed. Since the fine structures are supposed to exchange mass with the fine structure regions, the mass exchange rate between the fine structures and the surroundings, divided by the total mass of the fine structure regions, is modeled as γ_λ^2/τ^*, where τ^* is the fine structure residence time [22]. The residence time τ^* is the characteristic time scale of the fine structures, is given by

$$\tau^* = \sqrt{\frac{C_{\mathrm{D2}}}{3} \frac{\nu}{\varepsilon}}. \tag{3.13}$$

The fine structures are treated as a well stirred reactor in EDC. The mean reaction rate for a chemical species $k \in [1, S]$ is then expressed as

$$\widetilde{\omega}_k = \frac{\gamma_\lambda^2 \chi_b}{\tau^*} \left(Y_k^\circ - Y_k^* \right), \tag{3.14}$$

where χ_b represents the fraction of burning fine structures. The Y_k^* and Y_k° are the mass fractions of the fine structures and the surroundings, respectively, for

the species $k \in [1, S]$. In order to estimate the mean reaction rate (3.14), it is necessary to obtain the fine structure mass fractions Y_k^*. This is done by assuming either finite-rate chemistry or infinitely fast chemistry. The Favre-averaged mass fractions $\widetilde{Y}_k$ are then obtained from the relation

$$\widetilde{Y}_k = \gamma^* \chi_b Y_k^* + (1 - \gamma^* \chi_b)\, Y_k^\circ. \tag{3.15}$$

3.3   LEM3D and its assumptions

LEM3D, a three-dimensional scalar mixing model built upon stochastic processes, is spatially resolved in all three directions with full temporal resolution intended to have a significant reduction in computational cost in comparison to DNS. As LEM3D is a model, developed to achieve the above, we need some assumptions along the way:

- As the current method depends upon input from CFD which rely on the eddy viscosity hypothesis with the gradient diffusion assumption and using **Kolmogorov** theory in the expression of the turbulent parameters L, D_T and η, we assume that the error from these are neglectable as input parameters.

- Fluxes prescribed from CFD or experiments can sufficiently be described through **Lagrangian displacement of wafers**.

- The **dimensional-decomposition approach** with **auxiliary coupling** is acceptable.

- As the dimensional-decomposition approach introduces three representations of each control volume, one for each direction, the flow properties is multiplied by a **factor 3** to preserve the residence time.

- The effect of real three-dimensional turbulent eddies can satisfactorily be described through **one-dimensional instantaneous independent mappings**.

- The eddy size distribution can be approximated by $l^{-8/3}$ (Richardson's $p = 4/3$).

- The temporal distribution of eddy events follow a **Poisson process** with expectation/mean $\Lambda = (\lambda \Delta x)^{-1}$ where λ is given by Eq. (2.13).

- Turbulence **not resolved** through the mesh is assumed **isotropic**.

- Within the LEM wafers, chemistry is solved directly at **1** atm constant pressure, allowing for volume expansions. We assume **perfect mixing** within the wafers also when the wafers are **under-resolved** by $\Delta x_w = \text{fac} \cdot \eta$.

– Molecular diffusion can sufficiently be treated trough **Fick's law** with **mixture average or multicomponent diffusion** solved as a **1D process** between the wafers.

– **Re-gridding** of wafer sizes after dilatations do not introduce to much artificial diffusion.

– **Ideal gas law**

The above assumptions will be discussed in the remainder of this section. However, since some of these rely on concepts introduced in Chapter 4 it might be beneficial to read this in combination with Chapter 4.

3.3.1 LEM3D as a micromixing model

Even though LEM3D is not a micromixing model withing the PDF transport framework per se, it is PDF like in many aspects; LEM3D threats advection in a Lagrangian manner as virtually all numerical implementations of PDF methods for turbulent reactive flows does through the Monte-Carlo simulation techniques [78, 79]. As modeling of molecular mixing and chemical reactions is rendered unnecessary when LEM3D/LEM is employed, it can be considered as a micromixing-like model. Weydahl [108] considered LEM with respect to the requirements for micromixing models and concluded that it by construction meets all the requirements and that *concerning localness, LEM is local in the 1D physical space, which is physically more appealing than relating localness to composition space*.

However, in the LEM3D framework the auxiliary coupling creates sharp gradients, as discussed in Article III, violating the localness assumption as wafers mix/diffuse with wafers with a totally different composition, hence not in the immediate neighborhood in composition space as criteria (v) requires. The triplet map also enhances the gradients, but in a continuous manner. Other than criteria (v), LEM3D fulfills the same requirements as LEM.

3.3.2 Ideal Gas Law

The equation of state provides a relationship between the pressure p, the temperature T, and the volume V of a substance. The ideal-gas behavior is a gas where we can neglect intermolecular forces and the volume of the molecules in the modeling. We might hence write

$$\mathrm{p}V = n\mathrm{R}_u T = m\mathrm{R}T, \qquad (3.16)$$

where n is the amount of substance of gas given in mole, m is the mass and the specific gas constant R $[\mathrm{J}/(\mathrm{kg} \cdot \mathrm{K})]$ is related to the universal gas constant $\mathrm{R}_u(=$

8.315) $[\text{J}/(\text{K} \cdot \text{mol})]$ and the gas molecular weight W by

$$\text{R} = \text{R}_u/W. \tag{3.17}$$

3.3.3 Perfectly Stirred Reactor

The perfectly stirred reactor (PSR) is an idealized approximation of a system with strong mixing. In the limit of a perfectly mixed system, the chemical composition inside the system is homogeneous. Therefore, as long as the initial and/or boundary conditions are known, the chemical state is completely decided by the residence time [32]. For a flowing system, the Reynolds transport theorem gives the following integral equation:

$$\int_{\text{CV}} \frac{\partial}{\partial t} \left(\rho Y_k \right) dV + \int_{\text{A}} \rho Y_k \overline{u} \cdot \overline{n} \, dA = \int_{\text{CV}} \dot{\omega}_k W_k \, dV \tag{3.18}$$

where CV and A stand for the control volume and the entire bounding surface, respectively. Since the composition is uniform inside the PSR, the convective transport can be evaluated by considering only the inlet and outlet flows by

$$\frac{\partial}{\partial t} \left(\rho Y_k \right) V + \dot{m} \left(Y_k - Y_k^* \right) = \dot{\omega}_k W_k V, \tag{3.19}$$

where V is the total volume of the system, Y_k^* is the mass fraction at the inlet and Y_k is the mass fraction at the outlet which is the same everywhere in the system. For a constant mass flow rate condition, the equation can be further reduced to

$$\frac{dY_k}{dt} = \frac{\dot{m}}{\rho V} \left(Y_k^* - Y_k \right) + \frac{\dot{\omega}_k W_k}{\rho}. \tag{3.20}$$

The energy equation can be expressed as [32]

$$c_{\text{p}} \frac{dT}{dt} = \frac{\dot{m}}{\rho V} \sum_k Y_k^* (h_k^* - h_k) - \frac{1}{\rho} \sum_k h_k \dot{\omega}_k W_k + \frac{\dot{Q}}{\rho V}, \tag{3.21}$$

where h_k^* is the enthalpy at the inlet, $\dot{Q}$ is the heat transfer into the system, and c_{p} is the mass specific constant pressure heat capacity. For the purpose of analyzing the chemical time and the physical time, it is often desirable to define a residence time instead of a mass flow rate. The residence time is defined as

$$\tau = \frac{\rho V}{\dot{m}}, \tag{3.22}$$

where the mixture density is calculated from the ideal-gas law by

$$\rho = \frac{\text{p} W_{\text{mix}}}{R_u T}. \tag{3.23}$$

For a perfectly stirred reactor with a short chemical kinetic time scale relative to the residence time scale, the concentration at the outlet will approach the equilibrium condition. However, if the residence time is too short, the fluid exchange is fast and the system does not have enough time to react. This results in the outlet condition being more similar to the inlet conditions. The PSR is the most used ideal reactor for developing mechanisms. No spatial information is available, however this is important in many practical applications. Hence in order to study coupled chemistry and transport processes a model would is to have at least one dimension in order to include the transport effects.

3.3.4 Constant Pressure Reactor

For a simple constant pressure reactor, work done on the system needs to be considered by the boundary work

$$\frac{dW}{dt} = -\mathrm{p}\frac{dV}{dt} = -\mathrm{p}m\sum_k Y_k\frac{d\nu_k}{dt} - \mathrm{p}m\sum_k \nu_k\frac{dY_k}{dt}, \tag{3.24}$$

where $\nu_k = 1/\rho_k$ is the specific volume of the k-th species. With the enthalpy $h_k = e_k + \mathrm{p}\nu_k$ and using that the time rate of change of system energy in terms of all species can be written as [32]

$$\frac{dE}{dt} = m\sum_k Y_k\frac{de_k}{dt} + m\sum_k e_k\frac{dY_k}{dt} = \frac{dQ}{dt}, \tag{3.25}$$

where e_k is the specific internal energy of the k-th species, we can write the energy equation as

$$\sum_k Y_k\frac{dh_k}{dt} = -\sum_k h_k\frac{dY_k}{dt} + \frac{1}{m}\frac{dQ}{dt}. \tag{3.26}$$

The heat added to the system, can be expressed as

$$\frac{dQ}{dt} = \hat{h}A\left(T_\infty - T\right), \tag{3.27}$$

where $\hat{h}$ is the heat transfer coefficient, T_∞ is the ambient temperature, and A is the surface area where the heat transfer occurs.

In the constant pressure system, the specific internal energy can be written with constant pressure specific heat;

$$c_{\mathrm{p},k} = \left(\frac{dh_k}{dT}\right)_V \tag{3.28}$$

$$c_{\mathrm{p}} = \sum_k Y_k c_{\mathrm{p},k}, \tag{3.29}$$

where V is the volume of the system. Finally, the time rate of change of system energy is given by

$$\rho c_{\mathrm{p}} \frac{dT}{dt} = -\sum_{k} h_k \dot{\omega}_k W_k + \frac{\hat{h}A}{V}\left(T_\infty - T\right),\tag{3.30}$$

which describes the transient temperature and volume evolution for the constant pressure reacting system.

3.3.5 Molecular Diffusion

Given that the fluid under consideration in turbulent reactive flows is a mixture of multiple species in single phase, the mass fraction in one-dimensional flow can be written as

$$\frac{\partial}{\partial t}\left(\rho Y_k\right) + \frac{\partial}{\partial z}\left(\rho Y_k u_j\right) = \frac{\partial}{\partial z}\left(j_k\right) + \rho \omega_k.\tag{3.31}$$

The diffusion flux j_k for species k, consists of terms driven by three different forces; the temperature gradients (Soret effect), the concentration gradients (Fick's law), and the pressure gradients (pressure diffusion). The pressure diffusion, however, is often neglected in combustion applications [27]. This yields the diffusion flux

$$j_k = -\underbrace{\sum_{j}^{S} \rho D_{kj}\frac{dY_k}{dz}}_{\text{Fick's law}} - \underbrace{\frac{D_k^T}{T}\frac{dT}{dz}}_{\text{Soret effect}},\tag{3.32}$$

where D_{kj} and D_k^T are the multicomponent diffusion coefficients and the coefficient of thermal diffusion for species k, respectively.

Multicomponent diffusion

Equation (3.32), normally denoted as multicomponent diffusion, assumes that the diffusive flux j_k is proportional to every species gradient. This means that each species has a distinct contribution to the diffusive flux from the gradient of each species in the mixture giving a computational cost of $\mathcal{O}\left(S^2\right)$ per iteration. This complexity results from the need of calculating the $(S-1)^2$ diffusion coefficients matrix, which generally is not symmetric, $D_{kj} \neq D_{jk}$. The matrix of diffusion coefficients consists of the main and the cross diffusivities. The main diffusivity D_{kk} connects the flux of a component with its own concentration gradient, while cross diffusivities D_{kj} connect the flux of the component with the concentration gradients of other components. The values of diffusivities D_{kj} in a multicomponent mixture are not equal to the values $\mathbb{D}_{kj}$ in a binary mixture of the components k and j, due to the fact that the diffusion coefficients D_{kj} in multicomponent mixtures are not binary properties but are affected by the molecules of the third-party

species. The values of diffusion coefficients in multicomponent mixtures are the result of complex interactions between all the species, which makes it impossible to separate binary and multicomponent interactions.

Mixture-average diffusion

The mixture-averaged diffusion flux reduces the associated cost to $\mathcal{O}(S)$, with known errors in the range 10% [107]. Assuming that the diffusive flux for species k depends only on the gradient of species k yields:

$$j_k = -\rho \left(\frac{1 - X_k}{\sum_{j \neq k}^{S} \frac{X_j}{\mathbb{D}_{kj}}} \right) \frac{dY_k}{dz} - \frac{D_k^T}{T} \frac{dT}{dz}, \tag{3.33}$$

where $\mathbb{D}_{kj}$ denotes the binary diffusion coefficients and X_k the mole fraction of species k.

Constant diffusivity

A third alternative, reducing the cost to $\mathcal{O}(1)$, setting all the diffusion coefficients equal yields

$$j_k = -\rho D \frac{dY_k}{dz} - \frac{D_k^T}{T} \frac{dT}{dz}. \tag{3.34}$$

This third option, however, would not account for differential diffusion effects and is hence not implemented in the code.

3.3.6   Triplet map

The triplet map is thoroughly described in Chapter 2. From the formulas given there, it is clear that in 1D the effect of the triplet map is reasonable as long as we are willing to accept that the mapping is instantaneous and not continuous in time and that large eddies is not necessary followed by smaller once. Elaborating the last statement; the energy cascade refers to the transfer of energy from large scales of motion to the small scales, however as the triplet maps are independent, no energy is transfered between the scales. Consequently a large eddy does not give rise to smaller once, but might as well be followed directly by an arbitrary sized eddy, or none. As the size, time and spatial distributions of the triplet maps are represented by PDFs, we need to rely on assumptions used in the derivation of these, i.e. Kolmogorov theory/Richardson hypothesis and the scaling factor p. These artifacts are however within reason and inevitable in a stochastic representation of a turbulence framework. For 3D flows however, there are additional artifacts and assumptions. First, the three dimensional effect of a single eddy is represented as one-dimensional independent triplet maps. Second, as the turbulent diffusivity

provided to the model is given at the 3DCV-level, all turbulence within this level is assumed to be isotropic.

Comment for contemplation: On a DNS mesh, it would in principle be possible to formulate a 3D-LEM model with a three dimensional map similar to the 3D eddy effect by defining a 3D "triplet" map. The mapping could be constructed using the commonly agreed shape of 3D eddies of curved cylinders and in a corresponding manner to the 1D "triplet map" following the energy cascade for size distribution, taking D_T and p as input. If such a Lagrangian mapping is defined correctly it could, in stationary isotropic turbulence theoretically describe the entire turbulent advection and would, in theory, provide the same result as DNS on a similar mesh. The obvious disadvantage would however be that such an approach would require a computational cost of the same order of magnitude as DNS, as chemistry and diffusivity would have to be solved in all three spatial directions for all cells, i.e. DNS resolution.

3.3.7 The dimensional-decomposition approach, solving 3D as 3×1D

A chain is no stronger than its weakest link is a commonly heard phrase in team sports. All the above discussed assumptions, but the triplet map, are frequently used within CFD and derived from the reduction of mathematical equations. Further, where the triplet map is a conceptual construction based on the physical effect of eddies on scalar gradients, the 3×1D assumption mainly stem from the desire of having a three dimensional model, spatially resolved in three directions with a significant reduction in computational cost. Fulfilling all of the above without any trade off would be unreasonable to expect.

Factor three

Since there are three orthogonal stacks of LEM domains in the model framework, all three individual representations of the computational volume that are advanced concurrently (see Subsection 4.4.1), there are three times the mass within each control-volume (for the variable density approach the number might be slightly different, but should on average be 3). This again gives three times the amount of all extensive properties within the domain. To account for this, keeping the residence time constant, the overall transport rates are multiplied with a factor of 3.

As the turbulent diffusivity in LEM3D represents turbulent advection, we multiply it by the same factor 3 as the prescribed fluxes. It should be noted that this will neither effect the integral length scale L, nor the Kolmogorov scale, η.

Diffusion

The molecular diffusion is accounted for only within a single LEM domain, hence we only have 1D diffusion. In the current implementation of the model, diffusion is not affected by the factor 3 used to correct the turbulent advection. There is, however, a practice in similar models [8, 15], to account for the non-resolved diffusive contributions by a correction factor. That is, accounting for the non-resolved diffusive contributions is achieved deterministically by scaling the resolved diffusive transport terms by a factor. The representation of the filtered contribution of mass transport from the unresolved transport however depends on the configuration; if there is no preferred gradient, normally a factor 3 is adopted [8, 15].

Dilatation

The treatment of dilatation, either pure one-dimensional or distributed to all three directions, depend upon the approach used in Subsection 4.3.4. However, as long as the minimization by the least squares method (see Subsection 4.4.2) is applied for the advection and dilatation, the volume expansions from the reactions are distributed to all three directions through banking and hence treated as 3D.

Additionally, it is assumed that the numerical diffusion following from the regridding is acceptable. This is a widely used assumption.

3.3.8   Two-way coupling

One possible development path for LEM3D, other than pure post-processing of CFD or Particle Image Velocimetry (PIV)-measurements, is an iteratively coupling to a flow solver. The model flow chart is given in Figures 4.3 and 4.4 in Chapter 4, where the dashed lines indicate the two-way coupling, which potentially gets implemented. LEM3D will then provide updated scalar fields including density and temperature back to the flow solver, and the flow solver will provide updated flow fields back to LEM3D. This process is also described in previous work by Weydahl [108]. It is expected that the solution should be relaxed for better overall convergence.

3.3.9   Difficulties

It finally becomes evident that there are quite a few assumptions made and that some of them might be debatable for some flow configurations. It is important to realize that for every model there are assumptions to be made and to understand the prerequisites for each of the assumptions, and how these restrict its range of acceptability. The acceptability of a model will vary with the physical conditions and what it is used for. Obviously, there cannot exist a three dimensional model, spatially resolved in all three directions with full temporal resolution, intended to

have a significant reduction in computational cost compared to DNS without any trade-off. Hence, we should accept all the prerequisites for the model in order to achieve its benefits, i.e. assume that the artifacts from the above assumptions are worth the detail given and the computational speed-up compared to DNS. In many applications, temporal, spatial and size distributions is required information; if DNS is unaffordable, what do we do?
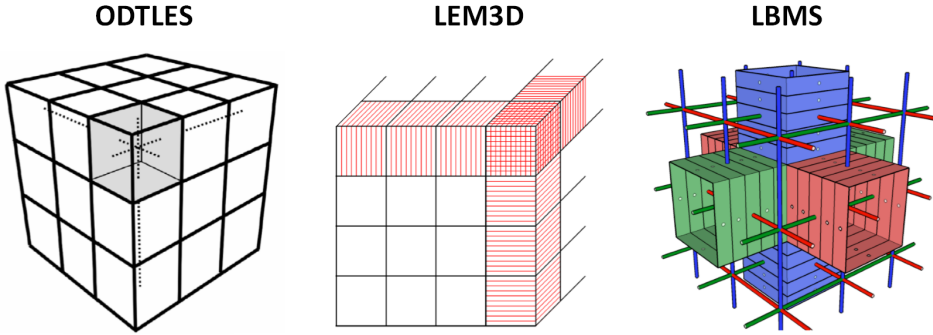
4. LEM3D

Since there is not yet a single, practical turbulence model that reliably can predict all turbulent flows with sufficient accuracy, the number of turbulence models and their complexity keeps getting extended. As is also the case for LEM3D, generalizations are continuously required to account for complex configurations. In the previous chapters general turbulence theory and approaches were discussed, the current chapter aims to fill the need of a thorough description and sufficient illustrations for LEM3D.

It should be noted that LEM3D has been developed guided by the principle of maintaining the distinctive feature of LEM, i.e. the separation between turbulent stirring diffusive mixing and chemical reaction as distinct processes subject to the inevitable compromises involved in modeling. As a consequence, scalars are not mixed at the molecular level by any other process than molecular diffusion, which rules out Eulerian treatment of advection and dilatation see subsection 4.4.1 and 4.3.4, respectively.

4.1 The 3×1D construction

LEM3D constitutes a three-array structure of LEM domains. Structurally, it is similar to to the ODTLES [90] and Lattice-Based Multiscale Simulation (LBMS) [98]. Figure 4.1 presents the illustrative geometries for the three models, ODTLES, LEM3D and LBMS. The leftmost figure present the geometry of ODTLES, where the illustrative geometry is taken from [90], but redrawn from its original form. The middle sub-figure presents the LEM3D geometry, described in detail in this section. The rightmost sub-figure presenting the three different directional "bundles" of LBMS is taken from [98], printed with permission from the author. The structure of the three models, first presented in [38], originally defined the 1D domains geometrically as line segments. Specifically, a line segment was corresponding to an edge of a linear stack of cubic control volumes. Later, it was pointed out that for numerical implementation it is preferable to interpret 1D model evolution

**ODTLES**   **LEM3D**   **LBMS**

Figure 4.1: The dimensional-decoupling concept illustrated for three different models based on the same decoupling assumption. From the left, ODTLES [90], LEM3D and LBMS [98]. The OTLES figure is taken from [90], but redrawn from its original form and the LBMS figure is taken from [98] and printed with permission from the author.

as occupying a volume of space, enabling a finite-volume numerical representation rather than the conceptual understanding of a line segment.

The LEM3D construction, illustrated in Figure 4.1 and previously described in [24, 25, 38, 88, 108], currently assumes that the global 3D flow domain is cuboidal, with coordinate bounds $0 \leq x \leq X$, $0 \leq y \leq Y$ and $0 \leq z \leq Z$. There is, however no physical restriction requiring a cuboidal control volume; this is for simplicity in the numerical implementation and might later be extended to a multi-block mesh.

The global flow domain is discretized in two distinct, but interdependent ways. The first consists of sets of three mutually orthogonal 1D LEM domain arrays. Each 1D domain spans the three-dimensional flow domain, and hence is its own one directional representation of the computational volume. 1D domains in different arrays intersect each other at regular intervals throughout the domain. The second discretization consists of a standard partitioning into rectangular control volumes, called 3DCVs, arranged such that a 1D-line intersection point resides at the center of each control volume, and that each control-volume face has a 1D-line that extends normal to the face and through its center.

Each LEM domain consists of $3\,\mathrm{LEM_{res}}$ computational cells, here named wafers. In other words, there are $\mathrm{LEM_{res}}$ wafers in each direction within a 3DCV. Without lose of generality take now a LEM domain from the i-direction, i.e. a LEMi-domain. By definition, each LEMi domain, has a sub-structure consisting of $N_i = X/\mathrm{LEM_{res}}$ 3DCVs. The first and the last 3DCVs each have one face interior to the x-domain, four contained in its respective side-faces, and one coinciding with
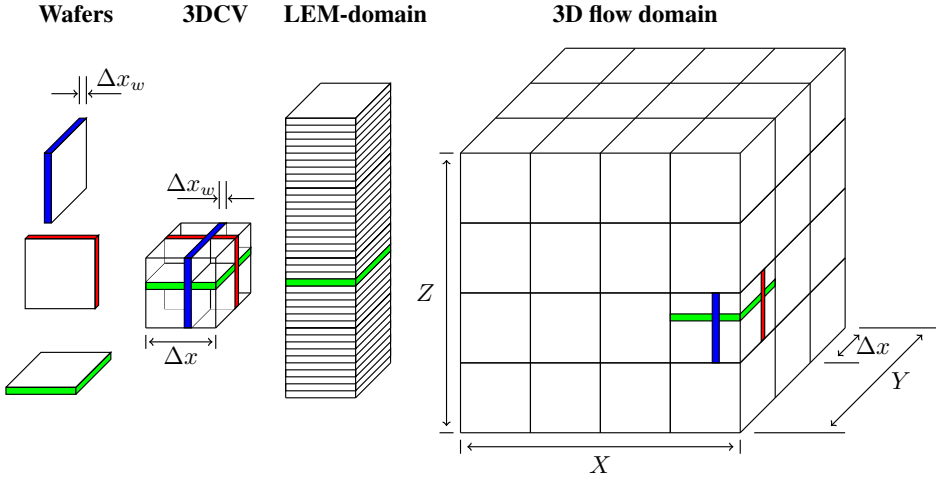
Figure 4.2: LEM3D geometric structures, from left to right: LEM wafers, 3DCV, LEM-domain and the 3D flow domain. The volumes of the geometrical structures are: $\Delta x_w(\Delta x)^2$, $(\Delta x)^3$, $(\Delta x)^3 N_d$, $d \in [i,j,k]$ and $X \cdot Y \cdot Z$, respectively.

an end-face of the LEMi-domain. The other 3DCVs in the x-domain each have two faces interior to the LEMi-domain and four contained in its respective side-faces. The union of non-interior 3DCV faces coincides with the surface of the LEMi-domain, this can also be seen in Figure 4.1. Further, as the LEM-resolution is supposed to be a sub-grid closure for RANS in the current implementation, the value of LEM_{res} must be large enough so that the smallest scales of the turbulent motion are adequately resolved, i.e. $\text{LEM}_{\text{res}} > \frac{\Delta x}{\eta}$. This constraint is relaxed by the introduction of the under-resolving factor, fac. Hence it is resolved down to fac·η in the entire domain. This implies that the number of wafers within the 3DCVs is $3\,\text{LEM}_{\text{res}} = 3\Delta x/\min(\text{fac} \cdot \eta)$. The total number of wafers in the problem is therefore $3\frac{\Delta x}{\eta}\frac{X \cdot Y \cdot Z}{(\Delta x)^3}$. This can be compared with the total number of points that would be required for a direct numerical simulation. For simplicity assume a cube domain ($X=Y=Z$), which is $\left(\frac{X}{\eta}\right)^3$, see table 4.1 for additional quantifications. The Reynolds number effect on number of computational cells for both DNS and LEM3D is illustrated in Figure 1.1.

In all three model formulations, three distinct flow solutions are time-advanced concurrently, each in one of the stack arrays. Each solution is a self-contained solution in that it does not exchange fluid or fluid properties with the other solutions, but the solutions are coupled through pre-described fluxes and banking described in Section 4.4.

	DNS	LEM			
	# cells	# CV	LEMres	# wafers	# LEM-domains
1D	$\frac{X}{\eta}$	$\frac{X}{\Delta x}$	$\frac{\Delta x}{\eta}$	$\frac{X}{\eta}$	1
2D	$\left(\frac{X}{\eta}\right)^2$	$\left(\frac{X}{\Delta x}\right)^2$	$\frac{\Delta x}{\eta}$	$2\frac{\Delta x}{\eta}\left(\frac{X}{\Delta x}\right)^2$	$2\frac{X}{\Delta x}$
3D	$\left(\frac{X}{\eta}\right)^3$	$\left(\frac{X}{\Delta x}\right)^3$	$\frac{\Delta x}{\eta}$	$3\frac{\Delta x}{\eta}\left(\frac{X}{\Delta x}\right)^3$	$3\left(\frac{X}{\Delta x}\right)^2$

Table 4.1: Number of computational cells in traditional CFD versus number of elements in the LEMiD construction, $i \in [1, 3]$, assuming a cube domain, i.e. $X = Y = Z$.

Each 3DCV further has associated its unique coordinates, (i, j, k) and velocities u_i, u_{i+1}, v_j, v_{j+1}, w_k and w_{k+1}. In LEM3D numerics, there are two important length scales, Δx and Δx_w (Sub-section 4.1.1), and multiple important time scales, Δt_{D}, Δt_{LEM} and Δt (Sub-section 4.1.2). These are, respectively, the LEM and RANS spatial discretization lengths and the diffusive, turbulent advective and the advective time steps.

4.1.1 Length scales

Δx_w : Thickness of a wafer, globally defined. Implemented as $\Delta x_w = \mathrm{fac} \cdot \min_{\{\forall\,3\mathrm{DCV}\}}(\eta, \eta_B)$, where η_B denotes the Batchelor scale and $\min_{\{\forall\,3\mathrm{DCV}\}}$ is the minimum over all 3DCVs.

η : Kolmogorov scale, the scale at which viscosity dominates and the turbulent kinetic energy is dissipated into heat. It is prescribed to the model locally at each 3DCV and locally restricts the smallest size of triplet maps occurring in the given 3DCV.

Δx : The length of each edge in a 3DCV, globally defined. Generally Δx should be large for computationally efficiency, but small enough to represent the mean flow scales with sufficient resolution.

L : Integral scale of the triplet map upward bounding the triplet maps with center in the given 3DCV, defined and prescribed within each 3DCV.

X, Y, Z : Outer dimensions of the global flow domain.

4.1.2 Time scales

$\Delta t_{\mathbf{D}}$: Diffusion time step given by the linear stability condition $\Delta t_D = \Delta x_w^2 / D_{max}$. Here, $D_{max} = \max(D_{M_i,l})$ and D_{M_i} is the mixture-averaged diffusion coefficient of species i, locally defined for each wafer and dependent on composition.

Δt_{LEM} : Occurrence of the next triplet map, locally defined within each 3DCV.

Δt : Advective time-scale, calculated from the prescribed CFL condition through $\Delta t = \mathrm{CFL}\,\Delta x / \max(|\boldsymbol{u}|)$, globally defined.

4.1.3 Integers

fac : Under/over-resolving factor based on the smallest scale in a turbulent reacting flow, i.e. $\min_{\{\forall\,3\mathrm{DCV}\}} (\eta, \eta_B)$. It is prescribed the model as a global integer and is related to the smallest scale and the wafer width by $\Delta x_w = \mathrm{fac} \cdot \min_{\{\forall\,3\mathrm{DCV}\}} (\eta, \eta_B)$.

$k_{\mathbf{min}}$: Smallest implemented size of the triplet map given by $k_{\min} = \max(2, \lfloor \Delta x_w / \eta \rfloor)$, where $\lfloor \cdot \rfloor$ denotes the greatest integer below or equal to $\cdot$.

$\mathbf{LEM_{res}}$: Number of wafers in each direction of a 3DCV, globally defined, given by $\mathrm{LEM_{res}} = \lceil \Delta x / \Delta x_w \rceil$, where $\lceil \cdot \rceil$ denotes the smallest integer above or equal to $\cdot$.

$\boldsymbol{N_d}, d \in [i, j, k]$: number of 3DCVs in direction d of the global flow domain.

$k_{\mathbf{max}}$: Largest numerical size of the triplet map, defined within each 3DCV as $k_{\max} = \lceil L / \Delta x_w \rceil$, where L is the integral length scale prescribed within each 3DCV.

$\boldsymbol{N_{\mathbf{LEM}_d}}, d \in [i, j, k]$: Number of wafers in a LEM-domain of direction d, implemented as $N_{\mathrm{LEM}_d} = N_d \cdot \mathrm{LEM_{res}}$.
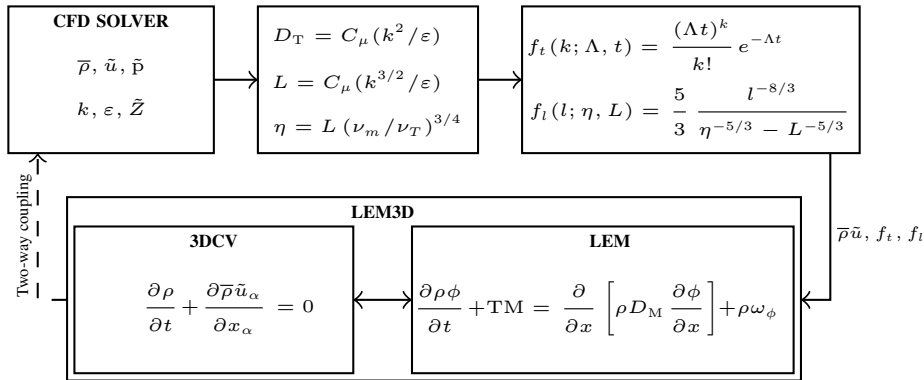
Figure 4.3: Code structure of LEM3D displaying the main equation(s) solved in each part of the code.

4.2 The model flow

In order to give the reader a visual understanding of the model flow, this section presents conceptual illustrations of the overall model flow. Figure 4.3 shows in a compact form the main equation(s)/scalars solved/found during each of the code blocks in LEM3D, while Figure 4.4 on the contrary shows the model-flow in a visual manner. Each of the boxes in Figure 4.4 has been assigned their own part of the thesis describing the background, implementation and consequences. The list below, order based on the model flow, states the title of each box and their corresponding (sub-)section.

CFD/Experiments	:	Chapter 3
Turbulent quantities	:	Section 3.2
Scalar initialization	:	Section 4.5
Turbulence initialization	:	Section 2.2
Chemical reactions	:	Subsection 4.3.3
Triplet map	:	Subsection 4.3.1
Dilatation	:	Subsection 4.3.4
Lagrangian displacement	:	Subsection 4.4.1
Rotation	:	Subsection 4.4.4
Two-way coupling	:	Subsection 3.3.8
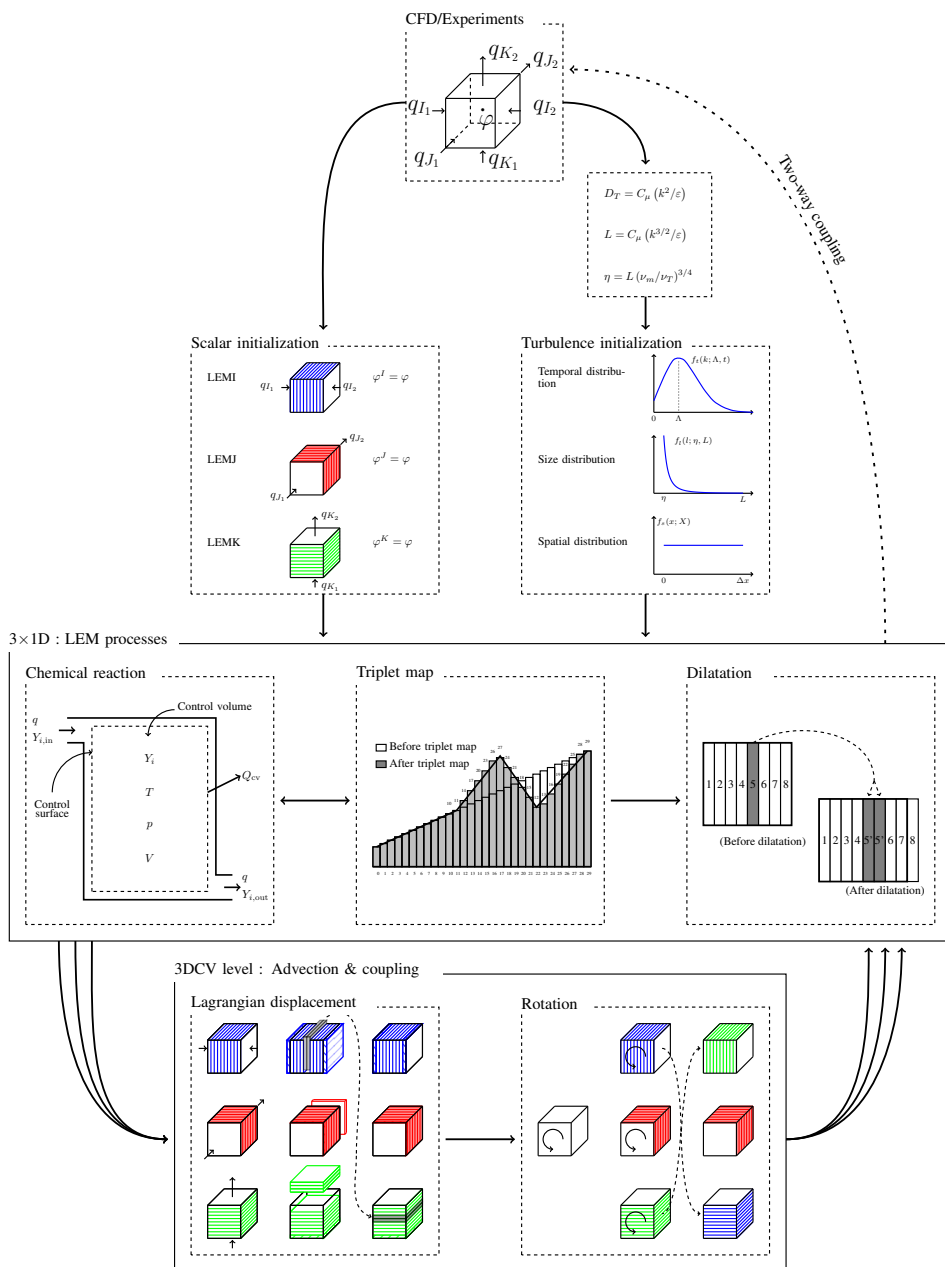
Figure 4.4: LEM3D - the concept structure
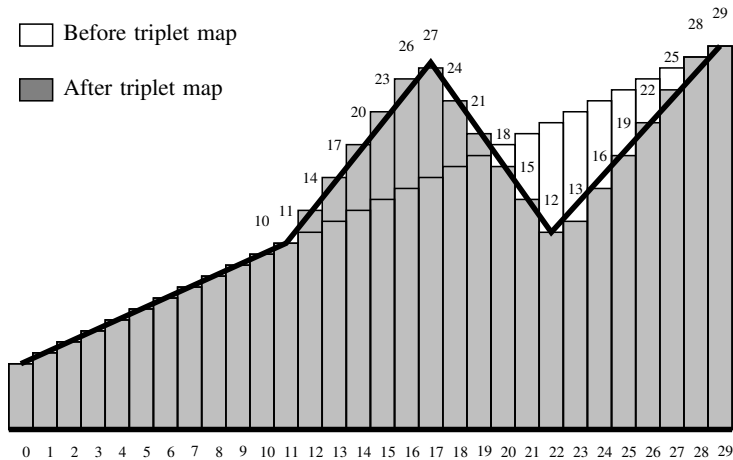
Figure 4.5: Triplet map implementation, illustrating the shift in indexes for a triplet map of size, $l = 18$ (i.e. $k = 6$), with $x_0 = 11$ and center at $x_0 + l/2 = 20$.

4.3 One Dimensional Operations

This section describes the operations done at each of the one dimensional domains of all three spatial directions. The mathematical equation solved is the reaction-diffusion equation

$$\frac{\partial \rho \phi}{\partial t} + \text{TM} = \frac{\partial}{\partial x}\left[\rho D_\text{M} \frac{\partial \phi}{\partial x}\right] + \rho \omega_\phi. \tag{4.1}$$

In addition the diffusive-reactive time advancement of Eq. (4.1) is punctuated by randomly occurring stirring events. These stochastic events, denoted triplet maps and represented by TM, emulate the effects of individual turbulent eddies on the scalar concentration fields. The mathematical background for the triplet maps are discussed in Section 2.2.

4.3.1 Triplet Map

The turbulent stirring is modeled as stochastic rearrangement events relating the LEM fluid-elements diffusion to random walks of particles. Each rearrangement event is interpreted as the action of a single instantaneous eddy on the one-dimensional scalar field. Each eddy is described by three numbers, each drawn from its corresponding probability density function. The three parameters represent the size, the location and the time instance for the eddy, as described in Section 2.2. As all the mathematical formulations have been discussed in Section 2.2, we restrict this section to a discussion of the implementation and the concept.

Once the time of the triplet map event is reached, punctuating chemical- and diffusion-processes, and the event size and location are determined. The rearrangement event is implemented using the triplet map Definition 1. This mapping first creates three copies of the selected segment, increases the spatial gradients of the copies compressing them by a factor of three, and then reversing the middle copy. Finally, the original segment is replaced by the newly mapped segment. Each mapping event requires at least six LEM wafers (a map of size three is the identity mapping) so that on a discretized domain, the smallest eddies, η, should be resolved by six LEM wafers to fully resolve the turbulent quantities. It should be noted that when $\eta_B << \eta$, we should resolve the wafers based on η_B. An illustration of the triplet mapping and the competing actions of reaction and diffusion on a mapped segment of a reacting scalar are shown in Figure 1 in Article I.

As the given segment is tripled by the triplet map, the discrete implementation of the triplet map is restricted to segments which are of length $3k$, i.e. with indexes $[1, 2, \ldots, 3k]$, where k is a positive integer ($k \in \mathbb{N}$). The resulting change of indexes by a triplet map of size $3k$ centered at $3k/2$ is $[1, 4, 7, \ldots, 3k - 2, 3k - 1, 3k - 4, 3k - 7, \ldots, 2, 3, 6, 9, \ldots, 3k]$. As discussed above the smallest triplet map contains six wafers, i.e. $k = 2$ is set as the lower limit. Figure 4.5 illustrates the discrete implementation of the triplet map for a map with $k = 6$, i.e. eddy size $l = 18$, with $x_0 = 11$ and center at $x_0 + l/2 = 20$.

The mapping event has multiple attributes analogous to turbulent convection. First and foremost compared to mixing models relying on the gradient diffusion assumption, the triplet map approach makes turbulent advection distinguishable from molecular diffusion. Secondly, the mapping increases the number of crossings of a single scalar value, which may be interpreted as an increase in surface area caused by flame wrinkling. Turbulent scaling laws built into the model also cause the strain rate and the rate of growth of flame surface area to be of the correct order of magnitude [36]. The triplet map is unfortunately not able to capture all turbulent motion, e.g., the effect of rotational folding of the flame by turbulent eddy motions stays uncaptured [15].

4.3.2 Diffusion

In the current formulation, detailed and finite-rate chemistry is fully implemented from CHEMKIN II. The implicit, backward Euler time integration is employed. The properties of the wafers are defined, transported and reacted at the wafer center, making Eulerian treatment of diffusion the natural option. The diffusion time step used (in the time integration), Δt_D is given by the linear stability condition;

$$\Delta t_D = (\Delta x_w)^2 / D_{max}, \tag{4.2}$$

where Δx_w denotes the LEM wafer size and

$$D_{max} = \max(D_{Y_i,l}).$$ (4.3)

In the above equation, $D_{Y_i,l}$ normally is set to be the mixture-averaged diffusion coefficient of species i at the lth cell location of a given LEM domain. However, as described in Subsection 3.3.5, $D_{Y_i,l}$ depends upon the choice between constant, mixture-averaged or multicomponent diffusion.

Second order numerical accuracy is ensured for the diffusion term by applying central schemes between the wafers. The equation is a tridiagonal linear equation system

$$-\varphi_{i-1}^{n+1} + \varphi_i^{n+1}(\frac{1}{\text{CFL}_D} + 2) - \varphi_{i+1}^{n+1} = \frac{\varphi_i^n}{\text{CFL}_D},$$ (4.4)

where CFL_D is the diffusive Courant-Friedrichs-Lewy number given as

$$\text{CFL}_D = \frac{D_{max}\Delta t_M}{(\Delta x_w)^2},$$ (4.5)

with Δt_M being the molecular time-stop. For very stiff chemistry, the characteristic chemical time scale associated with the reaction rate may be smaller than the diffusion time scale which could lead to inaccuracies. In this case, the value of D_{max} should be reduced accordingly. The equation system in Eq. (4.4) must be solved by direct or iterative methods. In the current work and code, the Thomas Algorithm or better know as Tridiagonal Matrix Algorithm (TDMA) [101] is employed. The implicit scheme is unconditionally stable for any CFL-number, but the time accuracy is reduced by increasing the time step, Δt_M, with first order accuracy, i.e. $O(\Delta t_M)$.

4.3.3 Reaction

Due to the resolution LEM3D is intended for, i.e. down to the Batchelor scale η_B, the wafers are considered as perfectly stirred reactors (see Subsection 3.3.3). Detailed finite-rate chemistry is solved implicitly at the diffusive timescale, Δt_M. The current code imposes a global pressure at 1 atm, while locally at the wafer scales, the pressure is either kept constant, allowing for volume expansions and requiring re-gridding, or accumulated and released in integer steps. Please see Subsection 4.3.4 for the alternatives.

It should be noted that due to computational restrictions, conducted simulations may often be under-resolved, i.e. the smallest scales resolved is $\min_{\{\forall 3\text{DCV}\}} (\eta, \eta_B) \cdot$ fac and the assumption of a perfectly stirred is weaker. If the under-resolving factor fac is large another turbulence-chemistry approach like, e.g., EDC (see subsection 3.2.2), might have to be considered as a subgrid model within LEM.

4.3.4 Dilatation and thermal expansion

For configurations where thermal expansion from heat release is negligible, the extension of LEM from a turbulence mixing model to a combustion model is straightforward. This was illustrated by e.g. Frankel et al. [19], who calculated binary scalar mixing and isothermal reaction in homogeneous turbulence, and the successful simulation of reactive mixing layer of nitric oxide and ozone by Kerstein [35].

If thermal expansion from heat release cannot be neglected, additional assumptions need to be added as the local pressure would accumulate. All treatments of thermal expansion inevitably introduce artificial diffusion, although this decreases with the resolution. In the LEM framework it is common to preserve the wafer size as the triplet map originally is intended for and developed based on computational cells of equal size. Three approaches accounting for thermal expansion are discussed below.

The first approach, used in previous versions of LEM3D, and still optional in the code, where handling of thermal expansion is implemented to minimize artificial diffusion [88, 108] is integer step creation. The approach, described in [62], is illustrated in Figure 4.6, creating new cells at integer steps based on an expansion criteria.

A second way, yet not implemented in the code, but available with minor configurations, is to account for dilatation in an Eulerian manner, i.e. let the expansion induce a flow out of the fluid cell. The approach described in [13] was first introduced for the LEM framework in [69].

The third approach, frequently used and currently the preferred approach, is to increase the cell volume and perform a re-gridding operation before every triplet map event [16, 93].

Common for the integer creation and the re-gridding procedure is that they increases the number of cells throughout the simulation, while for the Eulerian approach the pressure-induced flow is handled by the differential scheme in use. In order to keep the wafer number constant, within each 3DCV, some wafers need to be flushed out, as seen in Figures 4.6 and 4.8. Both of the Lagrangian approaches are currently applied precursory to each advective time-step. The alternative would have been to perform thermal expansion precursory of each triplet map. This option has been investigated and tested, but no significant difference is seen, so the dilatation frequency is lowered in order to reduce computational cost.

All three approaches are given a separate description below. Their performance,

however, is discussed in the next section 4.4.1, as it is challenging to isolate the effect of dilatation routine from the overall wafer displacement.

Integer step creation
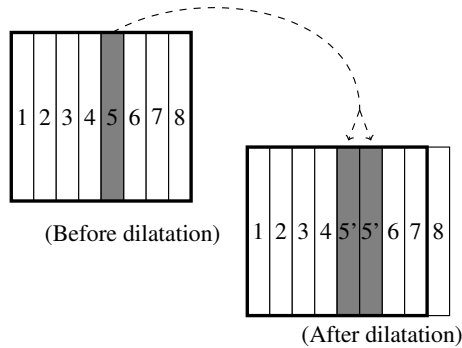
Figure 4.6: Dilatation by integer step creation for wafer number 5 when the local pressure exceeds the background pressure by a integer fraction.

When a wafer is to be expanded, based on a given expansion criteria, it is extended by i multiples of its volume by creating $i+1$ new copies of the wafer, and replacing the original wafer by the $i+1$ copies. The resulting dilatation gives displacement of surrounding wafers, since the number of wafers is to be kept constant within a 3DCV. The new wafers adopts a new local pressure $p = p_0/(i+1)$, where p_0 is the pressure from when the last expansion occurred. The process is illustrated in Figure 4.6 for $i = 1$. The expansion criterion used, is based on the thermodynamic pressure, assuming that the pressure can be estimated from the equation of state:

$$p^+ = \rho RT, \tag{4.6}$$

where T is temperature and R is the specific gas constant for the mixture. The superscript, $^+$, signifies that the pressure solely acts as an indicator for when the expansions should occur. The threshold for expansion is based on the local pressure of a wafer exceeding the background pressure by a given factor, normally set to 2.

As discussed above, the creation of new wafers leads to displacements of wafers located in the same LEM domain. For LEM domains oriented in the I-direction, the wafer creation always shift the neighboring wafers downstream, while if the LEM domain is oriented in the J- or K-direction the wafer creation adds i to indices of the wafers located in the opposite direction of the 3DCV mid-point.

(Before dilatation)   (After dilatation)
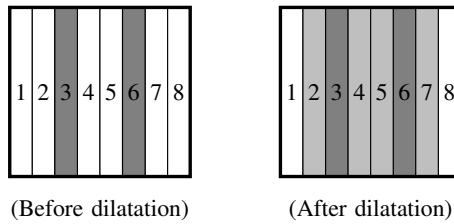
Figure 4.7: Eulerian approach of dilatation, the pressure will be equalized according to the scheme, here central difference is applied.

Eulerian approach

The Eulerian approach, using either finite volume or finite differences, differs from the other two approaches which follows a Lagrangian wafer displacement. It would, if implemented in the current code, be natural to use central difference schemes between wafers in treatment of the thermal expansion, as an expanding shape move radially outwards. Since diffusion already is discretized by central differences (see Subsection 4.3.2) it can conveniently be integrated with the Eulerian (expansion) approach. The approach assumes low Mach number and equalizes the pressure through creating a constraint on the velocity, $\mathcal{U}$, based on the pressure dependence on chemical reactions, heat conduction and species diffusion [69]:

$$\mathcal{U} = -\frac{1}{\rho c_p T}\left[\frac{\partial q}{\partial x} + \sum_s j_s \frac{\partial h_s}{\partial x}\right] - \frac{1}{\rho}\sum_s\left[\frac{W}{W_s}\frac{\partial j_s}{\partial x}\right] + \frac{1}{\rho}\sum_s\left[\frac{W}{W_s} - \frac{h_s}{c_p T}\right]\dot{\omega}_S, \tag{4.7}$$

where j_s is the species diffusive mass-flux (dependent on the choice of approach in subsection 3.3.5), h_s is the enthalpy of species s including the heats of formation, and $W = \left(\sum_s Y_s/W_s\right)^{-1}$.

Further, in the zero-Mach-number limit we can from the energy equation [13] derive the velocity driven by the pressure gradient from:

$$\frac{\partial u}{\partial x} = -\frac{1}{\gamma \mathrm{p}}\frac{d\mathrm{p}}{dt} + \mathcal{U}, \tag{4.8}$$

where $\gamma = c_p/c_V$ is the ratio of the specific heats.

Re-gridding

In the current model for variable density re-gridding is employed. The approach accounts for thermal expansions by increasing the cell volume, such that the local wafer pressure $\mathrm{p}_w = \rho_w RT$ agrees with the background pressure, followed by a re-gridding, such that each wafer is returned to its initial volume. The routine is employed precursory to every advective time step.
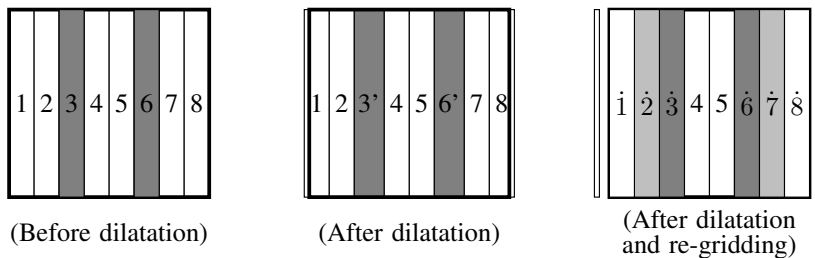
Figure 4.8: Dilatation and re-gridding to conserve a constant pressure and constant volume of the wafers.

In the I-direction all additional wafers are shifted upstream, and the volume- or mass-flux crossing the boundaries are stored and compensated for during the advection routine, see Subsection 4.4.1. Similarly, the fluxes are stored for the J- and K-direction, but here the the wafers are shifted so that the volume- or mass-fluxes are equal at both LEM-domain-boundaries. It might seem natural to have similar treatment in the three directions as dilatation acts in all directions, the different treatment is however a necessity by the dimensional decomposition approach. In for instance jet-configurations, wafers would get expanded upstream and into the nozzle during the thermal expansion and re-gridding procedure, if equal volume- or mass-fluxes was applied at both LEM-domain-boundaries. Later, the same wafers would, by accommodating the inlet conditions, be advected back through banking and advection (see Subsection 4.4.1), leading to numerical instabilities.

4.4 Three Dimensional Operations

This section describes the operations done at the three dimensional level, i.e. operations in and between the 3DCVs. The mathematical equation solved is

$$\frac{\partial \rho}{\partial t} + \frac{\partial \overline{\rho} \tilde{u}_\alpha}{\partial x_\alpha} = 0, \tag{4.9}$$

and the numerical treatment of it, denoted the advective coupling, is described in Subsection 4.4.1. An additional coupling between the domains, the auxiliary coupling, was found necessary in [88]. The auxiliary coupling has a frequency following the probability

$$p_{\text{rot}} = \frac{3}{2} \text{C}_{\text{rot}} \text{CFL}_{\text{3DCV}}. \tag{4.10}$$

The auxiliary coupling is thoroughly described in Subsection 4.4.4.
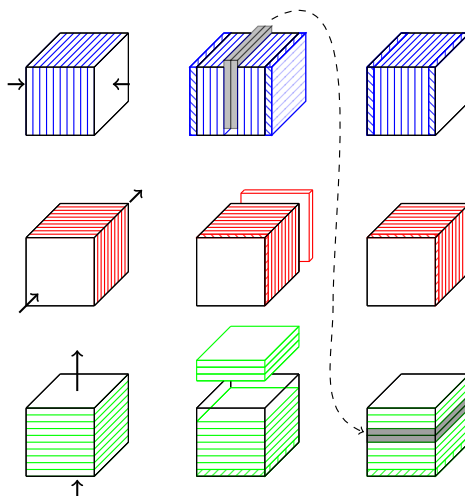
Figure 4.9: The advective coupling illustrated. The blue, red and green wafers represents the LEMi-, LEMj- and LEMk-domains, respectively, while the arrows indicate the fluxes into/out of the domains. Single wafers are advected into the 3DCV from each side of the i-oriented domain, a single wafer is advected into and out of the LEMj-domain, while a single wafer is advected into the LEMk-domain while three are advected out. The last advection of the wafers out of the green domain is facilitated through advectional flipping of the two excess wafers from the LEMi-domain.

4.4.1 The Advective Coupling

The displacement of LEM wafers are based upon the 3DCV prescribed mass-fluxes $\overline{\rho \boldsymbol{u}}$ following the continuity equation (Eq. (4.9)) and prescribed from a flow solver or experiments. Further, the displacements take dilatations from reactions into account through minimization of deviations (in the constant density frame work defined as banking). Typically, the displacements involve transfer of wafers among the differently oriented LEM domains intersecting each 3DCV. Conservation of volume is enforced by requiring the displacements of wafers in and out of each 3DCV to obey the equation

$$\sum_{l=1}^{N_{\text{faces}}} \delta_l = 0, \tag{4.11}$$

where δ_l denotes the integer number of wafer displacements across the 3DCV faces. Thus a constant number of wafers is kept within each 3DCV, similarly to what is seen in Eulerian PDF schemes using Monte Carlo method [9, 10].

An illustration of the 3-dimensional advection operation for a single 3DCV is

shown in Figure 4.9. Here the blue, red and green wafers illustrate the LEMi-, LEMj- and LEMk-domains, respectively, and the arrows indicate the fluxes into/out of the domains. In the current example single wafers are advected into the 3DCV from each side of the i-oriented domain, a single wafer is advected into and out of the LEMj-domain, while a single wafer is advected into the LEMk-domain while three are advected out. The middlemost three figures illustrate the need of advectional flipping, where the LEMk-domain (green), lack two wafers while the LEMi-domain (blue) have two in excess. These two are extracted from the center of the LEMi-domain, flipped and inserted directly downstream (based on the net k-directional flux) of the center of the 3DCV.

The transfer of wafers represents the fluxes normal to control-volume faces, which are prescribed either from experiments or a flow solver. The prescribed fluxes are implemented in a Lagrangian sense, for either volume- or mass-fluxes in between domains associated with control volumes that share a common face. For a flux q_l, where $l \in [1, N_{\text{faces}}]$ denotes the face normal to the flux, we define the prescribed displacement $\gamma_l \in \mathbb{R}$ as

$$\gamma_l = \frac{3q_l \Delta t}{(\wp V)_w},$$ (4.12)

q_l either denotes volume or mass-fluxes, and

$$(\wp V)_w = \begin{cases} V_w & q_l = \dot{V} \\ \sum_n^{N_l} V_n \rho_n & q_l = \overline{\rho \dot{V}} \end{cases},$$ (4.13)

where N_l are the indices of all wafers to be displaced such that $(\wp V)_w \leq 3q_l \Delta t$, and V_n the volume of a wafer, i.e. $V_n = (\Delta x)^2 \Delta x_n$. The factor 3 follows from the assumption described in Subsection 3.3.7. The definition Eq. (4.12) is a generalization of the prescribed displacement given for constant density flux in [108], where constant density was assumed, hence there were no difference between volume- and mass-fluxes; $q = \overline{\rho \dot{V}} = \rho \dot{V}$. Further, γ_l would reduce to $3\overline{u}_l \Delta t / \Delta x_w$ as $q_l = \overline{u}_l (\Delta x)^2$.

As $\gamma_l \in \mathbb{R}$ its discrete approximation will vary from time step to time step, unless $\gamma_l \in \mathbb{Z}$. Further, the volume within a 3DCV is kept constant by $\sum_l \delta_l = 0$ and as only volume-flux is required during the Lagrangian displacement, the approach might yield a deviation between the prescribed mass-flux and the mass fluxed in LEM3D. This is mainly observed in regions with volume increase through heat release from reactions, and downstream of these. It has also been observed in regions where the counter-gradients are strong, as seen in e.g. the effort of simulation of the jet in cross-flow configuration [23] mentioned in Chapter 6.

The associated deviation for each 3DCV face is denoted as Ξ_l, while the associated deviation for a 3DCV is denoted Ξ_{flux}. They are both defined as the difference

between the prescribed mass-fluxes and the actual mass fluxed by LEM3D given by

$$\Xi_{\text{flux}} = \sum_{l=1}^{N_{\text{faces}}} \Xi_l = \sum_{l=1}^{N_{\text{faces}}} \left(\Delta x_w \sum_{n=1}^{N_l} \rho_{ln} - \overline{\rho\,u_l}\Delta t \right), \qquad (4.14)$$

where N_l is the number of wafers fluxed over face l, and ρ_{ln} denotes the density of the wafer n fluxed into or out of the 3DCV at face l. The given deviation is an integral part of the current implementation in the variable density framework and in the presence of chemical reactions. This deviation is a generalization of the previous defined banking formulation for constant density and volume-flux [88, 108]. An important difference however, is that in variable density approaches the sum of all deviations might grow with $O(t)$, here t is the time of a transient LEM3D simulation; this however only occurs when the LEM3D solution deviates, on average, from the prescribed solution.

In order to adapt the deviations Ξ_l and minimize them, an investigation of various iteration procedures, in combination with least-squares methods to minimize the deviations at each 3DCV cell face, has been performed in Article II.

From the previous implementation of the code [108], Weydahl et al. concluded based on volume-flux results that the combination of the banking method, which is non-conservative in density varying flows, and the continuity equation (4.9) led to deviations that accumulated in the stream-wise direction. They further proposed to base the advection method on Ξ_l, namely the mass-flux deviations, which currently is the approach in use. These two approaches, mass- and volume-flux, together with a third approach proposed by Kerstein [39] are visited in the current section.

The rest of this section is structured in the same manner as implemented in the code. Firstly, the different flux approaches are described. Each of the descriptions includes an example on their intended use. All of the examples applies the given advection routine to a single LEM-domain consisting of 3 3DCVs, with $\text{LEM}_{\text{res}} = 4$. Secondly, the optimization algorithm for a single 3DCV is described. Lastly, the iteration scheme alternatives are presented. The selected iteration scheme is applied layer-wise and sets the order of 3DCVs at which Ξ_{flux} for the given 3DCV is minimized by the optimization algorithm. After the above operations, final values of $\delta_l\ l \in [1, N_{\text{faces}}]$ for each 3DCV are set and the wafers are displaced.

Volume-fluxes

The first proof of concept for LEM3D [108] was developed for a constant density framework, and hence volume-fluxes was an natural option in its simplicity of implementation. Later the volume-fluxes were also tested [108] and used for the
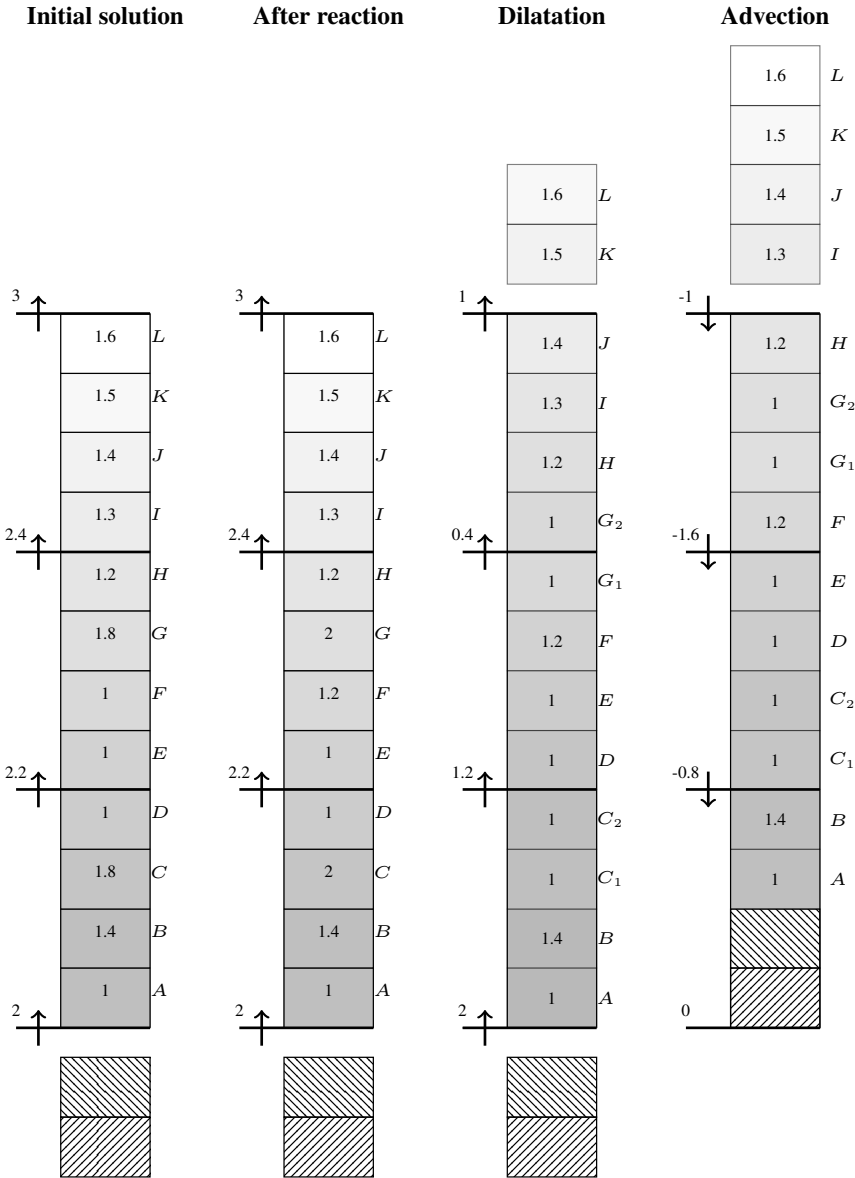
Figure 4.10: Advection for a domain with the volume-flux approach with dilatation at integer steps and banking of volume-fluxes at each cell boundary.

variable density flows in combination with dilatations implemented by the integer creation approach, described in Subsection 4.3.4. Banking occurs at each 3DCV cell face and for the constant density approach $\sum_{l}^{N_{\text{faces}}} \Xi_l = 0$, hence no deviation from the prescribed flow field will exist [108].

Figure 4.10 illustrates the procedure used for the variable-density framework, i.e. with integer creation and volume-flux for a single LEM domain. As explained in Section 4.3.4, the wafer expands when the local pressure p^+ exceeds two times the background pressure p. In the example, there are two wafers to be advected into the domain from the boundary. Each of the wafers in the domain has its one pressure ratio (p^+/p) given at its center and are identified by a capital letter on the right-hand side of the wafer. The volume-fluxes are given left of the arrows. In the initial solution, the leftmost column, there is already accumulated some local pressure. After the reaction, second column, we see that in two of the wafers the local pressure has exceeded the expansion criteria. Hence, in the third column, dilatation, wafer C and G are doubled, reducing the local pressure ratio to one. Lastly, in the rightmost column, the wafer displacement based on the prescribed fluxes are conducted.
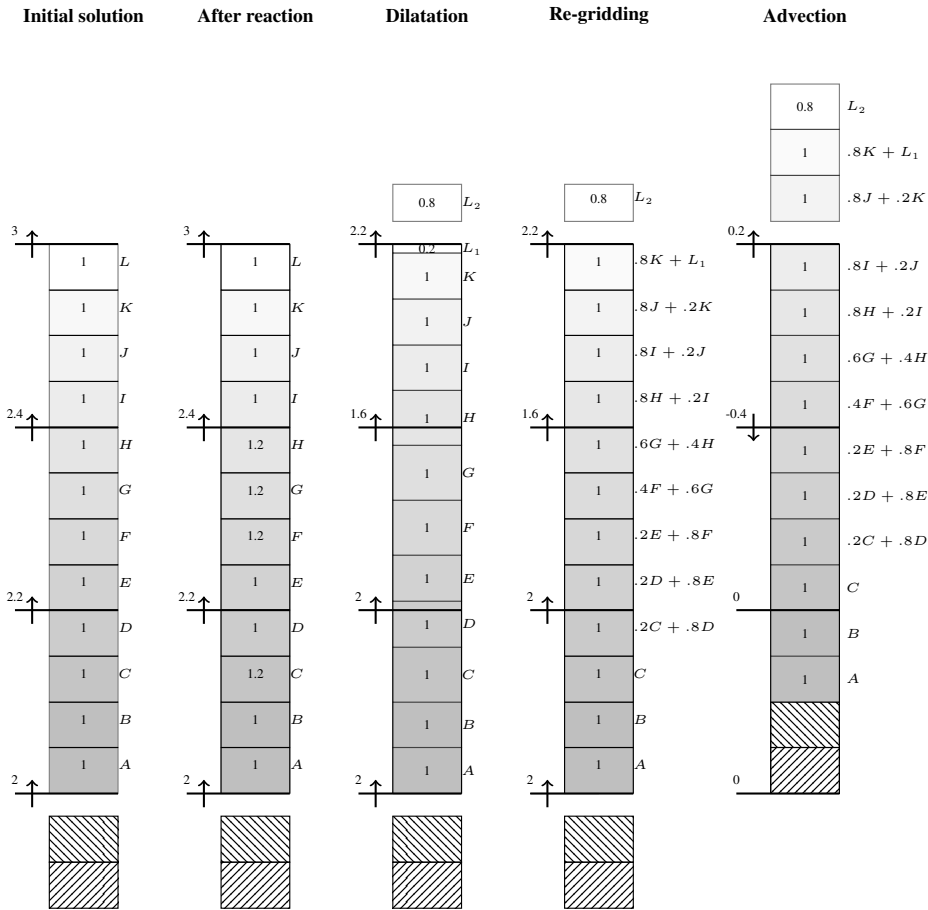
Mass-fluxes

As soon as variable density flows came into consideration it was natural to account for wafer displacements through prescribed mass-fluxes. At the 3DCV faces, Ξ_l are banked and stored. However, as LEM3D requires a constant number of wafers within each 3DCV, i.e. a constant volume, issues might arise in connection with dilatations. For the present work and the intended use of LEM3D with mass-fluxes, re-gridding with volume expansions are done before each advection step. Hence the local pressure p^+ always equals the global pressure p before and after the advection routine.

Figure 4.11 illustrates the intended use of the mass-flux routine with re-gridding for a single LEM-domain. Mass-fluxes $(\Xi_i l + q_i)$ are described with a decimal number left of the arrow, indicating their direction. In the center of each wafer the local pressure ratio is given and the identification of the wafers is shown next to them by a capital letter. The initial solution, as expected, only consists of wafers with pressure ratio 1. After reaction, we observe that the pressure ratios has increased, the pressure ratio is normalized through dilatations, affecting the mass-fluxes. Then re-gridding is performed before the wafer displacement occur.

Thermodynamical and geometrical volume

A third alternative method, combining advection, dilatation, banking and re-gridding was suggested by Kerstein et al. [39], it is motivated by the intended matching of average volume and mass-fluxes for LEM3D and the prescribed flow field. It should be noted the method has not yet been implemented, hence its performance is currently unknown. The method strictly speaking based on volume-fluxes but has an additional assumption in its construction resulting in a quite different approach than the two above. Instead of banking through Ξ, Kerstein [39] suggested bank-

54

Figure 4.11: Iteration routine for use of re-gridding before each advection routine. The arrows here indicates the prescribed mass-fluxes. Each wafer has a constant volume before each advective step.

ing locally within the wafers by differencing between the thermodynamical, V_w^t, and the geometrical volume, V_w^g, of the wafer. The volume of the wafer is given by $(\Delta x)^2 \Delta x_w$, Δx_w being the wafer width. In the mass-flux approach $V_w^t = V_w^g$. Wafer displacement is here calculated based on the geometrical volume, while the diffusion and reaction processes use V_w^t, calculated form the equation of state. In order to account for the increase in volume-fluxes after reactions, the thermodynamical volume is released when required. This results in the correct amount of thermodynamical volume to be fluxed and a full independence of the iteration scheme (see Subsection 4.4.3 for a description of the iteration schemes). The procedure is suggested to relax towards $V_w^t/V_w^g = 1$, hence all wafers within the same

LEM-domain of a 3DCV will have to obey either $V_w^t/V_w^g \geq 1$ or $V_w^t/V_w^g \leq 1$ after advection. The suggestion is made in order to reduce large local variations in thermodynamical volume.
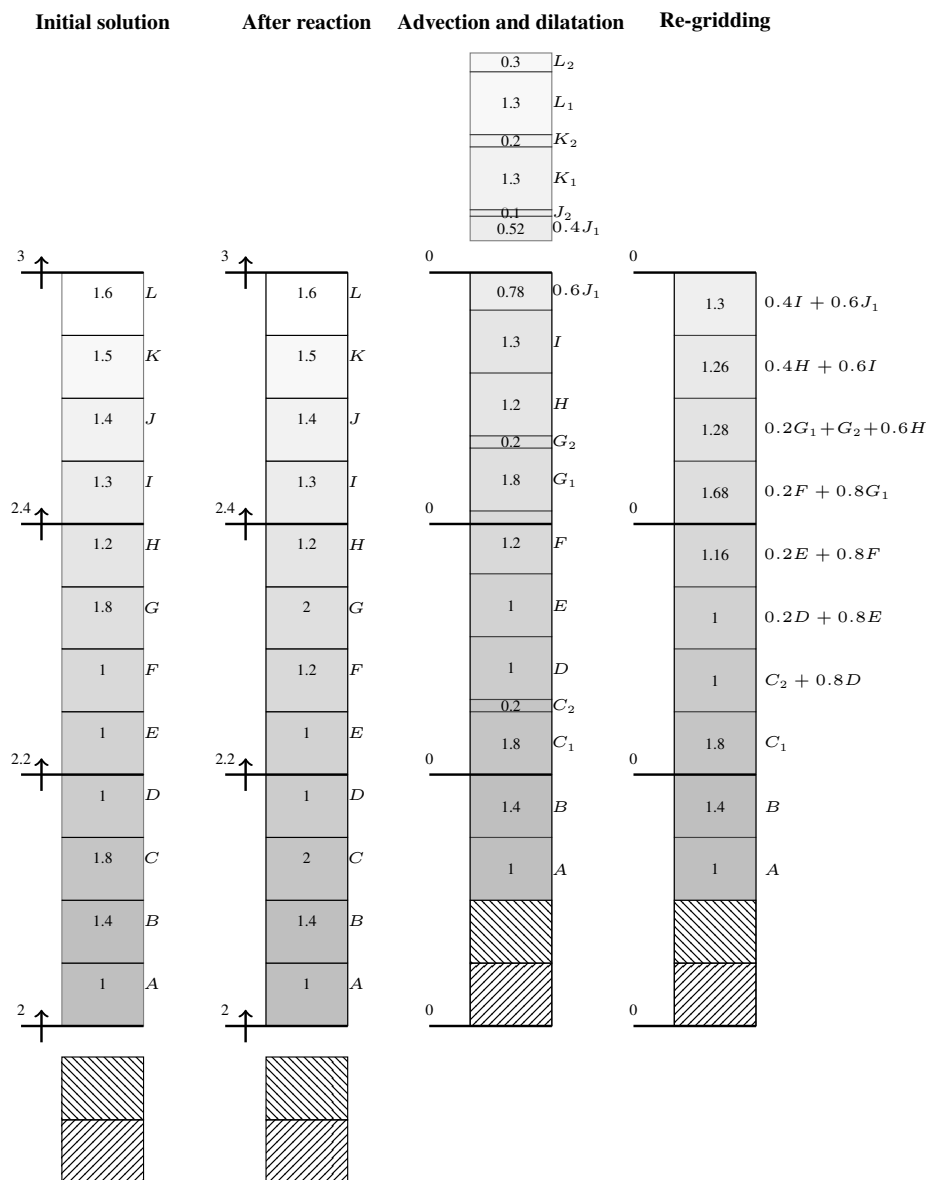
Figure 4.12: Joint dilatation and advection procedure for the "Thermodynamical and geometrical volume approach".

An example of the thermodynamical and geometrical volume approach is given

in Figure 4.12. For the initial solution of the left-most column, we observe that thermodynamical volume is already accumulated within some of the wafers from previous iterations. The LEM processes (diffusion and reaction) leads to the suppression of even more volume increase. The advection and dilatation is then conducted simultaneous. In the first 3DCV there are 2 wafers to be advected in and 2.2. should be advected out. Then 0.2 wafers need to be realized from the thermodynamically banked volume. Since we relax towards $V_w^t/V_w^g = 1$, wafer C is selected, 0.2 wafers is realized and the displacements are conducted. For the second 3DCV we also need to realize 0.2 wafers, and here wafer G is selected and 0.2 wafers are realized from the thermodynamical volume. Lastly, for the third 3DCV 0.6 wafers need to be realized. Relaxation towards unity-ratio now requires realizing 0.1, 0.2 and 0.3 wafers from the banked thermodynamical volume of wafers J, K and L, respectively. Re-gridding finalizes the routine by returning remaining wafers to the prescribed geometrical volume, i.e. $V_w^g = \Delta x^3/\text{LEM}_\text{res}$.

The observant reader would at this stage probably have realized that for configurations with non-correctly prescribed flow-fields we might end up in a situation with negative thermodynamical volumes $V_w^t < 0$ in regions where the prescribed flow field expect reactions, while reactions occur elsewhere in LEM3D. In these cases a two-way coupling is necessary and the current approach would not suffice.

### 4.4.2 Minimizing deviations by the method of least squares

A method has been developed and extended to account for variable density configurations for both mass and volumetric fluxes. This is done by minimization of the sum of squared deviations d^2 applying discrete corrections $\Delta_l \in \mathbb{Z}$ on the wafer displacements, given as

$$d^2 = \sum_l^{N_\text{faces}} \left(\Xi_l + V_w \sum_{n=1}^{\Delta_l} \rho_{ln} \right)^2 . \tag{4.15}$$

and subject to the constraint $\sum_l^{N_\text{faces}} \Delta_l = 0$. The constraint is due to the requirement that the corrections should not violate continuity principally given by $\int_S \Delta \cdot n dS = 0$, where $\Delta = \{\Delta_1, \ldots, \Delta_{N_\text{faces}}\}$ is the discrete correction vector.

For constant density flows or approaches based purely on volume-fluxes the expression for Ξ_l reduces to $r_l = \Xi_l/(\overline{\rho})$, where $\overline{\rho}$ denotes the prescribed density at the cell-face l. In this case the sum of deviations squared reduces to the equation used in [108]:

$$d^2 = \sum_l^{N_\text{faces}} (r_l + \Delta_l)^2 . \tag{4.16}$$
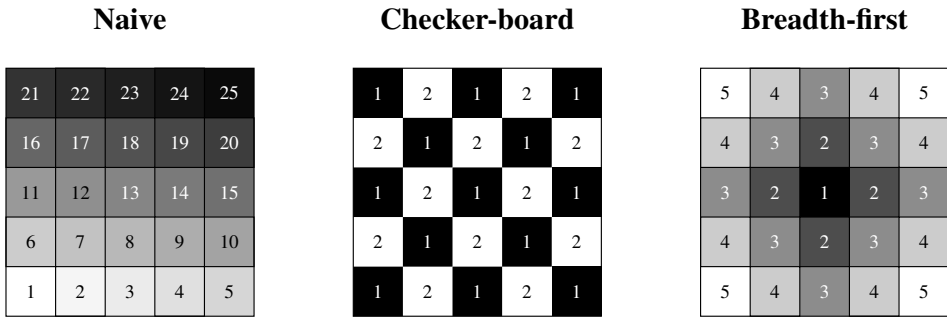
Figure 4.13: Illustration of the alternative displacement algorithms. The checker-board algorithm is illustrated in the middle. The subsets of minimization are alternated between layers and from time step to time step. To the right the iteration process for the breadth-first search based on the center cell as the root is illustrated.

4.4.3 Iteration schemes

Given a framework for how to optimize the displacements of wafers in and out of a single 3DCV independently, we need to decide the order in which the displacements are to be optimized. The displacements are calculated by starting at the upstream inlet layer of 3DCVs (LEMi is always set to be the stream-wise direction). First, the upstream inlet and the lateral displacements are calculated by the selected banking method for the first layer. Second, the displacements are optimized through the least squares method, conserving the number of wafers in each direction. The order of the 3DCVs has proven to be more crucial than first anticipated, as the deviations tend to be accumulated in the stream-wise direction. This results in deviations between the modeled flux and the prescribed fluxes.

In addition to the naive and checker-board algorithms, a bread-first search (BF) algorithm has been implemented and employed. The alternative algorithms are given below:

Naive algorithm

The naive algorithm, starting in either corner and then propagating row-wise upwards, was at an early stage discarded as it would result in accumulation of Ξ_{flux} down-stream in the flow for all variable density applications.

Checker-board

Since neighbouring 3DCVs share a common face, the minimization of Ξ_{flux} is feasible, but also sufficient for constant density approaches, when the 3DCVs belong to one of the two checker-board subsets of the set of all 3DCVs in each layer, as illustrated in the middle sub-figure of Figure 4.13. To ensure a consistent procedure,

the selected checker-board subset is alternated for each successive layer of 3DCVs, and also for successive time-advancement cycles. The checker-board algorithm is the minimization scheme previously used, as presented in [88, 108].

Breadth-first

The breadth-first search (BF) algorithm was originally developed by Zuse [110] and has been applied here to ensure a smooth spatial distribution of the deviations, see Figure 4.14. The breadth-first approach needs to be prescribed one or more roots $\Re$, specified by a location(s) in the jk-plane, i.e. (j_0, k_0). The approach is in LEM3D motivated by, distribution of the deviation Ξ and optimization of the dominating flow regions. It has been seen during simulations that a wise root is the location with the highest concentration of a carefully selected radical species for reactive simulations and the fuel species during non-reacting simulations. For the well known Li-mechanism [48] for hydrogen oxygenation, this has been shown to be H_2O_2 and H_2, i.e.

$$\max_{c \in \{\forall\,3\text{DCV}\}} (Y_{c,\text{H}_2}) \qquad \text{and} \qquad \max_{c \in \{\forall\,3\text{DCV}\}} (Y_{c,\text{H}_2\text{O}_2}),$$

respectively.

The Manhattan Metric is here applied as the measure of distance for the breadth-first algorithm. It is generally defined as $d(x, y) = \sum_{i=1}^{n} |x_i - y_i|$ for $x = (x_1, \ldots, x_n)$ and $y = (y_1, \ldots, y_n) \in \mathbb{R}^n$, but here simplifies to

$$d(j, k) = \min_{\forall r \in \Re} \left(|j - j_{0r}| + |k - k_{0r}| \right),$$

for each of the 3DCV, represented as (j,k,i), in the jk-plane at level i. The right-hand side of Figure 4.13 illustrates the iteration procedure, exemplified by the center cell as the root, i.e. $\Re = \{(0, 0)\}$. As shown in Section 3 of Article II, the simulations are not only sensitive to the choice of minimization algorithm, but also to the choice of the root in the BF procedure.

4.4.4 Auxiliary coupling between LEM domains

The advective operation, described in Subsection 4.4.1, displaces wafers to some extent among the differently oriented LEM domains based on flux preservation. This operation couples the domains. However, the coupling is fairly weak and in order to ensure that physical processes are consistently represented in all spatial directions, an auxiliary coupling of the arrays of mutually orthogonal LEM domains, motivated by the rotational character of turbulent eddies, was found necessary [88, 108]. This has been justified by considering, for instance, a uniform stream-wise flow and homogeneous turbulence. In that case, a scalar injected into
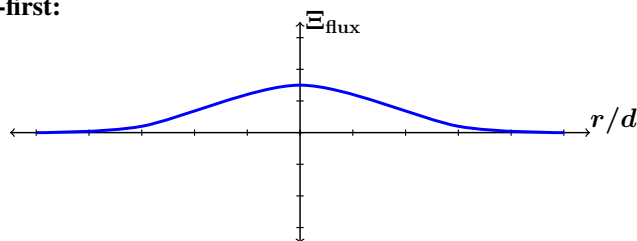
Naive algorithm:
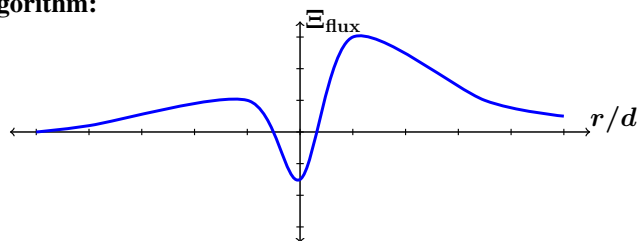
Checker-board:
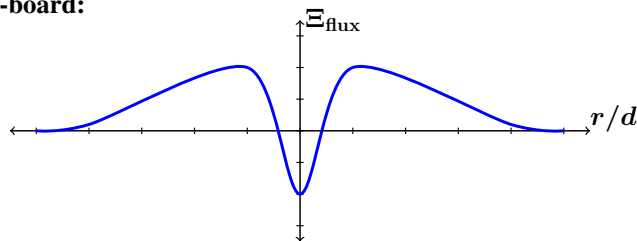
Breadth-first:

Figure 4.14: Typical 3DCV deviations, $\Xi_{\text{flux}} = \sum_{l=1}^{N_{\text{faces}}} \Xi_l$ observed for a reacting single jet configuration for both co-flow assisted and regular jets. The plots does not show actual values but are based on the knowledge built during validation of the code. The shape of the curves would typically be conserved when propagating downstream, but the order of magnitude would increase.

the stream-wise oriented LEM domain will never spread into the laterally oriented domains unless the domains are coupled by an additional process. Hence, the auxiliary coupling is needed to alleviate the possible insufficiency of LEM domain coupling in certain regions of a flow, and thus to assure that the simulation algorithm produces three correlated realizations of the scalar fields. Another example, laminar H_2 and O_2 at high temperature advected through a control volume from perpendicular directions would not mix if the control volume is aligned with the flows. This is particularly important for combustion in which case there would not be any reactions without mixing.

The auxiliary coupling is implemented by stochastic rotations of the 3DCVs. At occurrence, a 3DCV is rotated $\pm 90°$ about any one of the three coordinate axes,
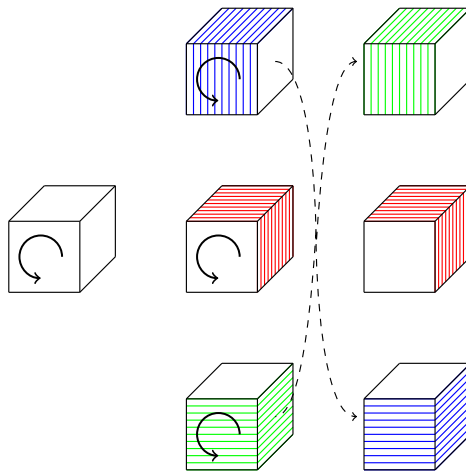
Figure 4.15: Auxiliary coupling between LEM domains illustrated by the rotation from LEMi domains to LEMk domains. As seen the LEMj domain is not affected by this particular rotation.

see Figure 4.15 for illustration. A $\pm 90°$ rotation and three coordinate axes gives six different ways of rotating a 3DCV, all with an equal probability of being performed if a rotation is to occur. The rotations give additional fluid exchanges between the LEM domains, as intended, and strengthens the coupling following from the flux preservation. Rotations occur at the global time steps Δt, with a probability of rotation locally defined through the local CFL number:

$$p_{\text{rot}} = \frac{3}{2} C_{\text{rot}} \text{CFL}_{\text{3DCV}}, \tag{4.17}$$

where CFL_{3DCV} is the local Courant-Friedrichs-Lewy number, and C_{rot} is a model constant. The local CFL number is calculated from $\text{CFL}_{\text{3DCV}} = \text{CFL} \cdot V_{\text{3DCV}}/V_{\text{max}}$ where CFL is the global Courant-Friedrichs-Lewy number, V_{3DCV} is the absolute value of the largest velocity component associated with the 3DCV side faces, and V_{max} is the maximum V_{3DCV} of the computational domain.

The effects of varying C_{rot} are investigated in Section 3 of Article II. Note that p_{rot} might exceed 1 in the above expression for large C_{rot}, but that the restriction $p_{\text{rot}} \leq 1$ is implemented in the code. The greatest value of p_{rot} is always for the particular 3DCV(s) for which $V_{\text{3DCV}} = V_{\text{max}}$. Here the rotation probability is $p_{\text{rot}} = \frac{3}{2}\text{CFL}$. The origin of the factor $\frac{3}{2}$ stems from the idea that each wafer should change LEM domain within each 3DCV. Hence, since only $\frac{2}{3}$ of the LEM wafers in a 3DCV are affected by a rotation while the remaining $\frac{1}{3}$ are unaffected, the frequency is multiplied by the factor $\frac{3}{2}$ in order to ensure that each of the LEM wafers within a given 3DCV will be displaced to differently oriented domains during the advective

residence time. The factor normally implies that the implementation allows for a maximum CFL number given by CFL $\leq \frac{2}{3}$. As $p_{rot} \leq 1$ is implemented, this is however not a strict restriction.

One feature of the auxiliary coupling is that the 3DCV rotations introduce additional transport of the wafers. Even as this transport can be physically motivated in the model, it is not a result of a physical process, but rather a necessity. The extra transport can however be evaluated and counterbalanced by deducting the corresponding diffusivity D_T^{rot} from the turbulent diffusivity D_T, such that the remaining triplet map diffusivity D_T^{TM} is given by

$$D_T^{TM} = D_T - D_T^{\text{rot}}. \tag{4.18}$$

Lemma 4.

$$D_{\text{T}}^{\text{rot}} = C_{\text{rot}} \frac{3}{4} \frac{V_{\text{3DCV}}}{\Delta x} \left\langle \delta^2 \right\rangle. \tag{4.19}$$

Here, $\left\langle \delta^2 \right\rangle$ is the mean square single rotation displacement of the wafers in the 3DCV in a given direction orthogonal to the rotational axis.

Proof. We find D_T^{rot}, for a single 3DCV, in the same manner as the diffusion induced by triplet maps, i.e. by Equation (2.8) and by using that the rate of 3DCV rotations is $N = C_{\text{rot}} \frac{3 V_{\text{3DCV}}}{2 \Delta x}$, i.e. $3/2$ times the flow through time. The result follows. $\qquad\square$

Lemma 5. The mean square displacement due to a single rotation can be expressed as

$$\left\langle \delta^2 \right\rangle = \frac{2}{3} \sum_{k=1}^{\text{LEM}_{\text{res}}/2} \frac{\left(\frac{(2k-1)}{2} \frac{\Delta x}{\text{LEM}_{\text{res}}} \right)^2}{\text{LEM}_{\text{res}}/2} \tag{4.20}$$

Proof. Only $\frac{2}{3}$ of the wafers are displaced for each rotation, following from the fact that only two of three directions are affected, e.g., as seen in Figure 4.15. Further, as δ is symmetric about the displacement-axis, i.e. there is displacement symmetry within each 3DCV around the center point, and as $\text{LEM}_{\text{res}} \in 2\mathbb{Z}$ we get the following relation

$$\left\langle \delta^2 \right\rangle = \frac{\sum_{k=1}^{\text{LEM}_{\text{res}}} \delta^2(k)}{\text{LEM}_{\text{res}}} = \frac{2 \sum_{k=1}^{\text{LEM}_{\text{res}}/2} \delta^2(k)}{\text{LEM}_{\text{res}}} = \sum_{k=1}^{\text{LEM}_{\text{res}}/2} \frac{\delta^2(k)}{\text{LEM}_{\text{res}}/2}. \tag{4.21}$$

Hence what remains is to find the displacement for a given wafer at position $k \in [1, \text{LEM}_{\text{res}}/2]$, where $k = 1$ is the closest one to the center-point while
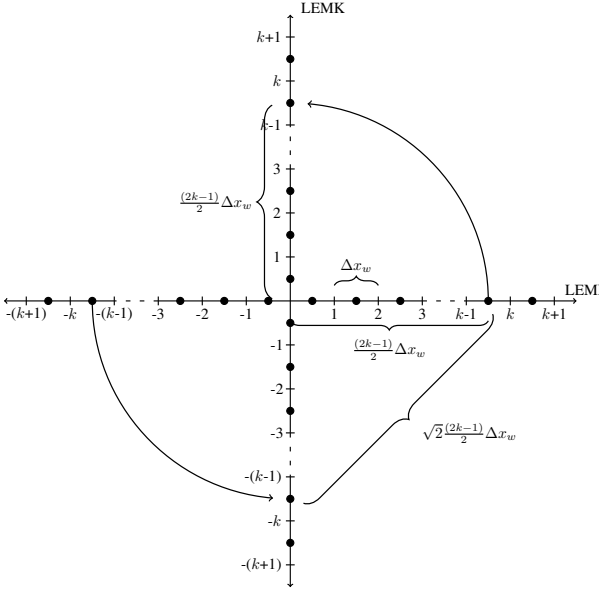
Figure 4.16: Illustration of the displacement distance for wafers between direction I and K for the wafers at position $\pm k$. It is seen that δ is symmetric about the displacement-axis, that is $\delta(-k) = \delta(k)$.

$k = \mathrm{LEM_{res}}/2$ is the wafer located at the boundary. As in previous work [88, 108], we neglect the diffusion induced by rotation-displacement in other directions than the one the wafer originates from before rotation. If the two dimensional displacement would have been considered we would have added a factor of $\sqrt{2}$, given from Pythagoras, as is illustrated in fig 4.16. Neglecting this factor conserves the segregation between the three directions and can be justified by the interest in the order of magnitude and that the factor of $\sqrt{2}$ can be included in the variable C_{rot}.

Now, from Figure 4.16, the displacement is given by

$$\delta^2(k) = \frac{(2k-1)}{2}\Delta x_w = \frac{(2k-1)}{2}\frac{\Delta x}{\mathrm{LEM_{res}}} \tag{4.22}$$

$\square$

The expression follows:

$$D_T^{TM} = D_T - C_{\mathrm{rot}}\frac{3}{4}\frac{V_{\mathrm{3DCV}}}{\Delta x}\left\langle \delta^2 \right\rangle. \tag{4.23}$$

The above method is the only way to account for the induced diffusivity as LEM3D

has no perception of flux within each of the 3DCVs. The effect of the above expression is that a fraction of the turbulent transport implemented by the triplet maps is replaced by the 3DCV rotations. In the outer regions of the flow domain, D_T^{TM} may turn negative and is set to zero, with the implication that the rotation-induced transport exceeds the physically specified transport that it replaces (a model artifact). It should be noted, however, that the effect of the excess transport is negligible in most applications and can be accounted for by lowering the rotational frequency through C_{rot}. Another coupling artifact of the model is that the 3DCV rotations bring dissimilar fluid states into contact. A remedy to this issue is to use coarser 3DCVs to minimize the artifacts. Such an approach also has the benefit of being computationally less expensive than using smaller 3DCVs for given spatial resolution of the LEM wafers since the total number of wafers in the simulation is reduced. However, the computational cost saving of using larger 3DCVs must be balanced by the model performance of LEM3D simulations, as other model artifacts are likely to become strong if the 3DCVs are too large. In particular, the coarse-scale 3D-resolution must under all circumstance be fine enough so that mean-flow resolution requirements are fulfilled.

4.5   Model input and initialization

As the LEM3D model is a pure mixing model it requires mean-flow information such as the mean mass-flux $\overline{\rho \boldsymbol{u}}$, the turbulent diffusivity D_T, integral length scale L and Kolmogorov scale η, either from a flow solver or experiment. Since the mass-flux and the turbulent diffusivity typically vary in the spatial directions, it needs be resolved at the coarser length scale corresponding to the 3DCVs. The values of D_T, L and η are fed to the centers of the control volumes, while face-normal components of $\overline{\rho \boldsymbol{u}}$ are provided to the 3DCV faces. Consequently, each 3DCV has associated its own set of turbulence parameter $\{D_T, L, \eta\}$ and PDFs $\{f_l, f_t, f_s\}$.

Boundary conditions $\overline{\rho \boldsymbol{u}}$ on the outer 3DCV faces and scalars including temperature and density, are either set according to physical properties or prescribed from experiments or CFD.

The currently used hybrid model is based on an initial RANS solution which generates the necessary model input to LEM3D according to Eq. (3.4)-(3.6). Moreover, LEM3D is normally initialized on 3DCV level using results from preceding RANS simulations in order to enhance convergence. The effect of different initialization procedures from a simple freely propagating flame has been investigated in Article III.

Further, five parameters need to be specified in advance of the simulation.

First, the scaling exponent p used in the linear eddy model framework is based on the scaling relation of the turbulent viscosity $\nu_T(l) \propto l^p$, as induced by turbulent eddies of size l or smaller. The scaling exponent is according to the mathematical derivation in Chapter 2 set to $p = 4/3$. It is derived on the basis of Richardson's 1926 scaling law $\nu_T(l) \propto 0.6 l^{4/3}$ [82], and similarly $\nu_T(\kappa)$ from Kolmogorov's hypothesis based on the inertial range scaling relating the turbulent viscosity to the wave number $\kappa = 2\pi/l$, through $E(\kappa) = C_K \varepsilon^{2/3} \kappa^{-5/3}$ [43, 100].

Second, the under-resolving factor fac sets a global lower limit for the LEM-resolution through

$$\Delta x_w = \min_{\{\forall\,3\text{DCV}\}} (\eta, \eta_B) \cdot \text{fac}.$$

Third, Δx is specified, currently similar to the RANS-resolution Δx_{RANS}. This again implies that the number of wafers within each of the 3DCVs coordinate directions are $\text{LEM}_{\text{res}} = \lceil \Delta x / \Delta x_w \rceil$.

Fourth, a CFL number needs to be given, typically in the range $[0.001, 0.3]$. The advectional time advancement is then globally calculated based on the prescribed CFL number through $\Delta t = \text{CFL}\,\Delta x / \max_{\{\forall\,3DCV\}} (|\boldsymbol{u}|)$.

Fifth, C_{rot} needs to be prescribed giving the frequency of the rotations in the auxiliary coupling. C_{rot} is typically set equal to one, a value which was confirmed suitable in Article II.

4.6 LEM3D options

This Chapter has described, in detail, all the technical aspects of the model stating the alternatives and different paths that might be used in the code. Figure 4.17 summarizes the options within the current LEM3D framework and their intended combinations. The red, black and blue arrows give the approaches followed during the current work, the alternatives available in the code, not extensively used and the options to be implemented, respectively. In addition there are the varieties in the variables described in the past chapters, e.g., C_{rot}, fac, CFL and p.

4.6.1 Computational speed up by MPI

The in-house code has been parallelized using OpenMPI in Fortran 90. The speed-up will depend on a case-to-case basis, in particular depending on LEM_{res} and the number of LEM-domains. The speedup is, however, always limited by the serial part of the program, which for LEM3D consists of initialization, advection (wafer displacements and auxiliary coupling) and finalization. Let us denote the fraction of the program which require serial operations by f.
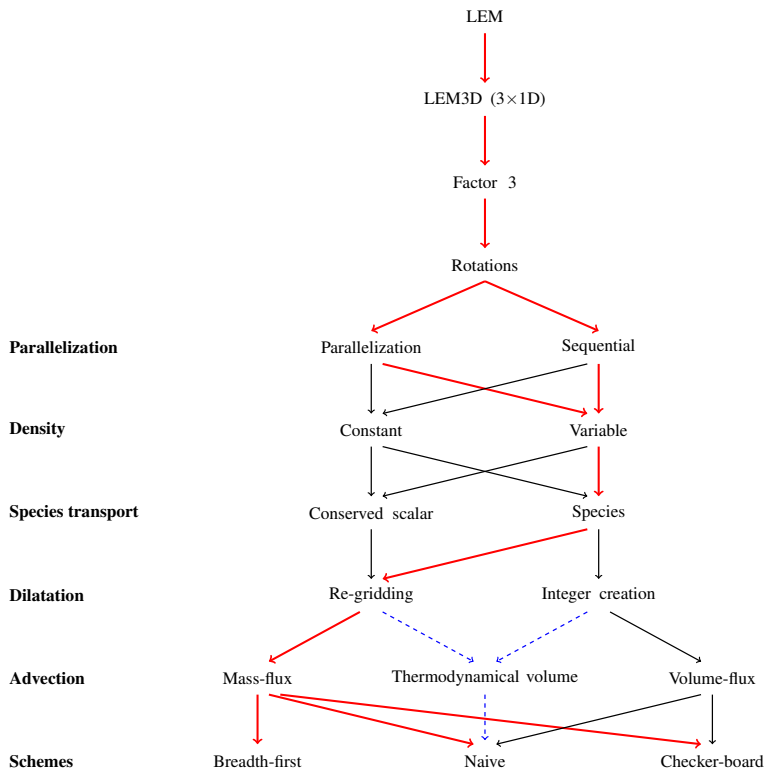
Figure 4.17: Diagram giving the different options in the LEM3D framework. The red thick line illustrate the approaches following during the current work. Black lines indicate the alternatives available in the code, not extensively used. While the blue dashed lines indicate options currently not implemented in the code.

If we have at most p_s processors, then the parallelization of the sequential algorithm has a complexity of at least $f + (1 - f)/p_s$ times the complexity of the sequential LEM3D. Thus, for any input to LEM3D, the parallelized algorithm achieves a speedup of at most $1/[f + (1 - f)/p_s]$ over the sequential algorithm. This upper bound on the speedup S achieved for any input by parallelizing a sequential algorithm is known as Amdahl's law [2]:

$$S \leq \frac{1}{f + (1 - f)/p_s}. \tag{4.24}$$

The speedup has been tested for some test-cases indicating that the fraction f lies in the range $[0.025, 0.05]$. However, as the sequential portion decreases with LEM_{res} and the number of LEM-domains, it is reasonable to assume that f will shift towards 1 when the the number of cells increases.

5. Result and discussion

This Chapter provides a summary of the selected articles, which contain the achieved results and benchmarks. The main outcomes and contributions are reported and discussed for each article, in a dedicated sub-section. For a more complete overview, the articles are enclosed at the end of the thesis. The order in which the articles are presented follows the progression of the thesis work. Alongside the description of the contents, the motivations that led to deal with the specific analysis are outlined.

5.1 Article I - Three-dimensional Linear Eddy Modeling of a Turbulent Lifted Hydrogen Jet Flame in a Vitiated Co-flow

After the model framework got extended from previous work [108] to include parallel computing, finite-rate chemistry, mass-fluxes and re-gridding and succeeding initial tests, verifications and simple validation cases, it was natural to select a challenging configuration for demonstration of the model. Berkeley's vitiated co-flow burner, consisting of a lifted turbulent N_2-diluted hydrogen jet flame in a vitiated co-flow of hot products from lean H_2/air combustion was selected. This configuration was of particular interest as it includes various aspects, such as auto-ignition, flame-propagation and flame stabilization. The novel LEM3D methodology for modeling and simulation of reactive flows was used as a post-processing tool for an initial RANS simulation. As the RANS simulations showed strong hysteresis effects; a converged RANS simulation with an attached flame was selected to provide mean-flow statistics to LEM3D. This approach, where LEM3D is complementing RANS with unsteadiness and small-scale resolution, is computationally efficient in comparison to resolving the small-scales with traditional CFD. Flame lift-off heights and flame structure were investigated, along with other characteristics not available from RANS alone, such as the instantaneous and detailed species profiles and small-scale mixing.

5.2 Article II - A parametric study of LEM3D based on validation with a Turbulent Lifted Hydrogen Jet Flame in a Vitiated Co-flow

In continuation of the work reported in Article I, the hybrid RANS-LEM3D model was prescribed a flow field from RANS with a lifted flame matching the experimental data by Cabra et al.. Analyzing the results showed significant deviations between LEM3D and prescribed mass-fluxes, i.e. large Ξ_{flux}, where Ξ_{flux} is the quantitative value of the deviations. The simulations resulted in radial deviations following the checker-board profile in Figure (4.14), stemming from the iteration scheme at use. In order to reduce the overall deviation, i.e. remove the existence of locally large fluxes $|\Xi_{\text{flux}}|$, the breadth-first routine was introduced. This resulted in a smoother radial profile of Ξ_{flux} similar to the one seen for breadth-first in Figure (4.14), without local extremes in $|\Xi_{\text{flux}}|$. The dependence of lift-off heights and flame structure on iteration schemes and model parameters were investigated in detail, along with other characteristics not available from RANS alone, such as the instantaneous and detailed species profiles, scatter plots and small-scale mixing. This kind of information is of great importance when practical implications are taken into consideration. It was found that LEM3D for the current application is able to show additional details compared to the RANS simulation with low computational cost, in comparison to traditional DNS simulations.

Even though LEM3D showed good agreement with experiments in the far field, currently the algorithm does not yield a lift-off height in accordance with the experiments. Thorough investigations of this feature was conducted, which showed that the auxiliary coupling is causing an increased spread of H_2, most easily observed in the non-reactive case. Combined with low fluxes in the LEM domains surrounding the central jet nozzle, and the treatment in LEM3D of three dimensions as $3 \times 1D$, the conditions and residence times are sufficient for reactions, stabilizing the flame at a low lift-off. However, as near-field discrepancy was a previously known model artifact of LEM resulting from the instantaneous nature of the eddy events [35], and among other things the undeveloped energy spectrum, the near field discrepancy was accepted as a model artifact.

5.3 Article III - Dimensional Decomposition of Turbulent Reacting flows.

Following up on the near-field discrepancy observed in Article II, the dimensional-decomposition approach, decomposing 3D into $3 \times 1D$ for turbulent (reacting) flows was discussed and investigated in detail. In particular, the currently used re-couplings for the dimensional-decomposition approach, wafer displacements and

the auxiliary coupling, was challenged and enlightened. First, a simple test case using a freely propagating laminar premixed flame was simulated, investigating the flame front using different initializations and switching the auxiliary coupling off. The freely propagating laminar premixed flame investigations concluded that the flame stabilizes at the upstream face of the initial solution when both the advectional and auxiliary re-couplings are activated; and in the center of the control volume when the auxiliary coupling is not at use. Second, the results from the LEM3D simulations of Berkeley's vitiated co-flow burner was re-visited adding a more detailed discussion of the model artifacts stemming from the dimensional-decomposition approach in combination with the auxiliary coupling. The main conclusion of the present work is that the auxiliary coupling introduces an unacceptable amount of artificial diffusion. Last, a suggestion on improvement of the models relying on the dimensional-decomposition approach is given. It is based on the Péclet number, and suggests to match the total diffusive mass-flux, potentially, prescribed from RANS or experiments.

6. Conclusion and further work

The LEM3D modeling approach for turbulent reactive flows has been motivated, discussed and investigated in detail. This new methodology, relying on the dimensional-decomposition approach, decomposing 3D into 3×1D, has been extended with respect to the the previous work by Sannan et al. [87, 88] and Weydahl et al. [108, 109]. The extensions consist of finite rate chemistry, parallel computing, re-gridding, mass-fluxes, wafer-tracking, the breadth-first iteration scheme, minimization of deviations by least squares, and post-processing tools.

Three different iteration procedures, a breadth-first search, a checker-board algorithm and a naive approach, as well as parameters of the model framework are examined and tested for sensitivity towards the result.

LEM3D is currently implemented as a post-processing tool for an initial RANS simulation or experimental data. In this hybrid approach, LEM3D complements RANS/experiments with unsteadiness and small-scale resolution in a computationally efficient manner, with respect to fully resolved resolution in all three spatial directions. In the present modeling approach, mean-flow information from RANS/experiment provides model input to LEM3D, which returns the scalar statistics needed for more accurate mixing and reaction calculations.

To demonstrate the RANS-LEM3D model, the hybrid model is applied to various configurations with varying degrees of success. A thorough investigation based on the flame front in a freely propagating laminar premixed flame for the approach is conducted, concluding that the flame stabilizes at the upstream face of the initial solution when both the advectional and auxiliary re-couplings are activated; and in the center of the control volume when the auxiliary coupling is not at use. Even as this result is not groundbreaking, it strongly increases the understanding of coupling mechanism in the dimensional-decomposition approach and their effects.

LEM3D has simulated both a lifted and attached turbulent N_2-diluted hydrogen jet flame in a vitiated co-flow of hot products from lean H_2/air combustion. The

dependence of lift-off heights and flame structure on iteration schemes and model parameters are investigated in detail, along with other characteristics not available from RANS alone, such as the instantaneous and fully resolved species profiles, temporal resolved scatter plots and small scale mixing. Furthermore, results from LEM3D simulations of Berkeley's vitiated co-flow burner are thoroughly examined adding a detailed discussion of the model artifacts. It is found that LEM3D is able to show additional details compared to the RANS simulation with low computational cost, in comparison to traditional DNS simulations. A drawback for the additional detail is that the results deviate from the average-profiles prescribed. The artifacts of the model is strongly linked to the dimensional-decomposition approach and the need of a re-coupling within the dimensional-decomposition approach. Thereby, the re-coupling mechanisms at use are thoroughly investigated.

The main finding of the present work is that the auxiliary coupling, currently at use in the model, introduces an unacceptable amount of artificial diffusion. And hence the conclusion is similar to the concern raised in previous work [108]: *(...) it is too early to conclude whether if the auxiliary coupling strategy provides a sufficiently adequate representation of the physical process.* A suggested improvement is given in Article III. It is based on bounding the overall diffusion flux through matching the Péclet number locally. This however, requires the Pe number to be prescribed together with other flow characteristics either from experiments or CFD.

In retrospect, multiple investigations should have been conducted on simpler configurations than the vitiated co-flow burner, which seized a large portion of the time spent on research during this work, due to the unsatisfactory results of the simulations. However, at the time it was natural to go more or less directly to the vitiated co-flow burner as LEM3D was expected to yield reasonable results based on past work [88, 108].

Although relevant comparisons to experimental data have been presented, DNS will accommodate the ultimate standard for verification for LEM3D. Enabling comparison of higher statistical moments, multi-point statistics and scalar spectra, which will provide a valuable validation of LEM3D. Comparison on the same basis, facilitated trough corresponding boundary conditions, assigning equal properties to both DNS and LEM3D, and supplying LEM3D with the mean flow advection and the turbulent diffusivity estimated from DNS. Therefore, as a part of the founding application, it was intended to simulate the jet in cross-flow configuration by Grout et al. [23]. DNS results from Kolla et al. [42] was provided by Prof. Gruber, to facilitate such a validation. The simulation was prepared through coarsening of the DNS results and some preliminary simulations was conducted. The results, however, yielded that the bidirectional flow configuration was as challenging as

expected. Further, issues was reviled related to having a preferred/iterative direction in the wafer displacement algorithm of LEM3D while having two dominant directions in the flow, dependent on location, for the jet in cross-flow configuration. The results from the preliminary simulations showed that more efforts should be investigated into this problem and other problems with bidirectional nature once the current issues, enlightened in Article III, are resolved.

An original intended path-way for this work was to implement and investigate the two-way coupling between LEM3D and a flow solver (ref. Sub-section 3.3.8). However, as there were many aspects to be investigate within the current framework, i.e. LEM3D as a post-processing tool for either CFD or experiments, it was found satisfactory within the scope of this work to investigate the one-way coupling. Examination of results in LEM3D are already remarkably intricate as many different processes occurs and a the two-way coupling would obscure the understanding of the results further. There would, however, be natural to proceed to a two-way coupled framework once the current issues, as enlightened in Article III, are resolved.

In short, the current study has, on behalf of the HYCAP project, contributed to in-depth knowledge on an advanced numerical design tool with relevance to the development of hydrogen-fired combustors and with relevance for the combustion community to develop generally valid combustion models. The two main missing ingredients of the LEM3D code at the start-up of the study, namely a detailed chemistry mechanism for hydrogen and parallelization for computations on large clusters, has been successfully implemented. The LEM3D tool is very complex and contains all important aspects of the complex interactions between turbulent flows and chemical reactions. At the same time the formulation is unique and differs from state-of-the-art tools in its approach. However, at its current state with the enlightened artifacts of the auxiliary coupling, the model is not found satisfactorily refined to the level required in order to be integrated into commercial state-of-the-art CFD simulation codes. Nevertheless, the LEM3D code in its current state represents a valuable test ground and learning tool for future graduate students researchers alike.

Bibliography

[1] Oxford Dictionaries - Model. https://en.oxforddictionaries.com/definition/model. Accessed: 12.08.2018.

[2] K. A. Berman and J. L. Paul. *Algorithms: sequential, parallel, and distributed*. Thomson/Course Technology Boston, MA, 2005.

[3] R. Bilger. Conditional moment closure for turbulent reacting flow. *Physics of Fluids A: Fluid Dynamics*, 5(2):436–444, 1993.

[4] K. Bischoff. Mixing and contacting in chemical reactors. *Industrial & Engineering Chemistry*, 58(11):18–32, 1966.

[5] P. Bradshaw. *An Introduction to Turbulence and Its Measurement*. Pergamon Press, 1971.

[6] K. Bray and J. B. Moss. A unified statistical model of the premixed turbulent flame. *Acta Astronautica*, 4(3-4):291–319, 1977.

[7] W. H. Calhoon. *On Subgrid Combustion Modeling for Large Eddy Simulations*. PhD thesis, Georgia Institute of Technology, 1996.

[8] S. Cao and T. Echekki. A low-dimensional stochastic closure model for combustion large-eddy simulation. *Journal of Turbulence*, 9(2):1–35, 2008.

[9] J.-Y. Chen. A Eulerian PDF scheme for LES of nonpremixed turbulent combustion with second-order accurate mixture fraction. *Combustion Theory and Modelling*, 11(5):675–695, 2007.

[10] J.-Y. Chen. Lecture notes ME257 - advanced combustion. UC Berkeley Department of Mechanical Engineering, October 2016.

[11] S. Chu and A. Majumdar. Opportunities and challenges for a sustainable energy future. *Nature*, 488(7411):294–303, 2012.

[12] R. L. Curl. Dispersed phase mixing: I. Theory and effects in simple reactors. *AIChE Journal*, 9(2):175–181, 1963.

[13] M. S. Day and J. B. Bell. Numerical simulation of laminar reacting flows with complex chemistry. *Combustion Theory and Modelling*, 4(4):535–556, 2000.

[14] P. Domingo and L. Vervisch. Triple flames and partially premixed combustion in autoignition of non-premixed turbulent mixtures. *Symposium (International) on Combustion*, 26(1):233–240, 1996.

[15] T. Echekki and E. Mastorakos. *Turbulent combustion modeling: Advances, new trends and perspectives*. Springer Science & Business Media, 2010.

[16] T. Echekki, A. R. Kerstein, T. D. Dreeben, and J.-Y. Chen. 'One-Dimensional Turbulence' Simulation of Turbulent Jet Diffusion Flames: Model Formulation and Illustrative Applications. *Combustion and Flame*, 125(3):1083–1105, 2001.

[17] I. S. Ertesvåg. *Turbulent strøyming og forbrenning: frå turbulensteori til ingeniørverktøy*. Tapir Akademisk Forlag, 2000.

[18] R. O. Fox and A. Varma. *Computational Models for Turbulent Reacting Flows*. Cambridge Univ. Press, 2003.

[19] S. Frankel, P. McMurtry, and P. Givi. Linear eddy modeling of reactant conversion and selectivity in turbulent flows. *AIChE Journal*, 41(2):258–266, 1995.

[20] J. Gibbins and H. Chalmers. Carbon capture and storage. *Energy Policy*, 36 (12):4317–4322, 2008.

[21] E. D. Gonzalez-Juez, R. C. Schmidt, and A. R. Kerstein. ODTLES simulations of wall-bounded flows. *Physics of Fluids*, 23(12):125102–125102–13, 2011.

[22] I. R. Gran. *Mathematical modeling and numerical simulation of chemical kinetics in turbulent combustion*. PhD thesis, Norges Tekniske Høgskole, 1994.

[23] R. Grout, A. Gruber, C. S. Yoo, and J. Chen. Direct numerical simulation of flame stabilization downstream of a transverse fuel jet in cross-flow. *Proceedings of the Combustion Institute*, 33(1):1629–1637, 2011.

[24] F. Grøvdal, S. Sannan, J.-Y. Chen, A. R. Kerstein, and T. Løvås. (in press), Three-dimensional Linear Eddy Modeling of a Turbulent Lifted Hydrogen Jet Flame in a Vitiated Co-flow. *Flow, Turbulence and Combustion,* DOI: 10.1007/s10494-018-9963-x, 2018.

[25] F. Grøvdal, S. Sannan, J.-Y. Chen, and T. Løvås. A parametric study of LEM3D based on validation with a Turbulent Lifted Hydrogen Jet Flame in a Vitiated Co-flow. *Submitted to Combustion Science and Technology* 4th July, 2018.

[26] J. O. Hinze. *Turbulence 2nd ed.* McGraw-Hill, New York, 1975.

[27] J. Hirschfelder, R. B. Bird, and C. F. Curtiss. *Molecular theory of gases and liquids*. Wiley, New York, 1964.

[28] Intergovernmental Panel on Climate Change. *Climate Change 2007- Mitigation of Climate Change: Working Group III Contribution to the Fourth Assessment Report of the IPCC*. Cambridge University Press, 2007.

[29] International Energy Agency. Carbon Capture and Storage Roadmap. https://www.iea.org/publications/freepublications/publication, 2010. Accessed: 17.10.2018.

[30] W. Jones and B. E. Launder. The prediction of laminarization with a two-equation model of turbulence. *International Journal of Heat and Mass Transfer*, 15(2):301–314, 1972.

[31] M. Kanniche, R. Gros-Bonnivard, P. Jaud, J. Valle-Marcos, J.-M. Amann, and C. Bouallou. Pre-combustion, post-combustion and oxy-combustion in thermal power plant for CO_2 capture. *Applied Thermal Engineering*, 30(1): 53–62, 2010.

[32] R. J. Kee, M. E. Coltrin, and P. Glarborg. *Chemically reacting flow: theory and practice*. John Wiley & Sons, 2005.

[33] A. R. Kerstein. A linear-eddy model of turbulent scalar transport and mixing. *Combustion Science and Technology*, 60(4-6):391–421, 1988.

[34] A. R. Kerstein. Linear-eddy modelling of turbulent transport. Part 6. Microstructure of diffusive scalar mixing fields. *Journal of Fluid Mechanics*, 231:361–394, 1991.

[35] A. R. Kerstein. Linear-eddy modelling of turbulent transport. Part 7. Finite-rate chemistry and multi-stream mixing. *Journal of Fluid Mechanics*, 240: 289–313, 1992.

[36] A. R. Kerstein. One-dimensional turbulence: model formulation and application to homogeneous turbulence, shear flows, and buoyant stratified flows. *Journal of Fluid Mechanics*, 392:277–334, 1999.

[37] A. R. Kerstein. One-dimensional turbulence: A new approach to high-fidelity subgrid closure of turbulent flow simulations. *Computer Physics Communications*, 148(1):1–16, 2002.

[38] A. R. Kerstein. One-dimensional turbulence stochastic simulations of multi-scale dynamics. *Lecture Notes in Physics, Interdisciplinary Aspects of Turbulence*, 756(1-6):291–333, 2009.

[39] A. R. Kerstein, S. Sannan, and F. Grøvdal. Colloquium. May 2018. Livermore, CA, USA.

[40] A. R. Kerstein, W. T. Ashurst, S. Wunsch, and V. Nilsen. One-dimensional turbulence: vector formulation and application to free shear flows. *Journal of Fluid Mechanics*, 447:85–109, 2001.

[41] A. Y. Klimenko and R. W. Bilger. Conditional moment closure for turbulent combustion. *Progress in Energy and Combustion Science*, 25(6):595–687, 1999.

[42] H. Kolla, R. W. Grout, A. Gruber, and J. H. Chen. Mechanisms of flame stabilization and blowout in a reacting turbulent hydrogen jet in cross-flow. *Combustion and Flame*, 159(8):2755–2766, 2012.

[43] A. N. Kolmogorov. The local structure of turbulence in incompressible viscous fluid for very large Reynolds numbers. *Dokl. Akad. Nauk SSSR*, 30 (4):299–303, 1941.

[44] K. K. Kuo and R. Acharya. *Fundamentals of turbulent and multiphase combustion*. John Wiley & Sons, 2012.

[45] T. Lackmann. *A Representative Interactive Linear-eddy-model (RILEM) for Simulating Spray Combustion*. PhD thesis, Chalmers University of Technology, 2017.

[46] T. Lackmann, A. R. Kerstein, and M. Oevermann. A representative linear eddy model for simulating spray combustion in engines (RILEM). *Combustion and Flame*, 193:1–15, 2018.

[47] B. E. Launder and D. B. Spalding. The numerical computation of turbulent flows. *Computer Methods in Applied Mechanics and Engineering*, 3(2): 269–289, 1974.

[48] J. Li, Z. Zhao, A. Kazakov, and F. L. Dryer. An updated comprehensive kinetic model of hydrogen combustion. *International Journal of Chemical Kinetics*, 36(10):566–575, 2004.

[49] B. F. Magnussen. On the structure of turbulence and a generalized eddy dissipation concept for chemical reaction in turbulent flow. *19th Aerospace Sciences Meeting*, 1981.

[50] B. F. Magnussen. Modeling of NO_x and soot formation by the eddy dissipation concept. *International Flame Research Foundation First Topic Oriented Technical Meeting*, pages 17–19, 1989.

[51] B. F. Magnussen. Modeling of pollutant formation in gas turbine combustors based on the eddy dissipation concept. *18ᵗʰ International Congress on Combustion Engines, Tianjin, China, June*, pages 5–9, 1989.

[52] B. F. Magnussen and B. H. Hjertager. On mathematical modeling of turbulent combustion with special emphasis on soot formation and combustion. *Symposium (international) on Combustion*, 16(1):719–729, 1977.

[53] F. E. Marble and J. E. Broadwell. The coherent flame model for turbulent chemical reactions. Technical report, Project Squid Headquarters, Purdue University, Lafayette, 1977.

[54] F. Mathey and J. P. Chollet. Subgrid-scale model of scalar mixing for large eddy simulations of turbulent flows. In *Direct and Large-Eddy Simulation II*, pages 103–114. Springer, 1997.

[55] R. J. McDermott. *Toward one-dimensional turbulence subgrid closure for large-eddy simulation*. PhD thesis, Department of Chemical Engineering, University of Utah, 2005.

[56] P. A. McMurthy, S. Menon, and A. R. Kerstein. A linear eddy sub-grid model for turbulent reacting flows: Application to hydrogen-AIR combustion. *Symposium (International) on Combustion*, 24(1):271–278, 1992.

[57] P. A. McMurtry, T. C. Gansauge, A. R. Kerstein, and S. K. Krueger. Linear eddy simulations of mixing in a homogeneous turbulent flow. *Physics of Fluids A: Fluid Dynamics*, 5(4):1023–1034, 1993.

[58] P. A. McMurtry, S. Menon, and A. Kerstein. Linear eddy modeling of turbulent combustion. *Energy & Fuels*, 7(6):817–826, 1993.

[59] S. Menon and W. H. Calhoon Jr. Subgrid mixing and molecular transport modeling in a reacting shear layer. *Symposium (International) on Combustion*, 26(1):59–66, 1996.

[60] S. Menon and A. R. Kerstein. Stochastic simulation of the structure and propagation rate of turbulent premixed flames. *Symposium (International) on Combustion*, 24(1):443–450, 1992.

[61] S. Menon and A. R. Kerstein. The Linear-Eddy Model. In *Turbulent Combustion Modeling*, pages 221–247. Springer, 2011.

[62] S. Menon, P. McMurtry, and A. Kerstein. A linear-eddy mixing model for large eddy simulation of turbulent combustion. In *Large Eddy Simulation of*

Complex Engineering and Geophysical Flows, pages 287–314. Cambridge University Press, New York, 1993.

[63] S. Menon, P. A. McMurtry, A. R. Kerstein, and J.-Y. Chen. Prediction of NO_x production in a turbulent hydrogen-air jet flame. *Journal of Propulsion and Power*, 10(2):161–168, 1994.

[64] F. R. Menter. Best Practice: Scale-Resolving Simulations in ANSYS CFD. *ANSYS Germany GmbH*, pages 1–70, 2012.

[65] F. R. Menter. Stress-Blended Eddy Simulation (SBES)—A New Paradigm in Hybrid RANS-LES Modeling. In *Symposium on Hybrid RANS-LES Methods*, pages 27–37. Springer, 2016.

[66] C. Meraner, T. Li, M. Ditaranto, and T. Løvås. Cold flow characteristics of a novel bluff body hydrogen burner. *International Journal of Hydrogen Energy*, 43(14):7155–7168, 2018.

[67] R. S. Miller and J. W. Foster. Survey of Turbulent Combustion Models for Large-Eddy Simulations of Propulsive Flowfields. *AIAA Journal*, pages 2930–2946, 2016.

[68] M. Obersteiner, C. Azar, S. Kossmeier, R. Mechler, K. Moellersten, S. Nilsson, P. Read, Y. Yamagata, and J. Yan. Managing Climate Risk. *IIASA Interim Report*, 2001.

[69] M. Oevermann, H. Schmidt, and A. Kerstein. Investigation of autoignition under thermal stratification using linear eddy modeling. *Combustion and Flame*, 155(3):370–379, 2008.

[70] L. Onsager. The distribution of energy in turbulence. *Physical Review, Proceedings of the American Physical Society*, 68(11-12):281–288, 1945.

[71] L. Onsager. Statistical hydrodynamics. *Il Nuovo Cimento (1943-1954)*, 6 (2):279–287, 1949.

[72] N. Peters. Laminar Diffusion Flamelet Models in Non-Premixed Turbulent Combustion. *Progress in Energy and Combustion Science*, 10(3):319–339, 1984.

[73] N. Peters. *Turbulent Combustion*. Cambridge University Press, 2000.

[74] H. Pitsch and N. Peters. A Consistent Flamelet Formulation for Non-Premixed Combustion Considering Differential Diffusion Effects. *Combustion and Flame*, 114(1-2):26–40, 1998.

[75] Z. E. Platform. The European Technology Platform on Zero Emission Fossil Fuel Power Plants, 2007.

[76] T. Poinsot and D. Veynante. *Theoretical and Numerical Combustion*. RT Edwards, Inc., 2005.

[77] T. Poinsot, D. Veynante, and S. Candel. Quenching processes and premixed turbulent combustion diagrams. *Journal of Fluid Mechanics*, 228:561–606, 1991.

[78] S. B. Pope. A Monte Carlo Method for the PDF Equations of Turbulent Reactive Flow. *Combustion Science and Technology*, 25(5–6):159–174, 1981.

[79] S. B. Pope. PDF methods for turbulent reactive flows. *Progress in Energy and Combustion Science*, 11(2):119–192, 1985.

[80] S. B. Pope. *Turbulent flows*. Cambridge University Press, 2001.

[81] L. F. Richardson. *Weather Prediction by Numerical Process*. Republication. Dover Publ., New York 1965. (Cambridge Univ. Press, London 1922)., 1922.

[82] L. F. Richardson. Atmospheric diffusion shown on a distance-neighbour graph. *Proceedings of the Royal Society of London. Series A, Containing Papers of a Mathematical and Physical Character*, 110(756):709–737, 1926.

[83] W. L. Roberts, J. F. Driscoll, M. C. Drake, and L. P. Goss. Images of the quenching of a flame by a vortex–To quantify regimes of turbulent combustion. *Combustion and Flame*, 94(1–2):58–62, 1993.

[84] S. M. Ross. *Introduction to probability models, 9th ed.* Academic press, 2014.

[85] V. Sankaran. *Sub-grid combustion modeling for compressible two-phase flows*. PhD thesis, Georgia Institute of Technology, 2003.

[86] S. Sannan, A. R. Kerstein, and T. Weydahl. A combustion model based on LEM3D and RANS. Technical report, SINTEF Technical Report, TR, 2008.

[87] S. Sannan, A. R. Kerstein, and T. Weydahl. A 3D geometrical substructure based on LEM. In *European Combustion Meeting 2009*, 2009.

[88] S. Sannan, T. Weydahl, and A. R. Kerstein. Stochastic Simulation of Scalar Mixing Capturing Unsteadiness and Small-scale Structure Based on Mean-flow Properties. *Flow, Turbulence and Combustion*, 90:189–216, 2013.

[89] R. C. Schmidt, R. McDermott, and A. R. Kerstein. ODTLES: A model for 3D turbulent flow based on one-dimensional turbulence modeling concepts. Technical report, Sandia National Laboratories Report SAND2005-0206, 2005–2006.

[90] R. C. Schmidt, A. R. Kerstein, and R. McDermott. ODTLES: A multi-scale model for 3D turbulent flow based on one-dimensional turbulence modeling. *Computer methods in applied mechanics and engineering*, 199(13-16): 865–880, 2010.

[91] J. A. Sethian. A fast marching level set method for monotonically advancing fronts. *Proceedings of the National Academy of Sciences*, 93(4):1591–1595, 1996.

[92] T. Smith and S. Menon. Model simulations of freely propagating turbulent premixed flames. *Symposium (International) on Combustion*, 26(1):299–306, 1996.

[93] T. M. Smith and S. Menon. One-dimensional simulations of freely propagating turbulent premixed flames. *Combustion Science and Technology*, 128(1-6):99–130, 1997.

[94] P. Spalart and V. Venkatakrishnan. On the role and challenges of CFD in the aerospace industry. *The Aeronautical Journal*, 120(1223):209–232, 2016.

[95] D. B. Spalding. Mixing and chemical reaction in steady confined turbulent flames. *Symposium (International) on Combustion*, 13(1):649–657, 1971.

[96] D. B. Spalding. Development of the eddy-break-up model of turbulent combustion. *Symposium (International) on Combustion*, 16(1):1657–1663, 1977.

[97] S. Subramaniam and S. Pope. A mixing model for turbulent reactive flows based on Euclidean minimum spanning trees. *Combustion and Flame*, 115 (4):487–514, 1998.

[98] J. C. Sutherland. A Novel Multi-scale Simulation Strategy for Turbulent Reacting Flows - DE-SC0008998. Technical report, Univ. of Utah, Salt Lake City, UT (United States), 2018.

[99] G. I. Taylor. Statistical theory of turbulence. *Proceedings of the Royal Society of London A: Mathematical, Physical and Engineering Sciences*, 151(873):421–444, 1935.

[100] H. Tennekes, J. L. Lumley, J. Lumley, et al. *A First Course in Turbulence*. MIT press, 1972.

[101] L. H. Thomas. Elliptic problems in linear difference equations over a network. *Watson Sci. Comput. Lab. Rept., Columbia University, New York*, 1949.

[102] J. A. Van Oijen and L. P. H. De Goey. Modelling of Premixed Laminar Flames using Flamelet-Generated Manifolds. *Combustion Science and Technology*, 161(1):113–137, 2000.

[103] H. K. Versteeg and W. Malalasekera. *An Introduction to Computational Fluid Dynamics: The Finite Volume Method, 2nd Edition*. Pearson Education, 2007.

[104] D. Veynante and L. Vervisch. Turbulent combustion modeling. *Progress in Energy and Combustion Science*, 28(3):193–266, 2002.

[105] J. Villermaux. Mixing effects on complex chemical-reactions in a stirred reactor. *Reviews in Chemical Engineering*, 7(1):51–108, 1991.

[106] J. Villermaux and J. Devillon. Représentation de la coalescence et de la redispersion des domaines de ségrégation dans un fluide par un modele d'interaction phénoménologique. *Proc. Second Intl Symp. on Chemical Reaction Engineering*, pages 1–13, 1972.

[107] J. Warnatz, U. Maas, R. W. Dibble, and J. Warnatz. *Combustion, 4th Ed.* Springer, 1996.

[108] T. Weydahl. *A Framework for Mixing-Reaction Closure with the Linear Eddy Model*. PhD thesis, NTNU Trondheim, 2010.

[109] T. Weydahl, S. Sannan, I. R. Gran, and A. R. Kerstein. Modeling Molecular Mixing in Turbulent Reacting Flows. *Proceedings of the European Combustion Meeting*. Chania, Crete, 2007.

[110] K. Zuse. Der Plankalkül. *Bericht der Gesellschaft für Mathematik und Datenverarbeitung*, (63):235–285, 1972.

Article I

Fredrik Grøvdal, Sigurd Sannan, Jyh-Yuan Chen, Alan R. Kerstein and Terese
Løvås

**Three-dimensional Linear Eddy Modeling of a Turbulent Lifted
Hydrogen Jet Flame in a Vitiated Co-flow**

Article II

Fredrik Grøvdal, Sigurd Sannan, Jyh-Yuan Chen and Terese Løvås

A parametric study of LEM3D based on validation with a Turbulent Lifted Hydrogen Jet Flame in a Vitiated Co-flow

A parametric study of LEM3D based on validation with a Turbulent Lifted Hydrogen Jet Flame in a Vitiated Co-flow

Fredrik Grøvdal[a,*], Sigurd Sannan[b], Jyh-Yuan Chen[c], Terese Løvås[a]

[a]*NTNU, Department of Energy and Process Engineering, NO-7034 Trondheim, Norway*
[b]*SINTEF Energy Research, NO-7465 Trondheim, Norway*
[c]*Department of Mechanical Engineering, University of California - Berkeley, Berkeley, CA 94720, USA*

Abstract

A novel model, the hybrid RANS-LEM3D model, is applied to a lifted turbulent N_2 diluted hydrogen jet flame in a vitiated co-flow of hot products from lean H_2/air combustion. In the present modelling approach, mean-flow information from RANS provides model input to LEM3D, which returns the scalar statistics needed for more accurate mixing and reaction calculations. The dependence of lift-off heights and flame structure on iteration schemes and model parameters are investigated in detail, along with other characteristics not available from RANS alone, such as the instantaneous and detailed species profiles and small scale mixing. Furthermore, two different iteration procedures, a breadth-first search and a checkerboard algoritm, as well as parameters of the model framework are examined and tested for sensitivity towards the result. It is found that LEM3D for the current application is able to show additional details compared to the RANS simulation with low computational cost, in comparison to traditional DNS or LES simulations.

Keywords: Turbulent mixing, Linear Eddy Model, Vitiated Co-flow Burner, Kolmogorov scale, Differential diffusion, 3×1D solver

1. Introduction

In efficient and successful design of combustors, e.g., the development of gas turbine combustor designs, the use of validated predictive tools that describe the relevant aspects of the combustion physics and kinetics is crucial in order to reduce emissions and increase efficiency. Experience throughout the last decades has proven that in order to achieve optimum in efficiency and low emissions, high flow rates are important. However, such high flow rates induce chaotic behavior, i.e., turbulence. Turbulent flows are characterized by three-dimensional, rotational, irregular, and intermittent structures on a wide range of scales. Even though there is a general acceptance that the Navier-Stokes equations fully describe turbulent flows, turbulence is still known as one of the most difficult problems to model of classical physics [1]. This is related to the complexity of the equations and the enormous amount of data power needed to obtain satisfactory solutions to real-life applications. At present, direct numerical simulation (DNS) of the Navier-Stokes equations, without the use of any turbulence models, is not feasible for large-scale applications, let alone for turbulent reactive flows. Hence, for engineering and science purposes, high-fidelity numerical simulation tools are based on modeling. With the ever-growing enhancement of computational powers in the past decades, the general focus of modeling has been to develop models and tools with as high predictive powers as possible, given the limitations set by the computational powers available.

A compromise made by conventional models is that they do not explicitly separate molecular mixing and turbulent stirring as distinct processes at the subgrid level. Thus, turbulent stirring, which by nature is advective, is treated as a diffusion process and the dissimilar influences of these mechanisms are smeared out. This is the case both for Large Eddy Simulation (LES) and methods based

---

*Corresponding author.
Email address: `fredrik.grovdal@ntnu.no` (Fredrik Grøvdal)

Nomenclature

Greek Symbols

η	$= (\nu_M/\varepsilon)^{1/4}$ Kolmogorov micro length scale [m]
ν_M	Molecular kinematic viscosity [m²/s]
ν_T	Turbulent kinematic viscosity [m²/s]
ω_ϕ	Reaction rate (production rate) [(kg)$_\phi$/kg/s]
ϕ	Reactive scalar [kg]
ρ	Density [kg/m³]
σ_T	$= \nu_T/D_T$ Turbulent Schmidt number
σ_h	Turbulent Prandtl number of the energy equation
σ_{Y_i}	Turbulent Schmidt numbers of the mass balance equations
ε	Dissipation term in the equation for turbulence energy [m²/s³]
u	Fluid velocity [m/s]

Superscripts

$-$	Mean value
$\sim$	Mass-weighted average value
$,$	Fluctuating value

Latin Symbols

Δt	RANS time step [s]
Δx	RANS cell size [m]
Δx_w	LEM cell size [m]
ξ	Mixture fraction
C_μ	Constant in the k-ε model
D_M	Molecular diffusivity [m²/s]

D_T	Turbulent diffusivity [m²/s]
k	Turbulent kinetic energy [m²/s²]
L_{int}	Integral length scale [m]
p	Scaling exponent in the linear eddy model
t	Time [s]
TM	Triplet Map
W	Molecular weight [g/mol]
X_k	Mole fraction of species k [(mol)$_k$/mol]
Y_k	Mass fraction of species k [(kg)$_k$/kg]
Z	Elemental mass fractions
fac	$= \Delta x_w/\eta$ under-resolving factor
p	Static pressure [Pa=N/m²]

Aberrations

3DCV	Control volume in LEM3D
CFD	Computational fluid dynamics
CFL	Advective Courant-Friedrichs-Lewy number
CV	Control volume
DNS	Direct numerical simulation
LEM	The standalone LInear Eddy Model
LEM$_{res}$	# of LEM wafers in each direction in 3DCV
LEM3D	The three dimensional linear eddy model formulation
LES	Large Eddy simulation
RANS	Reynold's averaged Navier Stokes equation

on the Reynold's Averaged Navier Stokes equations (RANS). In combustion, the explicit distinction between turbulent stirring, diffusive mixing, and chemical reaction at all scales is critical to the overall ability to capture phenomena such as ignition, extinction, unmixedness, and turbulent flame speed, etc. Furthermore, LES and RANS rely on the gradient diffusion model with the counter gradi-

ent assumption,[1] but where LES resolves the largest scales and models the smallest scales (generally assumed to be isotropic), RANS provides no other information than turbulent intensity. Small-scale resolution, however, is needed to give accurate predictions of the mixing and chemistry in turbulent

---

[1]For non-reacting flows the counter gradient assumption means that the averaged transport $\overline{\rho \mathbf{u}'' \phi''}$ of a scalar ϕ is oriented in a direction opposite to the normal gradient turbulent diffusion.

combustion processes.

To capture the principal mechanisms governing turbulent stirring and diffusive mixing, Kerstein formulated the Linear Eddy Model (LEM) [2, 3], which was then extended to include chemical reactions [4]. The One-Dimensional Turbulence (ODT) model, also developed by Kerstein [5], subsumes the capabilities of LEM with regard to mixing and evolves velocity fields in addition to scalar profiles. Both LEM and ODT are one-dimensional models that resolve all scales of turbulent reactive flows at a computationally affordable cost.

Applications of the standalone 1D LEM have been limited to relatively simple flow configurations, such as flows that are homogeneous in at least one spatial direction [6]. For more complex flows, the approach has been to couple the model to global flow solvers. McMurtry et al. [7, 8] proposed to use LEM as a sub-grid mixing and chemistry closure for LES. In this modeling approach, the unresolved length and time scales of LES are captured by individual LEM domains associated with each LES control volume. The coupling between the individual LEM domains is prescribed by the LES-resolved mass-fluxes. The complete LEM-LES model, with two-way coupling between LEM and LES, was later demonstrated for scalar mixing and non-premixed combustion [9]. The LEM-LES model has also been applied to premixed combustion with promising results [10, 11, 12].

The standalone ODT model has been shown to accurately reproduce DNS data for a non-premixed turbulent jet flame [13]. The use of ODT as a subgrid model for LES was first suggested and described by Kerstein [14]. In the ODTLES model, three mutually orthogonal arrays of one-dimensional domains are embedded within the coarser LES mesh [15]. The approach allows for the large-scale turbulent motions to be captured by the LES part of the model, while the small-scale processes are resolved by the ODT along a network of intersecting 1D lines throughout the system. Both LEM-LES and ODTLES represent promising modeling approaches that resolve the turbulence-chemistry interactions at the smallest scales of turbulent reactive flows at a computationally affordable cost compared to DNS.

In this paper we investigate a hybrid model in which a 3-dimensional formulation of the Linear Eddy Model (LEM3D) is used as a post-processing tool for an initial RANS simulation. The use of LEM coupled to RANS has been proposed previously, but to date there has been limited demonstration and evaluation of this approach for combustion applications [16]. The LEM3D approach has been developed by Sannan et al. [17, 18] and is formulated to provide small-scale resolution in all three spatial directions of a turbulent flow field. The formulation incorporates three orthogonally intersecting arrays of 1D LEM domains, with intersecting LEM domains coupled in a Lagrangian sense by non-diffusive fluid-cell displacements. Thus, thermodynamical quantities are advected with no numerical transport, thereby maintaining the strict segregation of advective and molecular diffusive time advancement that provides maximum fidelity for combustion applications. For the work presented here, LEM3D is coupled to the state-of-the-art flow solver ANSYS Fluent, and the coupled RANS-LEM3D tool has the potential of direct industrial application with allowance for complex geometries such as in gas turbine combustors.

In the hybrid RANS-LEM3D approach, LEM3D complements RANS with unsteadiness and small-scale resolution in a computationally efficient manner. The hybrid model is broadly analogous to LEM-LES in its physical treatment, but differs in its overall structure in ways that facilitate its future use as a flexible tool for mixing and chemical reaction simulation within 3D flow solutions. The spatial structure of LEM3D is incidentally the same as in ODTLES, but the domain coupling of LEM3D is expressly designed to avoid numerical transport and its consequences. In the present study, we employ the hybrid RANS-LEM3D model with detailed chemistry to investigate the stabilization mechanism and flame structure of a turbulent lifted hydrogen jet flame in a vitiated co-flow.

The vitiated co-flow burner, used for validation in the present study, was developed at UC Berkeley and first presented by Cabra et al. [19, 20]. The co-flow burner enables studies of flame lift-off and stabilization mechanisms in an environment similar to that of a gas turbine combustor. In practical applications, the lifting of the flame base off the burner has the advantage both of avoiding thermal contact between the flame and the pilot nozzle, which would lead to erosion of the burner material, and potential flashbacks, in particular for hydrogen enriched fuels. The disadvantage of the flame stabilization technique is that the lifted flame blows off more easily than attached flames and therefore must continuously be controlled. The vitiated co-flow burner and similar experiments have been used extensively

for model validation in recent years, e.g., of the Eddy Dissipation Concept by Myhrvold et al. [21], conditional analysis by Cheng et al. [22], and the DQMOM based PDF transport modeling by Lee et al. [23].

The issue of autoignition and lift-off heights of turbulent H_2/N_2 flames issuing into hot co-flows of combustion products has been extensively studied by, e.g., Masri et al. [24] and Cao et al. [25] using PDF calculations. Myhrvold et al. [21] conducted a series of simulations and indicated the extent to which turbulence models influence the predicted lift-off height with Magnussen's Eddy Dissipation Concept [26]. The study of Cao et al. [25] indicates that the lift-off is primarily controlled by chemistry. However, auto-ignition events in unsteady flames have been shown to be controlled by both chemistry and turbulent mixing [27]. The discussion on flame stabilization on the vitiated burner set-ups seemed to be put to an end with the 3D DNS study of a planar hydrogen jet at Sandia National Laboratories by Yoo et al. [28]. In this configuration, with the hydrogen jet issuing with high velocity into hot slow air, the authors concluded that auto-ignition is the key mechanism responsible for flame stabilization of the lifted flame. These findings were later confirmed in the review article by Mastorakos on ignition of turbulent non-premixed flames [29].

This paper aims to give further insight into the sensitivity of the hybrid RANS-LEM3D model to adjustable parameters to demonstrate the strengths of the model but also to point towards issues that require special attention. In Section 2, the LEM3D model is explained in depth. A new iteration scheme previously not used for LEM3D, based on a breadth-first search (BF) [30], is introduced in sub-section 2.4. The coupling of the LEM3D mixing and reaction model to the computational fluid dynamics (CFD) flow solver is established in sub-section 2.6. Parameter and iteration sensitivities are discussed in Section 3 and applied to the vitiated co-flow burner, and the final conclusions are contained in Section 4.

2. Numerical Model and Setup

2.1. The Linear Eddy Model

The Linear Eddy Model is formulated to explicitly distinguish between the effects of turbulent stirring, molecular diffusion, and chemical reaction in a turbulent reactive flow [2, 3, 4]. This is achieved
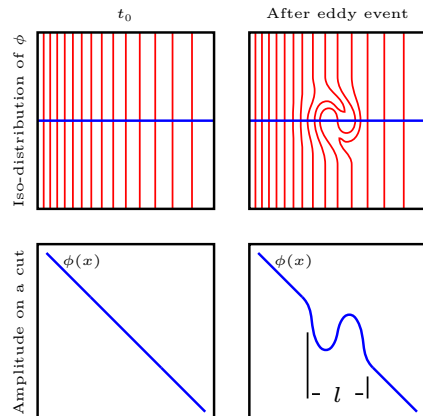

Figure 1: Schematic illustration of the effect of a turbulent eddy of size l on a distribution ϕ in space and the amplitude $\phi(x)$ along a 1D line of sight.

by a reduced description of the scalar fields in one dimension, which makes a full-scale resolution of all spatial and temporal scales, down to the smallest turbulence scales, computationally feasible. The governing transport equation for a reactive scalar ϕ can be expressed as

$$\frac{\partial \rho \phi}{\partial t} = \frac{\partial}{\partial x}\left[\rho D_M \frac{\partial \phi}{\partial x}\right] + TM + \rho \omega_\phi, \tag{1}$$

where ρ is the density, D_M is the molecular diffusivity, and $\rho \omega_\phi$ is the chemical reaction source term. The term TM symbolically denotes randomly occurring stirring events (triplet maps) that punctuate the diffusion and chemical reaction processes.

The triplet maps are stochastic events in LEM that emulate the effects of turbulent eddies on the scalar concentration fields. In Lagrangian terminology, the triplet maps rearrange fluid cells, represented by the computational cells of the discretized one-dimensional domain, in such a manner that scalar lengths are reduced and local gradients are magnified. This is in accordance with the effects of compressive strain in turbulent flow, as illustrated in Figure 1. The left-hand-side of the figure shows an iso-distribution in space of a scalar ϕ and its amplitude along a 1D line of sight at a time t_0. The right-hand-side of the figure illustrates the effect of a turbulent eddy together with molecular diffusion on the iso-contours and the amplitude $\phi(x)$ along the line of sight. In physical flow, molecular diffu-

4

sion and turbulent eddies are continuous processes. In LEM, the eddy events are instantaneous maps sampled from an inertial range size distribution followed by molecular diffusion and eventual chemical reactions in the case of reactive flows.

The turbulent stirring implied by the triplet maps represents turbulent advection and is a distinct physical mechanism governing the mixing of scalar fields. In conventional CFD approaches, such as RANS, turbulent mixing is treated as a diffusion term through the mass-averaged scalar flux $\overline{\rho \widetilde{u_j'' \phi''}} = -\overline{\rho} D_T \frac{\partial \widetilde{\phi}}{\partial x_j}$, where $\overline{\rho}$ denotes the mean of ρ, $\phi'' = \phi - \widetilde{\phi}$ is the fluctuation of ϕ about the Favre-averaged $\widetilde{\phi} = \overline{\rho \phi}/\overline{\rho}$, u_j'' is the fluctuation of the velocity component u_j about the Favre-averaged $\widetilde{u}_j$, and D_T is the turbulent diffusivity. This is called the gradient-diffusion assumption where D_T is positive. The implication is that the scalar flux is in the opposite direction of the mean scalar gradient vector, i.e., the transport of a scalar is always in the direction from a region of high mean concentration to a region of lower concentration. For inhomogeneous, anisotropic or streamline turbulence, however, this might not be the case. In such regions counter-gradient diffusion may occur which does not obey the gradient-diffusion assumption. In LEM, the turbulent diffusivity D_T gives the rate of stirring events.

The molecular diffusion $\frac{\partial}{\partial x}\left[\rho D_M \frac{\partial \phi}{\partial x}\right]$ and chemical reactions $\rho \omega_\phi$ of Eq. (1) are solved directly on the LEM domain. Note that a gradient type model is assumed for the diffusive flux (Fick's law). The reactive-diffusive processes are punctuated by the stochastic triplet map events TM. Hence, the stochastic stirring and mixing processes affect the chemical reactions, and the subsequent heat release and dilatation exhibit random behavior.

It should be noted that there is a governing transport equation (1) for each of the scalars (species, temperature, etc.) in a turbulent reactive flow. Thus, LEM naturally accommodates for multiple chemical species and there is typically a mass diffusivity D_{M_i} associated with each specie i of a gaseous mixture.

2.2. LEM3D

The LEM3D formulation, first described in [17, 18], incorporates three orthogonally intersecting arrays of 1D LEM domains, with intersecting LEM domains coupled in a Lagrangian sense by non-
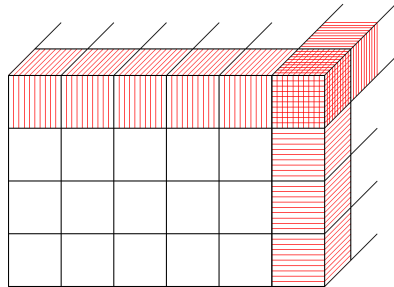

Figure 2: The flow domain of the LEM3D simulation with the coarse Cartesian mesh. The superimposed fine-scale resolution is illustrated by the coloured LEM domains in red, blue and green. One domain is shown in each direction and these intersect in the top-front corner control volume, 3DCV, of the LEM3D domain. Note that the actual LEM resolutions used in the simulations are much higher than shown in the figure.

diffusive fluid-cell transfers from one domain to another. LEM3D thus provides small-scale resolution in all three spatial directions of the turbulent flow field, as well as time-resolved unsteadiness. As in 1D LEM, LEM3D involves stochastic rearrangement events of fluid cells, but is extended to include transfers of fluid cells between the LEM domains. Thereby, LEM3D maintains the explicit distinction of advective and molecular diffusive time advancements which is critical to a high fidelity for combustion applications.

The governing transport equation follows the structure of the 1D LEM, but includes an advection term $\partial(\overline{\rho u_\alpha} \phi)/\partial x_\alpha$, i.e.,

$$\frac{\partial \rho \phi}{\partial t} + \frac{\partial \overline{\rho u_\alpha} \phi}{\partial x_\alpha} = \frac{\partial}{\partial x_j}\left[\rho D_M \frac{\partial \phi}{\partial x_j}\right] + TM_j + \rho \omega_\phi,$$
(2)

where the index j indicates that the terms are implemented on 1D domains in all three spatial directions. Here, TM_j denotes triplet maps occurring on a particular 1D domain. Note that the conventional summation over repeated indices does not apply to the right hand side of the equation.

Diffusive time advancement takes place on each LEM domain in small sub-cycling steps within a coarser time step. The sub-cycling is punctuated by the stochastically occuring stirring events, i.e., the triplet maps.

The coupling of the intersecting LEM domains is associated with the advection term and the larger

time step corresponding to the coarse-grained spatial scale defined by the intersections of orthogonal LEM domains (see Section 2.4 for a comprehensive discussion). By construction, these intersections define a Cartesian mesh of cubic control volumes (3DCVs), as shown in Figure 2. Each of the 3DCVs are resolved in all three spatial directions by an equal number of LEM cells. The advection process $\partial(\overline{\rho u_\alpha}\phi)/\partial x_\alpha$ is governed by an averaged mass-flux $\overline{\rho u}$ which may be prescribed from a global flow solver or measurements. The advection is implemented deterministically by Lagrangian displacements of fluid cells.

The remaining terms of Eq. (2) are explained in Section 2.1. Note, however, that the chemical source term $\rho \omega_\phi$ involves intersecting LEM domains through heat release and thermal expansions. The source term is here solved directly by the use of the stiff solver DVODE [31].

The model input to LEM3D includes mean-flow information such as the mass-flux $\overline{\rho u}$ and the turbulent diffusivity field D_T for the turbulent field. While the mass-flux governs the advective transport of scalars, the turbulent diffusivity governs the turbulent stirring by providing the rate at which turbulent eddy events occur. Both the mass-flux $\overline{\rho u}$ and the diffusivity D_T typically vary in the spatial directions and are resolved at the coarser length scale only, corresponding to the 3DCVs. The mean-flow information is here obtained from an initial RANS simulation, with the values of D_T fed to the centers of the 3DCVs and the face-normal components of $\overline{\rho u}$ provided to the 3DCV faces. Other model inputs to LEM3D include local values, also fed to the 3DCV centers, of the integral length scale L_{int} and the Kolmogorov scale η. A more detailed discussion of the LEM3D model input and the coupling to RANS is contained in Section 2.6.

2.3. Implementation of chemistry

The LEM3D model may be viewed as a '1D-DNS' in all three directions, i.e., all relevant length scales are resolved down to the Kolmogorov scale, or down to the Batchelor scale as needed in case this is smaller than the Kolmogorov scale. Hence, the 1D LEM cells, also called LEM wafers, may be considered as homogeneous reactors with the chemistry implemented directly without any modeling. In previous work [18], unity Lewis number, infinitely fast chemistry and adiabatic conditions were implemented. Further, the chemistry was represented through a single conserved scalar, i.e., the mixture
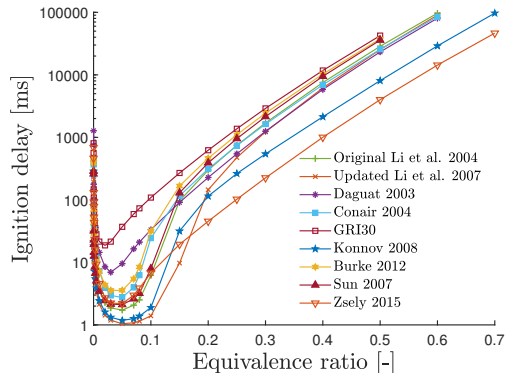

Figure 3: Ignition delay times vs. equivalence ratio for different mechanisms. The inlet conditions for the vitiated co-flow burner were used for this comparison, i.e., $T = 1045$K, $Y_{H_2O} = 0.0989$, $Y_{N_2} = 0.7534$ and $Y_{O_2} = 0.1474$.

fraction ξ. The conserved scalar approach is based on the assumption that the diffusion coefficients for all species are equal, and thus does not account for effects of differential diffusion. Differential diffusion effects, however, have been recognized for a long time to have a significant impact on turbulent hydrogen-rich flames [32, 33, 34]. In the current implementation, the molecular diffusivities D_{M_i} of the individual species i are represented by mixture-averaged quantities [35]. Hence, the model takes into account the effects of differential diffusion, as shown in a previous study [36, 37].

In the current formulation, detailed and finite-rate chemistry is fully implemented from CHEMKIN II. The implicit, backward Euler time integration is employed, where the diffusion time step is given by the linear stability condition $\Delta t_D = \Delta x_w^2/D_{max}$ when Δx_w denotes the LEM wafer size. Here, $D_{max} = \max(D_{M_i,l})$, where $D_{M_i,l}$ is the mixture-averaged diffusion coefficient of species i at the lth cell location of a given LEM domain. For very stiff chemistry, the characteristic chemical time scale associated with the reaction rate may be smaller than the diffusion time scale which could lead to inaccuracies. In this case, the value of D_{max} should be reduced accordingly.

The chemical reaction mechanism employed in the current study is the detailed H_2/O_2 mechanism of Li et al. [38]. The use of the Li mechanism is here chosen from a comparison of ignition delay times of several kinetic schemes with the inlet conditions of the Cabra vitiated co-flow burner,

6

computed with a UC Berkeley in-house code and shown in Figure 3. The investigated mechanisms [38, 39, 40, 41, 42, 43, 44, 45, 46] were selected among all major mechanisms published after 1999, and hence among the most widely used mechanisms in hydrogen combustion [47]. The Li mechanism compares well to most of the other mechanisms, and there are no extremes along the ignition delay curve.

A study looking into detailed reaction mechanisms for hydrogen combustion under gas turbine conditions was done by Ströhle et al. [48]. The investigation showed that the Li mechanism accurately represents H_2/O_2 chemical kinetics at elevated pressures, as present in a typical gas turbine combustor. The Li mechanism has previously also been used in a similar configuration to the Cabra burner, e.g., Yoo et al. [49] conducted a three dimensional DNS simulation of a turbulent lifted hydrogen/air jet flame in a heated co-flow.

2.4. Domain couplings

The benefit of LEM3D compared to a DNS or a LES, namely the computational speed-up, introduces by construction the artifact of solving a 3D-dimensional flow configuration through arrays of coupled 1D domains. The coupling of the LEM domains is hence a crucial part of the model. As discussed in [17], the coupling is associated with the advective time step Δt and consists of two operations:

1. Advective coupling provided by the term $\partial(\overline{\rho u_\alpha}\phi)/\partial x_\alpha$ of Equation (2). The displacement of LEM wafers are based upon the prescribed mass-fluxes $\overline{\rho \boldsymbol{u}}$ given from RANS, while accounting for dilatations from reactions due to the source term $\rho \omega_\phi$. Typically, this involves transfers of wafers among the differently oriented LEM domains intersecting each 3DCV. Conservation of volume is enforced by requiring the displacements of wafers in and out of each 3DCV to obey the equation

$$\sum_{l=1}^{N_{\text{faces}}} \delta_l = 0, \tag{3}$$

where δ_l denotes the integer number of wafer displacements across the 3DCV faces. A 2D illustration of the advection operation is shown in Figure 4.

2. An auxiliary coupling is implemented by stochastic rotations of the 3DCVs. The rotations give additional fluid exchanges between the LEM domains, and ensure that physical processes are consistently represented in all spatial directions. Thus, for every advective time step the 3DCVs are rotated $\pm 90°$ about any of the three coordinate axes with a locally defined probability

$$p_{\text{rot}} = \frac{3}{2} C_{\text{rot}} \cdot \text{CFL}_{\text{3DCV}}, \tag{4}$$

where CFL_{3DCV} is the local Courant-Friedrichs-Lewy number, and C_{rot} is a model constant. The effects of varying C_{rot} are investigated in Section 3. Note that p_{rot} might exceed 1 in the above expression for large C_{rot}, but that the restriction $p_{\text{rot}} \leq 1$ is implemented in the code. Since the rotations introduce diffusive transport, the induced diffusivity D_T^{rot} is deducted from the turbulent diffusivity such that the remaining triplet map diffusivity D_T^{TM} is given by

$$D_T^{TM} = D_T - D_T^{\text{rot}} = D_T - \frac{3}{4} \frac{V_{\text{3DCV}}}{\Delta x} \left\langle \delta^2 \right\rangle. \tag{5}$$

Here, V_{3DCV} is the absolute value of the largest velocity component associated with the 3DCV faces, Δx is the RANS mesh size, and $\left\langle \delta^2 \right\rangle$ denotes the mean-square single rotation displacement of the wafers in the 3DCV in the directions orthogonal to the rotational axis.

Due to the increase of volume through heat release from reactions, following the ideal gas law for constant pressure, there is an associated deviation Ξ_{flux} for each 3DCV between the prescribed mass-fluxes and the actual mass fluxed by LEM3D given by

$$\Xi_{\text{flux}} = \sum_{l=1}^{N_{\text{faces}}} \left(\Delta x_w \sum_{j=1}^{N_l} \rho_{lj} - \overline{\rho u}_l \Delta t \right), \tag{6}$$

where N_l is the number of wafers fluxed over face l, and ρ_{lj} denotes the density of the wafer j fluxed into or out of the 3DCV at face l. The given deviation is an integral part of the current implementation in the variable density framework and in the presence of chemical reactions. This deviation was not present in previous formulations of the model [17] due to the assumption of constant density.
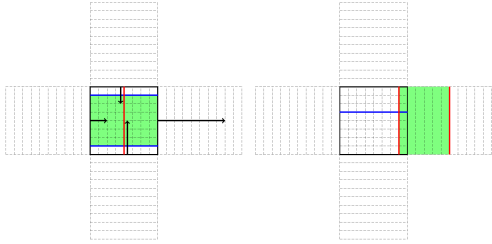
Figure 4: A 2D illustration of the advection operation associated with a given 3DCV. The arrows in the left figure indicate the given wafer displacements in the donor domain (vertical) and the receiver domain (horizontal), with the resulting displacements shown in the figure to the right. The six excess wafers (in green) in the donor are extracted from the center of the 3DCV, rotated counter-clockwise or clockwise (randomly chosen), and then displaced and inserted into the receiver so as to fill the gap created by the advection of that domain. The wafer displacements in the donor correspondingly fill the gap left by the extracted wafers.
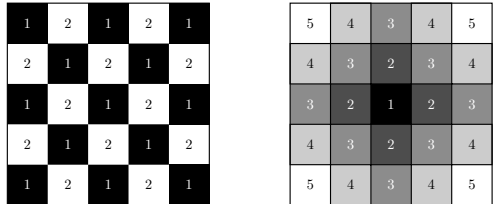

Figure 5: The checker-board algorithm is illustrated on the left. The subsets of minimization are alternated between layers and from time step to time step. To the right the iteration process for the breadth-first search based on the center cell as the root is illustrated.

In order to adapt the deviation Ξ_{flux}, an investigation of various iteration procedures, in combination with least-squares methods to minimize the deviations at each 3DCV cell face, has been performed. In addition to the originally implemented checker-board algorithm, a bread-first search (BF) algorithm has been implemented and employed here. A series of simulations has been conducted to demonstrate the differences between the procedures, with the results shown in Section 3. In more detail the alternative algorithms are given by:

- **The checker-board algorithm:** By the minimization algorithm, final values of the displacements across all interfaces of the 3DCVs are determined by a checker-board routine for each layer of 3DCVs. Since neighbouring 3DCVs share a common face, the minimization of Ξ_{flux} is only feasible, but also sufficient, when the 3DCVs belong to one of the two checker-board subsets of the set of all 3DCVs in each layer, as illustrated in the left-hand side of Figure 5. To ensure a consistent procedure, the selected checker-board subset is alternated for each successive layer of 3DCVs, and also for successive time-advancement cycles. This is the originally used minimization algorithm as presented in [17, 18].

- **The breadth-first search (BF) algorithm:** Originally developed by Zuse [30], and applied here to ensure a smooth spatial distribution of the deviations. The Manhattan Metric[2] is applied as the measure of distance, and the main cell of interest for each layer as the root of the search. The right-hand side of Figure 5 illustrates the iteration procedure, exemplified by the center cell as the root.

As shown in Section 3, the simulations are not only sensitive to the choice of minimization algorithm, but also to the choice of the root in the BF procedure.

2.5. RANS simulation

The initial steady-state RANS simulations of the vitiated co-flow burner to provide mean-flow information to LEM3D are here performed by employing the ANSYS Fluent package, which solves the Reynolds-Averaged Navier-Stokes equations for the mean conservation of mass, momentum and energy, together with the k-ε turbulence model equations. The RANS simulations are performed on a cuboidal $75 \times 75 \times 60$ grid, employing a modified k-ε model.

The jet inlet is approximated by a single cell, where the area of the jet is preserved, i.e., $(\Delta x)^2 = \pi(d/2)^2$, where d is the jet diameter and Δx is the mesh size. The effect of using a square nozzle in this study is assumed to be negligible, justified by an experimental study for a similar burner configuration which indicated that changing from a blunt-edge nozzle to a tapered nozzle bears no discernible impact on the lift-off height L [50]. The lack of sensitivity of L on the nozzle geometry is explained by that the lifted flame is sufficiently far away from the nozzle, that is $L/d \geq 10$, with negligible impact on L from local recirculation around the nozzle

---

[2]Let $x = (x_1, \ldots, x_n)$ and $y = (y_1, \ldots, y_n) \in \mathbb{R}^n$. Then the Manhattan metric is defined as $d(x,y) = \sum_{i=1}^{n} |x_i - y_i|$.

exit. The coarse RANS grid is a somewhat crude approximation, but is chosen here to demonstrate the potential of LEM3D as a post-processing tool to give additional details of the reactive flow.

Table 1: Numerical conditions selected for computing the jet and flame in a vitiated co-flow for RANS.

RANS domain	Cuboid, $75 \times 75 \times 60$
Solver	Steady state
Turbulence model	Modified κ-ε with
	$\quad C_\mu = 0.09$
	$\quad C_{1\varepsilon} = 1.44$
	$\quad C_{2\varepsilon} = 1.83$
	$\quad \sigma_k = 1$
	$\quad \sigma_\varepsilon = 1.3$
	$\quad \sigma_h = 0.7$
	$\quad \sigma_{Y_i} = 0.6$
Turbulence-Chemistry Interaction:	Eddy-Dissipation Concept
Discretization schemes	Standard for pressure SIMPLEC for pressure-velocity coupling Second order upwind for momentum and turbulent kinetic energy
Under-relaxation factors	Pressure= 0.3 Body forces= 0.9 Density= 0.9 Momentum= 0.7

The numerical scheme used for the RANS simulations is given in Table 1. A modified k-ε model is employed, with the constant $C_{2\varepsilon}$ set as in Myhrvold et al. [21] to correct for the overestimated spreading rate for round jets by the standard k-ε model. The boundary conditions used in the computations are detailed in Table 2, and these are the same as used in the simulations by Cabra et al. [19] and by Myhrvold et al. [21]. A series of initial RANS simulations showed that the lift-off height was extremely sensitive to the turbulent Prandtl number σ_h and the turbulent Schmidt number σ_{Y_i}, and the values of these numbers were tuned to obtain a lift-off in agreement with the Cabra experiment. Thus, with the conditions shown in Table 1 and Table 2, the RANS simulation converged to a flame with a lift-off height $L = 10.2\,d$ while Cabra et al. [19] measured a lift-off of $L = 10\,d$ in the burner configuration. The lift-off is defined as the axial location where the OH mass fraction first reaches 600 ppm as used in [19, 20, 21].

During the RANS simulations, certain issues were encountered with respect to flame stabilization. This seems to be due to hysteresis effects. Hysteresis on $T_{\text{co-flow}}$, V_{jet}, and the dilution level $y_{\text{N}_2,\text{jet}}$ affects the stability regimes layout, though

for the vitiated co-flow burner stability is most sensitive to $y_{\text{N}_2,\text{jet}}$. These hysteresis effects influencing the transition to the lifted condition are well known and documented [51]. However, it is reported for a lifted flame with similar conditions that the hysteresis effect will not affect the stability boundaries in the unsteady regime [52].

Table 2: Flame and flow boundary conditions of the jet flame and the co-flow.

	Central jet	Co-flow
Volumetric flow of H_2 [L_{STP}/min]	25	225
Volumetric flow of N_2 [L_{STP}/min]	75	
Volumetric flow of air [L_{STP}/min]		2100
Temperature [K]	305	1045
Mean velocity [m/s]	107	3.5
Reynolds number	23600	18600
Diameter [m]	0.00457	0.21
Mean mole fraction, H_2	0.2537	0.0005
Mean mole fraction, N_2	0.7427	0.7532
Mean mole fraction, O_2	0.0021	0.1474
Mean mole fraction, H_2O	0.0015	0.0989

2.6. The hybrid RANS-LEM3D model

The hybrid model is based on an initial RANS simulation in the Fluent Solver which generates the necessary model input to LEM3D. The RANS model input to LEM3D is mean-flow information such as the mean mass-flux $\overline{\rho u}$ and the turbulent diffusivity D_T of the flow field. The mean mass-flux governs the advective transport of scalars in LEM3D, while the turbulent diffusivity governs the turbulent advection (stirring) by determining the rate at which turbulent eddy events occur. Both the mass-flux and the turbulent diffusivity typically vary in the spatial directions, but are resolved only at the coarser length scale corresponding to the 3DCVs. The values of D_T are fed to the centers of the control volumes, while face-normal components of $\overline{\rho u}$ are provided to the 3DCV faces. The turbulent diffusivity is given by the turbulent viscosity ν_t by

$$D_T = \frac{\nu_T}{\sigma_T} = \frac{C_\mu}{\sigma_T} \frac{k^2}{\varepsilon}, \tag{7}$$

where σ_T is the turbulent Schmidt number (or the Prandtl number when referring to the temperature field), and $C_\mu = 0.09$ [53].

Additional model inputs to LEM3D include local values for the integral length scale L_{int} and the Kolmogorov scale η, as well as a value for the scaling exponent p that governs the eddy-size dependence

in the Kolmogorov inertial cascade range. The integral and Kolmogorov scale are calculated from the k-ε model, respectively given by

$$L_{\text{int}} = C_\mu \, \frac{k^{3/2}}{\varepsilon}, \tag{8}$$

and

$$\eta = L_{\text{int}} \left(\frac{\nu_M}{\nu_T} \right)^{\frac{3}{4}}. \tag{9}$$

The scaling exponent p used in the linear eddy model framework is based on the scaling relation of the turbulent viscosity $\nu_T(l) \propto l^p$, as induced by turbulent eddies of size l or smaller. The scaling exponent is set to $p = 4/3$ on the basis of Richardson's 1926 scaling law $\nu_T(l) \propto 0.6l^{4/3}$ [54], and similarly $\nu_T(\kappa)$ from Kolmogorov's hypothesis based on the inertial range scaling relating the turbulent viscosity to the wave number $\kappa = 2\pi/l$, through $E(\kappa) = C_K \varepsilon^{2/3} \kappa^{-5/3}$ [55, 56].

Table 3: LEM3D input properties

Physical parameters		Model parameters	
Δx	4.05×10^{-3} m	CFL	0.1
Δt	1.25×10^{-6} s	fac	4
Δx_w	5.19×10^{-5} m	LEM_{res}	78
p	1 bar	p	4/3

We here demonstrate the RANS-LEM3D coupling using a coarse steady-state RANS simulation in Fluent for which there is a one-to-one correspondence between the RANS grid cells and the 3DCVs. The LEM3D simulation domain is a cuboidal $31 \times 31 \times 50$ grid and thus a sub-domain of the Fluent domain. In this case, no interpolation is needed and the values of the turbulent diffusivity and the face-normal velocity components are used as direct input to LEM3D. The input profiles are obtained by user-defined functions (UDFs) in Fluent which format the data in line with the proper input format for LEM3D. The LEM3D simulation is performed with the conditions presented in Table 3, where the parameter fac is a under-resolving parameter available for computational saving. Hence, we resolve down to the minimum of fac $\cdot \eta$ in the entire domain, which implies that the number of wafers within the 3DCVs in each coordinate direction is $\text{LEM}_{\text{res}} = \Delta x/\min(\text{fac} \cdot \eta)$. The time advancement is calculated from the CFL number through $\Delta t = \text{CFL} \, \Delta x/\max(|\boldsymbol{u}|)$. Note that the
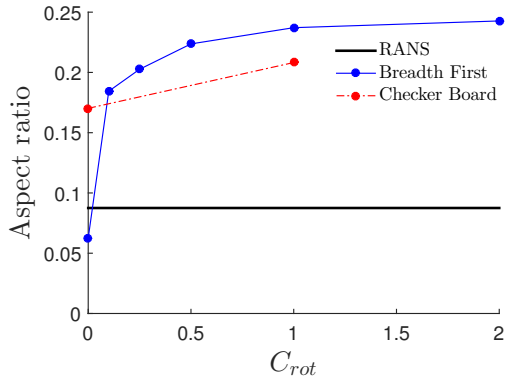

Figure 6: The aspect ratio for the different iteration schemes and values of C_{rot}. The aspect ratio is calculated from the width/height of the iso-surface $\widetilde{Y}_{\text{H}_2} = 0.01$.

above settings are done for simplicity and that any RANS grid could be interpolated into a suitable mesh for LEM3D.

3. Results and Discussion

The coupling of the LEM domains were discussed in Section 2.4. In this section we examine three different iteration procedures and the effects of varying C_{rot} within these;

- The checker-board without least squares (CB)

- The breadth-first with least squares and the root taken as the jet-nozzle (BF)

- The breadth-first with least squares and the root given where the reactions first take place, i.e., the highest concentration of the radical H_2O_2, (BNC).

3.1. Cold flow

We first examine how well LEM3D performs for a flow field without reactions, given the boundary conditions of Table 2. In Figure 6, the aspect ratio based on the width/height of the iso-surface $\widetilde{Y}_{\text{H}_2} = 0.01$ is shown. We observe that a smaller C_{rot}, i.e., a weaker coupling between the domains, results in smaller aspect ratios. Further, for all values of C_{rot}, other than zero, breadth-first has a higher aspect ratio than the checker-board routine. These results coincide well with the contours of both species and temperature (not shown here),
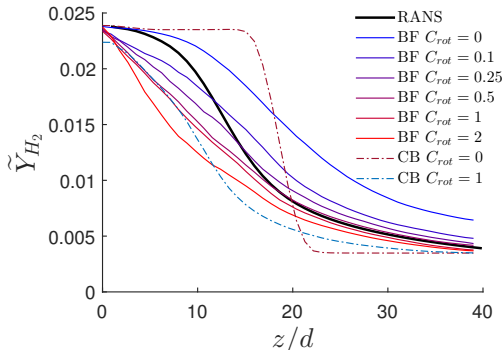
Figure 7: Axial profiles of H_2 for the different iteration routines and values of C_{rot}, time-averaged iterations over 20000 iterations smoothed (i.e. averaged over each 3DCV cell).

Figure 8: Instantaneous axial profile of H_2 of the breadth-first procedure with $C_{rot} = 0.25$.

and indicate that a higher value of C_{rot} induces more diffusion of hydrogen out on the domains surrounding the centerline.

Figure 7 shows the centerline profiles of the H_2 mass fraction resulting from the iteration procedures for different C_{rot}, sampled 20 times at a sampling frequency of every 1000 iterations or approximately two flow-through times. The resulting time-averaged solution is then averaged to 3DCV resolution for comparison with RANS. We observe in the downstream region, i.e. for $z/d > 20$, that all the profiles, except for $C_{rot} = 0$, coincide well with RANS. However, in the upstream region $z/d < 6$, only the $C_{rot} = 0$ profile has a similar decay as the RANS solution. Furthermore, we note that especially the checker-board $C_{rot} = 1$ procedure, first presented in [17, 18], has a non-physical solution with a rapid decay in the range $z/d \in [10, 20]$. It should also be noted that there is a clear trend, as in Figure 7, that for smaller C_{rot} we have less diffusion away from the centerline. Overall, the breadth-first with $C_{rot} = 0.25$ is observed to have the most physical trends in addition to being consistent with RANS. The breadth-first approach generally coincides more than the previously implemented checker-board scheme for the axial profiles, indicating that the new solution procedure is an improvement to the model.

To illustrate the increased information and enhanced resolution given by LEM3D, an instantaneous axial profile of $\widetilde{Y}_{H_2}$ is shown in Figure 8. The profile is sampled after convergence of the breadth-first routine with $C_{rot} = 0.25$. We observe that the downstream profile coincides well with the RANS
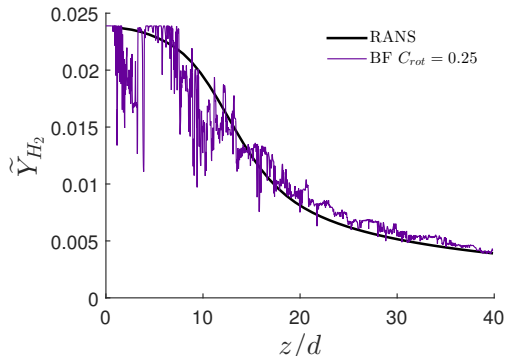
solution, while there is much more fluctuation in the H_2 concentration in the upstream domain, corresponding to effects of the turbulent stirring.

In Figure 9, time-averaged radial profiles of $\widetilde{Y}_{H_2}$ with 3DCV resolution at three axial positions of the jet are shown for the various iteration schemes. At $z/d = 7$, we observe that the profiles for lower values of C_{rot} become sharper and more similar to the RANS profile. However, all the profiles, except for the checker-board $C_{rot} = 0$, predict more spreading of the hydrogen than RANS. At $z/d = 15$, we observe that this particular procedure for $C_{rot} = 0$ gives less spread in the downstream cells since the area below the graph clearly is larger than any of the others. In general, the profiles get sharper with smaller C_{rot}. At $z/d = 30$, we see a clear indication that for both checker-board schemes the advective coupling described in Section 2.4 is not strong enough to couple the 1D LEM domains satisfactorily. This may also be observed by considering the deviating mass-flux Ξ_{flux} at the centerline compared to the surrounding domains. Thorough investigations have shown that at the centerline, Ξ_{flux} will be large in magnitude but negative, while in the neighboring domains Ξ_{flux} has a large positive magnitude. Hence, there is a deficit of advection down the centerline compared to the surrounding domains and we obtain the 'dip' as illustrated by the dashed-doted lines for $z/d = 30$. This was indeed the reason for introducing the breadth-first scheme; that is to obtain an evenly distribution of Ξ_{flux}. Another non-physical profile is the breadth-first procedure with $C_{rot} = 0$. This routine gives a too sharp gradient compared to both RANS and to
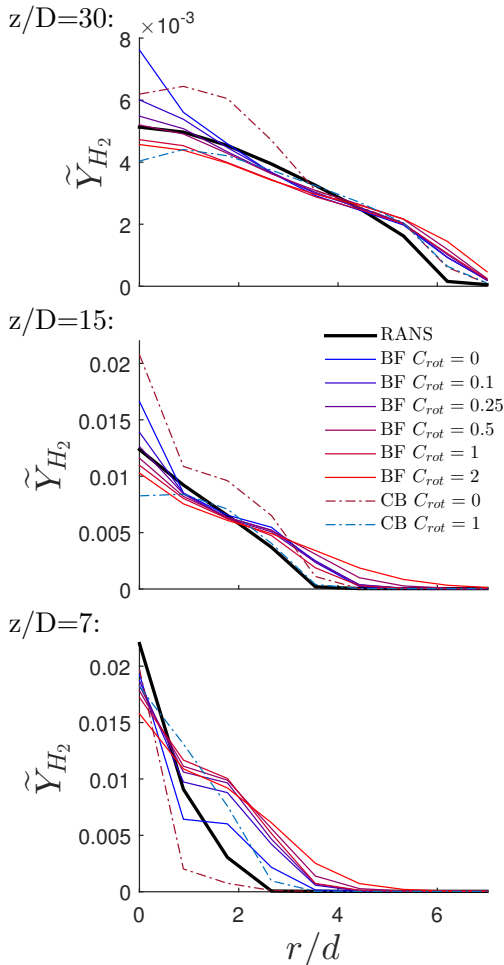
Figure 9: Radial profiles of H₂ at the three axial positions $z/d = 7$, 15 and 30.

the other profiles. At $z/d = 30$, the breadth-first routine with $C_{rot} = 0.5$ coincides well with RANS for $r \in [-5, 5]$.

The observed decrease in H_2 with increasing C_{rot} has been thoroughly investigated. It has shown to be an artifact in the construction of the coupled 1D domains. With higher values of C_{rot}, we introduce more frequent sharp gradients in between the control volumes, simultaneously as we require rotation to couple the domain. Hence, an optimum needs to be estimated for each case. For non-reacting simulations, $C_{rot} = 0.25$ is generally preferable for the use of the breadth-first scheme while the checker-board algorithm generally performs best with $C_{rot} = 1$. Overall, for the non-reacting simulation the breadth-first $C_{rot} = 0.25$ procedure is to give the most physical and appropriate match with the RANS profiles at time average and would hence be the most beneficial for post-processing of RANS.

3.2. Lifted flame

We here consider the same set-up as in Section 3.1, but with chemical reactions as described in Section 2.3. For the reactive study we include the breadth-first iteration scheme with the root determined by where the reactions take place, i.e., at the highest concentration of the radical H_2O_2 (BNC).

In Figure 10, the lift-off height and non-reacting flame volume are shown versus C_{rot} for the different iteration schemes used in the reacting case. The non-reacting flame volume is calculated using the Riemann-integral of the volume enclosed by the upstream concave surface defined along the iso-lines of $\tilde{Y}_{OH} = 600$ ppm and its normals down to the inlet plane. Notice that this surface will contain the lift-off point. The non-reacting flame volume (NRFV) is defined by

$$\text{NRFV} = \int_{\theta=0}^{2\pi} \int_{r=-R_L}^{R_L} H(r, \theta) \, dr d\theta, \tag{10}$$

where R_L denotes the radial position of the lift-off point and $H(r, \theta)$ is a function giving the flame-front normalized by the jet diameter. This is found by taking the value of the time-averaged iso-line of $\tilde{Y}_{OH} = 600$ ppm at the point (r, θ).

We observe that both parameters, i.e., the lift-off height L and the NRFV indicate that the simulations yield different profiles than the RANS solution. The lift-off L increases somewhat with decreasing C_{rot}, while the trend is not equally clear
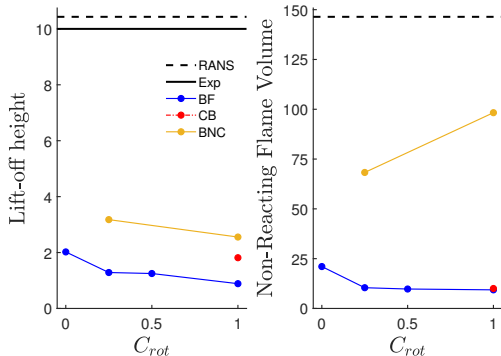
Figure 10: Lift-off height (L/d) and the non-reacting flame volume vs. C_{rot} and the different iteration regimes for the reacting case.

for NRFV. However, using the BNC as the iteration procedure results in a better agreement with the experiments and RANS. For all cases, we also note that the NRFV gives a more physical prediction in comparison to the lift-off alone when it comes to describing the flame shape. The NFRV accounting for the unphysical jet-penetration into the flame, typically seen for values of C_{rot} close to and equal to zero, while the lift-off height just indicate the first occurrence of $\widetilde{Y}_{OH} = 600$ ppm. This unphysical jet-penetration can be seen e.g. in the contours of BF $C_{rot} = 0.25$ in Figure 11.

3.2.1. Contour plots

The OH contours of Figure 11 show the various flame shapes based on the 3DCV-averaged solutions for the different iteration schemes. The leftmost sub-figure show the profile of the RANS simulation, supporting the contours of Myhrvold et al. [21]. In the second sub-figure from the left, the checker-board scheme with $C_{rot} = 1$ yields a non-physical dip on the centerline of the contour. This dip, which is also present in the mixture fraction contours (not shown here), indicates that the jet fuel almost vanishes from centerline at this axial location. This is a result of the lack of sufficient entrainment to the centerline provided by the checker-board scheme, letting the jet disperse out of the centerline to the neighboring domains. As a consequence, there are enhanced reactions in the domains surrounding the centerline at the expense of possible centerline reactions, and hence the dilatations are too small in the centerline domain and too large in the surrounding domains. The mass-flux deviation Ξ_{flux} of Eq. (6)

is the largest where the reactions take place, and hence the 1D domains containing enhanced reactions will impose large deviations in these domains. Thus, Ξ_{flux} will be large in the domains surrounding the centerline, while Ξ_{flux} along the centerline domain is enforced to have large, negative values. The checker-board scheme therefore gives an advection deficit along the centerline, explaining the non-physical dip mentioned above. The three rightmost sub-figures of 11 display the flame structures for various breadth-first schemes, all with a more physical appearance than the checker-board scheme.

As discussed in Section 3.2, the various LEM3D simulations all give a low lift-off height compared to both RANS and the experiments [19]. However, as indicated by the experimental contours shown in [19, 20], the radial stabilization of the lift-off point occurs at about $r/d = 1.2$ and this is reflected both by the CB and BF iteration schemes. In this regard, both the BNC profiles and the RANS stabilize at a wider radial distance of $r/d \approx 1.8$. The experimental measurements also indicate that below $z/d = 25$ the width of the flame is no wider than $r/d \approx 2$. The RANS here gives a width as large as $r/d = 3.8$, while all of the LEM3D simulations provide a width in the range $r/d \in [2.1, 2.8]$. It should be noted that the overspreading is a known problem and that all models in [19, 21] over-predict the width of the flame stabilization region compared to experiments. Concerning the overall flame structure, here illustrated by the shape of the 600 ppm iso-contours, the breadth-first scheme with root not in the center produces OH contours that seem to have the most physical and comparable shape to experiments.

3.2.2. Axial profiles

Centerline profiles of the mixture fraction, the temperature and the density-averaged mass fractions of O_2, H_2O, H_2, and OH for the lifted flame obtained with various iteration procedures are compared to experimental data and shown in Figure 12. The axial profiles are based on 20 time-averaged samples and averaged to 3DCV resolution for comparison with RANS. It should be noted that since the LEM3D schemes predict a smaller lift-off than RANS, as indicated by Figures 10 and 11, the profiles are expected to be shifted.

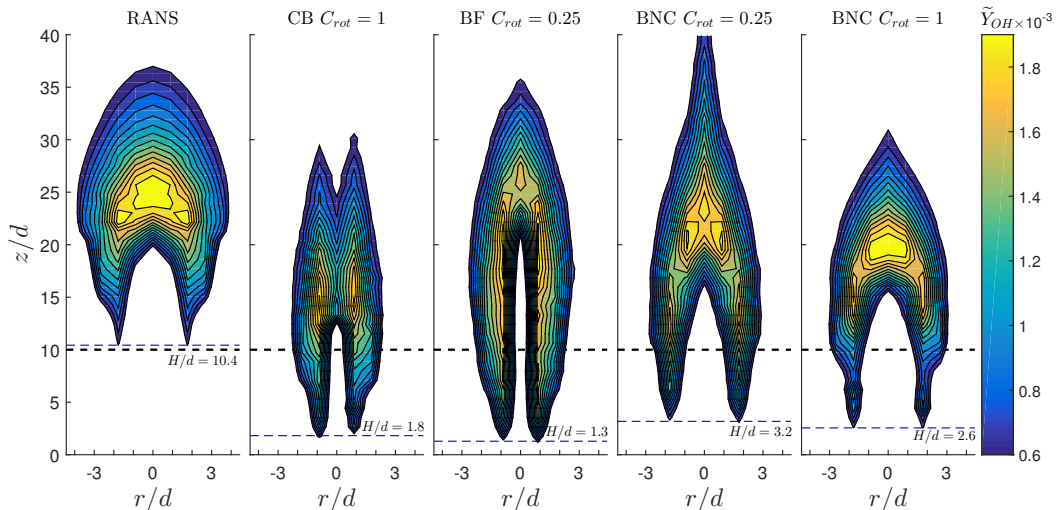The mixture fraction ξ is computed using Bilger's formula [57] based on the elemental mass fractions

13

Figure 11: OH contour plots of the RANS and the four iteration schemes investigated in this section. The black line indicates the experimental lift-off $H/d = 10$, and the blue line indicates the lift-off for the given simulation.

of the fuel and oxidizer, i.e.,

$$\xi = \frac{0.5\,Z_{\mathrm{H}}/W_{\mathrm{H}} + (Z_{\mathrm{O},0} - Z_{\mathrm{O}})/W_{\mathrm{O}}}{0.5\,Z_{\mathrm{H},F}/W_{\mathrm{H}} + Z_{\mathrm{O},0}/W_{\mathrm{O}}}, \qquad (11)$$

where the subscripts F and O denote the fuel and the oxidizer streams, W is the molecular weights, and Z_{H} and Z_{O} are elemental mass fractions of hydrogen and oxygen, respectively.

As seen from the profiles, the BNC and the BF curves generally follow similar trends with some differences in the axial location of the peaks of the H_2O, OH, and temperature profiles. For the mixture fraction, there is good agreement between these curves, the RANS, and the experimental results. The CB curves basically fail in predicting the experimental trends correctly. The value of the OH peak is generally over-predicted by a factor of two for all the simulations (including the RANS).

As discussed by Myhrvold et al. [21], the results for the axial O_2 profiles are related to the predicted lift-off height. Since the RANS simulation with the modified k-ε model gave a lift-off of $L = 10.2\,d$, it allows for more diffusion of O_2 towards the centerline since the oxygen is consumed by the flame at a later axial location than for the LEM3D simulations. The O_2 peak illustrates the downstream penetration and subsequent consumption of the O_2. The peak is generally higher for models that predict

higher lift-off since there is a slower consumption of O_2 and hence more oxygen is diffused to the centerline. Except for the BF iteration scheme, the CB and BNC schemes of LEM3D yield an earlier reaction at the centerline as observed from the contours of Figure 11. The earlier reaction is also observed by the earlier consumption of H_2, an earlier OH peak, and consequently an earlier production of H_2O as shown in Figure 12.

The profiles of Figure 13 are instantaneous LEM resolved profiles compared to RANS and the experimental values. The trend with the difference in predicted lift-off is more evident here, as it is clear that the overall shape agrees for all profiles but are shifted a distance $7.4\,d$ upstream compared to the experimental lift-off. As discussed in the previous paragraph, the under-prediction of the lift-off results in no primary peak of the O_2-profile. Further, we observe that most of the larger eddies exists, as expected from the flow field (not plotted here), in the range $z/d \in [5, 20]$.

3.2.3. Scatter plots

In this section, scatter plots comparing experimental results to the best performing scheme, i.e., the breadth-first with least squares and the root given were the reactions first take place, are discussed. Figure 14 shows scatter data of the tem-
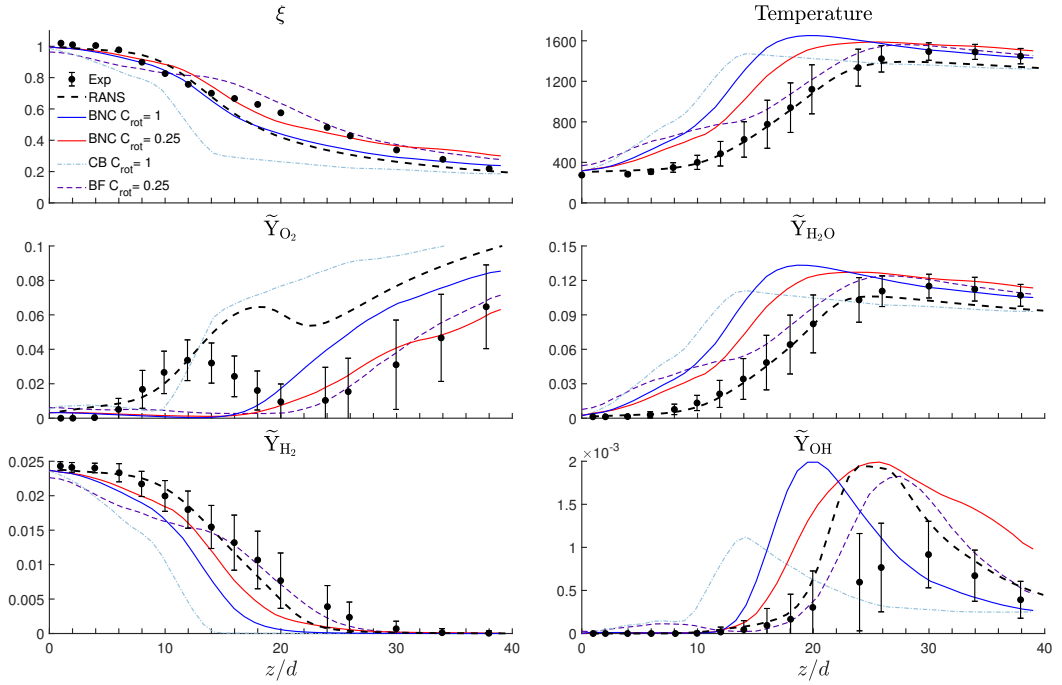
14

Figure 12: Axial profiles of various scalars shown for the different iteration routines and compared with RANS and the experimental results to illustrate. The profiles are based on a time-averaged solution over 20 samples and smoothed to 3DCV resolution. The mixture fraction profile fits very well with the measurements, while there are various differences for the other curves.
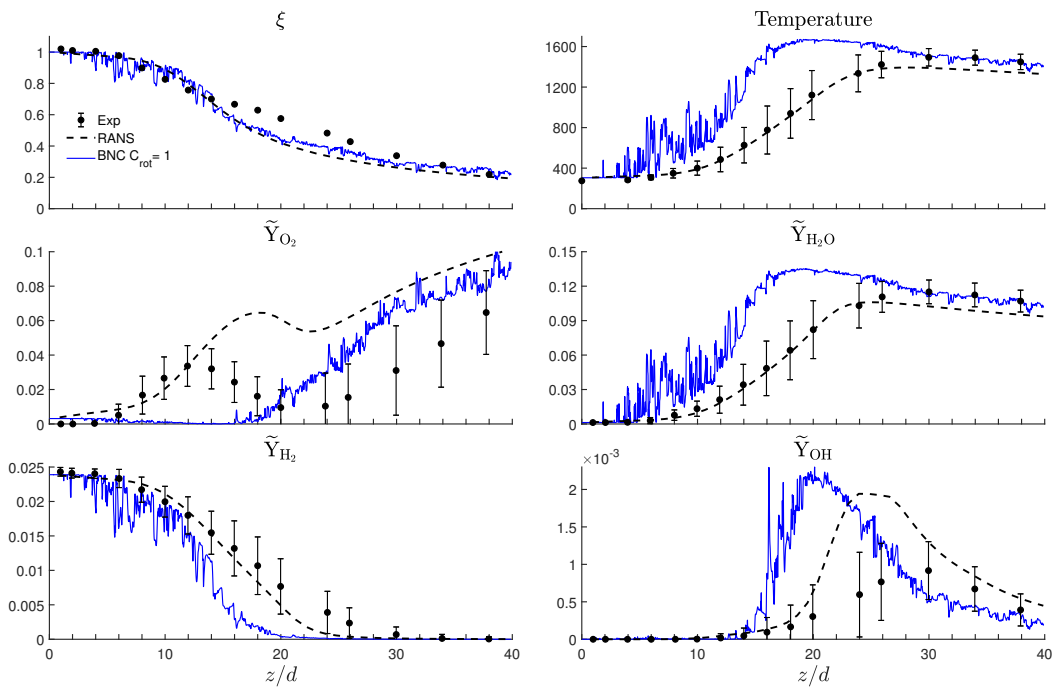
Figure 13: Axial LEM-resolved instanteous profiles of various scalars after convergence.

16

perature versus the mixture fraction at five different axial positions, $z/d \in \{8, 9, 10, 11, 26\}$, together with theoretical values for mixing without reaction and adiabatic equilibrium for comparison. The right-hand side of Fig. 14 shows experimental results. Approximately 4000 point measurements were grouped together from different radial positions to form a probability density map. The left-hand side gives the LEM3D scatter data based on small-scale wafer resolution (black dots), 3DCV averaged results (green dots), and the underlying RANS results for the simulation (blue dots). The LEM resolved results are sampled for each point at the plane normal to the jet for each of the axial positions in a single time step after convergence.

None of the flames are attached to the nozzle, but at $z/d \approx 8$ where hot oxides from the co-flow are getting entrained in the experiments, evolving into a partially premixed flow with fluid temperatures corresponding to the mixing line between the jet and the co-flow boundary conditions, the mixing in LEM3D seems already to have approached a fast chemistry limit. Since the LEM3D iteration schemes yield small lift-offs, the flame structure is different compared to the experiments. While in the experiments there is a clear progression from a predominantly mixing condition to a vigorous flame burning that corresponds to the transition from mixing only to mixing combined with ignition and flame stabilization, the LEM3D scheme tends to lay close to the adiabatic equilibrium limit and thus indicates a too high rate of reactions.

For both scatters there is progressive dilution of the richest samples beyond the potential core of the jet, such that the fuel-rich boundary condition for combustion gradually decreases from $\xi = 1$ to values $\xi \in [0.6, 0.7]$. Again, as for the axial profiles, we observe that the data tend to be more similar in the far-field region than in the near field.

4. Conclusions

The focus of the present work has been to demonstrate the LEM3D with the novel breadth-first iteration scheme and to test the model capabilities vs. RANS and experimental measurements. The LEM3D model has here been applied to a turbulent lifted hydrogen jet flame in a vitiated co-flow. LEM3D contributes with information not available from RANS alone, e.g., scatter plots and instantaneous profile. This kind of information is of great importance when practical implications are taken into consideration.

Even though LEM3D shows good agreement with experiments in the far field, currently the algorithms do not yield a lift-off height in accordance with the experiments. Thorough investigations of this feature has been done, which has shown that the rotations are causing an increased spread of H_2, as most easily observed in the non-reactive case. Combined with low fluxes in the LEM domains surrounding the central jet nozzle, and the treatment in LEM3D of three dimensions as $3\times1D$, the conditions and residence times are sufficient for reactions, stabilizing the flame at a low lift-off. However, near-field discrepancy is a previously known model artifact of LEM resulting from the instantaneous nature of the eddy events [4], and among other things the undeveloped energy spectrum.

LEM3D is further shown to be sensitive to numerical implementation details such as the coupling scheme and the rotation factor C_{rot}. Possible improvements in this regard are noted. The sensitivity cannot be thoroughly evaluated here because the chosen application constrains important aspects of numerical implementation. Other such sensitivities have been examined for simple flows[18] and mixing without chemical reactions[17].

To a large degree, the limitations of LEM3D in this context are a result of the reliance on RANS-type steady-state inputs rather than concurrent unsteady time advancement of LEM3D coupled to LES. Though this would undoubtedly improve model performance, as indicated by previous LEM-LES applications, the present goal is to assess the degree of improvement of RANS performance for mixing and combustion applications that can be achieved by introducing LEM closure. Any such improvement would be beneficial due to the relatively low cost and wide usage of RANS. The results presented here suggest that there is at least some significant range of applications for which LEM3D coupling to RANS provide useful performance improvement.

While previous studies and the experimental data did not have clear evidence of autoignition events below the lift-off height, it was seen in the current work that autoignition, or turbulent mixing of products and reactants in the stabilization region followed by rapid ignition, seemed to cause stability in LEM3D.

In further work, more complex flame configurations should be investigated, e.g., DNS of the jet-
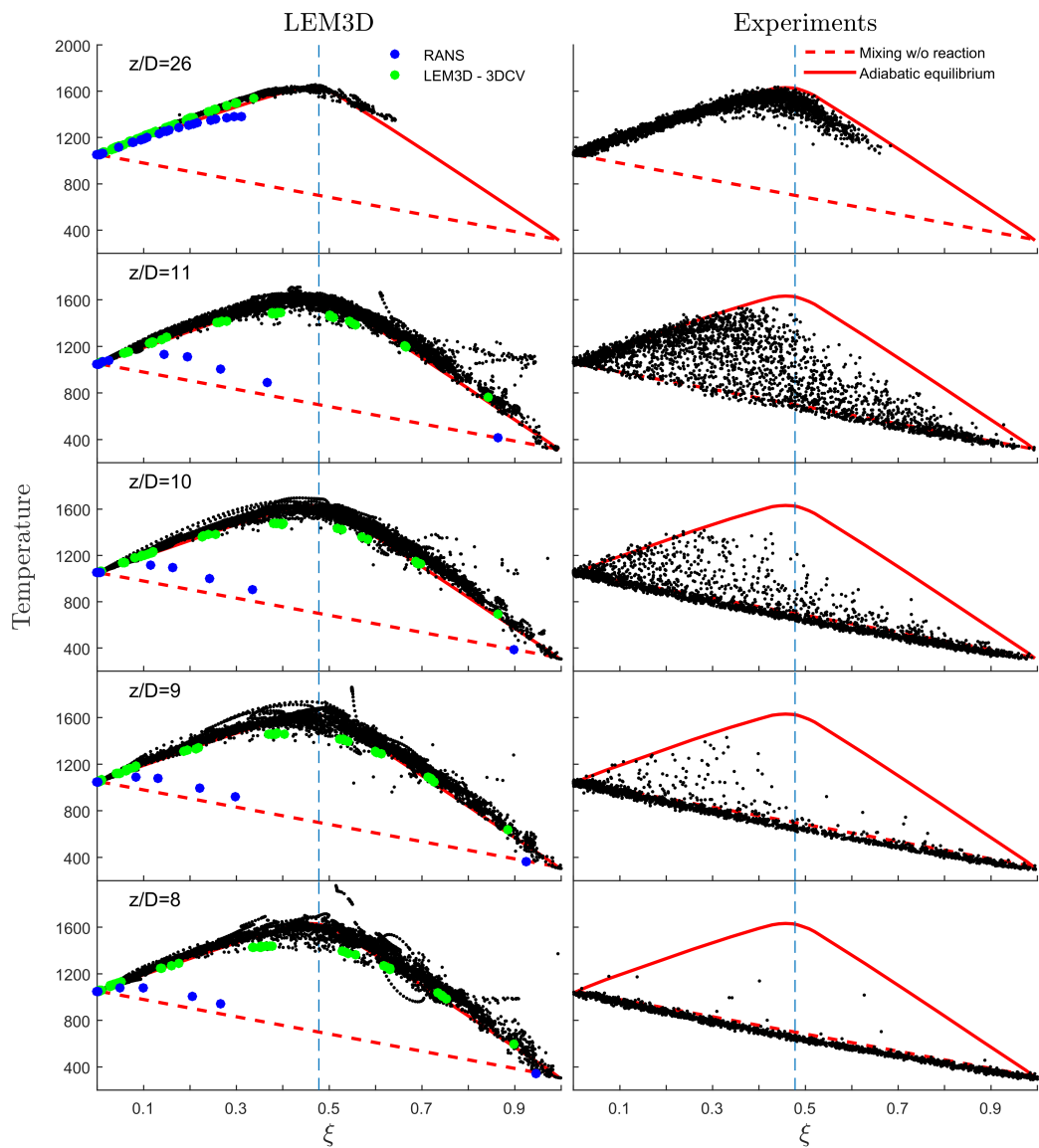
Figure 14: Scatter data of the temperature versus the mixture fraction at five axial positions of both LEM3D and RANS (left), and the experiments conducted by Cabra et al. [19] (right). The red curves indicate theoretical values for mixing without reaction and adiabatic equilibrium. For the left side of the figure, the blue, the red and the black dots show the underlying RANS solution to LEM3D (initial values for the simulation), the 3DCV averaged values for LEM3D, and the LEM-resolved values, respectively.

in-cross-flow configuration [58] and the turbulent lifted hydrogen flame in a slot burner [49]. Pressure will be included as a transport variable in the code, to account for pressure-gradients in the initial flow field, and other alternatives to treat thermal expansion will be considered to reduce the deviationg mass-flux Ξ_{flux}.

Acknowledgments

Compliance with Ethical Standards

Conflict of interests The authors declare that they have no conflict of interest.

References

[1] R. P. Feynman, R. B. Leighton, M. L. Sands, The Feynman Lectures on Physics, Vol. 1, Addison-Wesley, 1964.

[2] A. R. Kerstein, A linear-eddy model of turbulent scalar transport and mixing, Combustion Science and Technology 60 (4-6) (1988) 391–421.

[3] A. R. Kerstein, Linear-eddy modelling of turbulent transport. Part 6. Microstructure of diffusive scalar mixing fields, Journal of Fluid Mechanics 231 (1991) 361–394.

[4] A. R. Kerstein, Linear-eddy modelling of turbulent transport. Part 7. Finite-rate chemistry and multi-stream mixing, Journal of Fluid Mechanics 240 (1992) 289–313.

[5] A. R. Kerstein, One-dimensional turbulence: model formulation and application to homogeneous turbulence, shear flows, and buoyant stratified flows, Journal of Fluid Mechanics 392 (1999) 277–334.

[6] P. A. McMurtry, T. C. Gansauge, A. R. Kerstein, S. K. Krueger, Linear eddy simulations of mixing in a homogeneous turbulent flow, Physics of Fluids A: Fluid Dynamics 5 (4) (1993) 1023–1034.

[7] P. A. McMurthy, S. Menon, A. R. Kerstein, A linear eddy sub-grid model for turbulent reacting flows: Application to hydrogen-air combustion, in: Symposium (International) on Combustion, Vol. 24, Elsevier, 1992, pp. 271–278.

[8] P. McMurtry, S. Menon, A. Kerstein, Linear eddy modeling of turbulent combustion, Energy & fuels 7 (6) (1993) 817–826.

[9] S. Menon, W. H. Calhoon Jr, Subgrid mixing and molecular transport modeling in a reacting shear layer, in: Symposium (International) on Combustion, Vol. 26, Elsevier, 1996, pp. 59–66.

[10] V. Chakravarthy, S. Menon, Subgrid modeling of turbulent premixed flames in the flamelet regime, Flow, Turbulence and Combustion 65 (2) (2000) 133–161.

[11] V. Sankaran, S. Menon, Subgrid combustion modeling of 3-D premixed flames in the thin-reaction-zone regime, Proc. Comb. Inst. 30 (2005) 575–582.

[12] B. A. Sen, S. Menon, Linear eddy mixing based tabulation and artificial neural networks for large eddy simulations of turbulent flames, Combustion and Flame 157 (2010) 62–74.

[13] N. Punati, J. C. Sutherland, A. R. Kerstein, E. R. Hawkes, J. H. Chen, An evaluation of the one-dimensional turbulence model: Comparison with direct numerical simulations of CO/H2 jets with extinction and reignition, Proc. Comb. Inst. 33 (2011) 1515–1522.

[14] A. R. Kerstein, One-dimensional turbulence: A new approach to high-fidelity subgrid closure of turbulent flow simulations, Computer Physics Communications 148 (1) (2002) 1–16.

[15] R. C. Schmidt, A. R. Kerstein, R. McDermott, Odtles: a multi-scale model for 3d turbulent flow based on one-dimensional turbulence modeling, Comput. Methods Appl. Mech. Eng. 199 (2010) 865–880.

[16] G. M. Goldin, S. Menon, W. H. Calhoon, Jr, A linear eddy mixing model for steady non-premixed turbulent combustion, in: 33rd Aerospace Sciences Meeting and Exhibit, 1995, p. 379.

[17] S. Sannan, T. Weydahl, A. R. Kerstein, Stochastic simulation of scalar mixing capturing unsteadiness and small-scale structure based on mean-flow properties, Flow, Turbulence and Combustion 90 (2013) 189–216.

[18] T. Weydahl, A Framework for Mixing-Reaction Closure with the Linear Eddy Model, Ph.D. thesis, NTNU Trondheim, 2010.

[19] R. Cabra, T. Myhrvold, J. Chen, R. Dibble, A. Karpetis, R. Barlow, Simultaneous laser Raman-Rayleigh-Lif measurements and numerical modeling results of a lifted turbulent H2/N2 jet flame in a vitiated coflow, Proc. Comb. Inst. 29 (2002) 1881–1888.

[20] R. Cabra, Turbulent Jet Flames Into a Vitiated Coflow, Ph.D. thesis, UC Berkeley, 2003.

[21] T. Myhrvold, I. Ertesvåg, I. Gran, R. Cabra, J.-Y. Chen, A numerical investigation of a lifted H2/N2 turbulent jet flame in a vitiated coflow, Combustion Science and Technology 178 (2006) 1001–1030.

[22] T. Cheng, J. Wehrmeyer, R. Pitz, Conditional analysis of lifted hydrogen jet diffusion flame experimental data and comparison to laminar flame solutions, Combustion and Flame 150 (2007) 340–354.

[23] J. Lee, Y. Kim, DQMOM based PDF transport modeling for turbulent lifted nitrogen-diluted hydrogen jet flame with autoignition, International Journal of Hydrogen Energy 37 (2012) 18498–18508.

[24] A. Masri, R. Cao, S. Pope, G. Goldin, PDF calculations of turbulent lifted flames of H2/N2 fuel issuing into a vitiated co-flow, Combustion Theory and Modelling 8 (2004) 1–22.

[25] R. R. Cao, S. B. Pope, A. R. Masri, Turbulent lifted flames in a vitiated coflow investigated using joint PDF calculations, Combustion and flame 142 (2005) 438–453.

[26] B. F. Magnussen, Modeling of NOx and soot formation by the Eddy Dissipation Concept, Int. Flame Research Foundation (1989).

[27] B. Johannessen, A. North, R. Dibble, T. Løvås, Ex-

perimental studies of autoignition events in unsteady hydrogen–air flames, Combustion and Flame 162 (2015) 3210–3219.

[28] C. S. Yoo, R. Sankaran, J. H. Chen, Direct numerical simulation of turbulent lifted hydrogen jet flame in heated coflow.

[29] E. Mastorakos, Ignition of turbulent non-premixed flames, Progress in Energy and Combustion Science 35 (1) (2009) 57–97.

[30] K. Zuse, Der Plankalkül, no. 63, Gesellschaft für Mathematik und Datenverarbeitung, 1972.

[31] P. N. Brown, G. D. Byrne, A. C. Hindmarsh, Vode: A variable-coefficient ode solver, SIAM journal on scientific and statistical computing 10 (5) (1989) 1038–1051.

[32] R. Bilger, Molecular transport effects in turbulent diffusion flames at moderate reynolds number, AIAA Journal 20 (7) (1982) 962–970.

[33] B. MOO LEE, H. DONG SHIN, Differential diffusion effects in h2/n2 turbulent nonpremixed flames, Combustion science and technology 62 (4-6) (1988) 311–330.

[34] F. Bisetti, J.-Y. Chen, J. H. Chen, E. R. Hawkes, Differential diffusion effects during the ignition of a thermally stratified premixed hydrogen–air mixture subject to turbulence, Proceedings of the Combustion Institute 32 (1) (2009) 1465–1472.

[35] R. B. Bird, W. E. Stewart, E. N. Lightfoot, Transport Phenomena John Wiley & Sons, New York (1960) 413.

[36] S. Sannan, A. R. Kerstein, Numerical simulation of differential molecular diffusion effects in a hydrogen-rich turbulent jet using lem3d, Energy Procedia 51 (2014) 253–258.

[37] S. Sannan, A. R. Kerstein, Differential molecular diffusion in a hydrogen-rich jet, Energy Procedia 86 (2016) 304–314.

[38] J. Li, Z. Zhao, A. Kazakov, F. L. Dryer, An updated comprehensive kinetic model of hydrogen combustion, International journal of chemical kinetics 36 (2004) 566–575.

[39] J. Li, Z. Zhao, A. Kazakov, M. Chaos, F. L. Dryer, J. J. Scire, A comprehensive kinetic mechanism for co, ch2o, and ch3oh combustion, International Journal of Chemical Kinetics 39 (3) (2007) 109–136.

[40] P. Dagaut, F. Lecomte, J. Mieritz, P. Glarborg, Experimental and kinetic modeling study of the effect of no and so2 on the oxidation of co-h2 mixtures, International Journal of Chemical Kinetics 35 (11) (2003) 564–575.

[41] M. Ó Conaire, H. J. Curran, J. M. Simmie, W. J. Pitz, C. K. Westbrook, A comprehensive modeling study of hydrogen oxidation, International Journal of Chemical Kinetics 36 (11) (2004) 603–622. doi:10.1002/kin.20036.
URL http://doi.wiley.com/10.1002/kin.20036

[42] G. P. Smith, D. M. Golden, M. Frenklach, N. W. Moriarty, B. Eiteneer, M. Goldenberg, C. T. Bowman, R. K. Hanson, S. Song, W. C. Gardiner, Jr., V. V. Lissianski, Z. Qin, http://www.me.berkeley.edu/gri_mech/.

[43] A. A. Konnov, Remaining uncertainties in the kinetic mechanism of hydrogen combustion, Combustion and Flame 152 (4) (2008) 507–528. doi:10.1016/j.combustflame.2007.10.024.
URL http://linkinghub.elsevier.com/retrieve/pii/S0010218007003318

[44] M. P. Burke, M. Chaos, Y. Ju, F. L. Dryer, S. J. Klippenstein, Comprehensive H2/O2 kinetic model for high-pressure combustion, International Journal of Chemical Kinetics 44 (7) (2012) 444–474. doi:10.1002/kin.20603.
URL http://doi.wiley.com/10.1002/kin.20603

[45] H. Sun, S. Yang, G. Jomaas, C. Law, High-pressure laminar flame speeds and kinetic modeling of carbon monoxide/hydrogen combustion, Proceedings of the Combustion Institute 31 (1) (2007) 439–446.

[46] I. G. Zsély, J. Zádor, T. Turányi, Uncertainty analysis of updated hydrogen and carbon monoxide oxidation mechanisms, Proceedings of the Combustion Institute 30 (1) (2005) 1273–1281.

[47] C. Olm, I. G. Zsély, R. Pálvölgyi, T. Varga, T. Nagy, H. J. Curran, T. Turányi, Comparison of the performance of several recent hydrogen combustion mechanisms, Combustion and Flame 161 (9) (2014) 2219–2234.

[48] J. Ströhle, T. Myhrvold, An evaluation of detailed reaction mechanisms for hydrogen combustion under gas turbine conditions, International Journal of Hydrogen Energy 32 (1) (2007) 125–135.

[49] C. S. Yoo, J. H. Chen, R. Sankaran, A 3d dns study of the stabilization of a turbulent lifted hydrogen/air jet flame in an autoignitive heated coflow, in: Fall Meeting of the Western States of the Combustion Institute, 2007.

[50] A. North, M. Magar, J.-Y. Chen, R. Dibble, A. Gruber, Effect of pressure, environment temperature, jet velocity and nitrogen dilution on the liftoff characteristics of a n2-in-h2 jet flame in a vitiated co-flow, Eurasian Chemico-Technological Journal 16 (2-3) (2014) 141–148.

[51] K. M. Lyons, Toward an understanding of the stabilization mechanisms of lifted turbulent jet flames: Experiments, Progress in Energy and Combustion Science 33 (2007) 211–231.

[52] A. North, Experimental Investigations of Partially Premixed Hydrogen Combustion in Gas Turbine Environments, Ph.D. thesis, UC Berkeley, 2013.

[53] B. E. Launder, D. B. Spalding, The numerical computation of turbulent flows, Computer methods in applied mechanics and engineering 3 (2) (1974) 269–289.

[54] L. F. Richardson, Atmospheric diffusion shown on a distance-neighbour graph, Proceedings of the Royal Society of London. Series A, Containing Papers of a Mathematical and Physical Character 110 (756) (1926) 709–737.

[55] A. N. Kolmogorov, The local structure of turbulence in incompressible viscous fluid for very large reynolds numbers, in: Dokl. Akad. Nauk SSSR, Vol. 30, 1941, pp. 299–303.

[56] H. Tennekes, J. L. Lumley, A First Course in Turbulence, MIT press, 1972.

[57] R. Bilger, The structure of turbulent nonpremixed flames, Proc. Comb. Inst. 22 (1989) 475–488.

[58] R. Grout, A. Gruber, C. S. Yoo, J. Chen, Direct numerical simulation of flame stabilization downstream of a transverse fuel jet in cross-flow, Proceedings of the Combustion Institute 33 (1) (2011) 1629–1637.

Article III

Fredrik Grøvdal, Christoph Meraner, Sigurd Sannan, Tian Li and Terese Løvås

Dimensional Decomposition of Turbulent Reacting flows.

Dimensional Decomposition of Turbulent Reacting flows

Fredrik Grøvdal[a,*], Christoph Meraner[a], Sigurd Sannan[b], Tian Li[a], Terese Løvås[a]

[a] *NTNU, Department of Energy and Process Engineering, NO-7034 Trondheim, Norway*
[b] *SINTEF Energy Research, NO-7465 Trondheim, Norway*

Abstract

A dimensional-decomposition approach, decomposing 3D into 3×1D for turbulent (reacting) flows are motivated, discussed and investigated. Three orthogonally intersecting arrays of 1D domains are coupled to capture the the 3D characteristics of fluid flows. The currently used re-couplings for the dimensional-decomposition approach are challenged and enlightened. A thorough investigation based on a flame front in a freely propagating laminar premixed flame is conducted, concluding that the flame stabilizes at the upstream face of the initial solution when both the advectional and auxiliary re-couplings are activated. Furthermore, results from the Three Dimensional Linear Eddy (LEM3D) simulations of a vitiated co-flow burner are re-visited adding a more detailed discussion of the model artifacts. The main conclusion of the present work is that the auxiliary coupling can introduce a significant amount of artificial diffusion. A suggestion for future work is given based on the Péclet number.

Keywords: Turbulent mixing, Linear Eddy Model, Dimensional-Decomposition, Flame stabilization, Péclet number, 3×1D solver

1. Introduction

The key limitation in simulations of turbulent reacting flows is the computation cost. Ideally the whole range of spatial and temporal scales should be resolved and captured. The computational cost is due to solving a combination of fundamental equations involving turbulent fluid flow, heat transfer, chemical reaction, radiative heat transfer and other complicated physical and chemical processes. A number of methods for turbulent mixing and reaction have been developed and investigated in order to meet the required physical description within the computational resources available. One among these is the dimensional-decomposition approach presented by Kerstein [1], where it was proposed to decompose a three dimensional flow into one dimensional domains and recouple them to describe the physical processes. The idea behind this is to obtain a fully resolved spatial and temporal resolution at reduced cost. In the original work, a line segment was defined to correspond to an edge of

a linear stack of cubic control volumes. This idea, however was later modified for numerical implementation since it is preferable to interpret the one-dimensional model evolution as occupying a volume of space, enabling a finite-volume numerical representation, rather than the more conceptual understanding of a line segment.

Such an approach, a 3×1D "DNS", would have the clear advantage of a much lower computational cost in comparison with traditional Direct Numerical Simulations (DNS). The cost reduction is a consequence of requiring fewer computational cells, solving down to the smallest resolution, either the Kolmogorov or the Batchelor scale, in one spatial direction only. DNS in quotes is used as neither 2D DNS nor 1D DNS are in principle able to resolve all turbulent scales. Figure 1 illustrates the number of computational cells for the dimensional-decomposition approach (3×1D) and traditional DNS for Reynolds numbers of 10^4 and 10^5.

In turbulent reactive flows, one-dimensional "DNS" has no perception of turbulent mixing. The Linear Eddy Model (LEM) [2, 3] and the One Dimensional Turbulence Model (ODT), are one-dimensional models where turbulent eddies are rep-
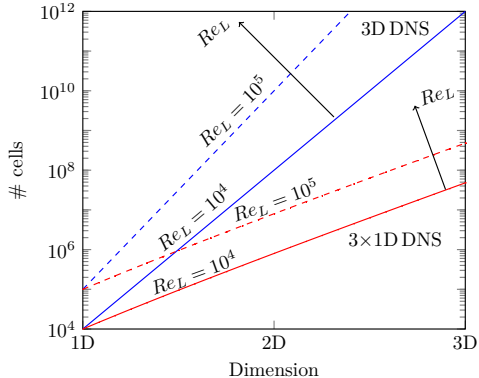

Figure 1: Number of computational cells in traditional DNS versus the number of computational cells needed with the dimensional-decomposition approach.

resented through a special measure-preserving map called the triplet map. The discrete implementation of the triplet map is a permutation of fluid elements, also named wafers. Hence, LEM/ODT is a natural choice for the dimensional-decomposition strategy. Several models have been developed based on the dimensional-decomposition strategy and constitutes a three-array structure of LEM/ODT domains, e.g. ODTLES [4], the Three Dimensional Linear Eddy model (LEM3D) [5, 6] and Lattice-Based Multiscale Simulation (LBMS) [7]. The focus in recent years has for this strategy been on the coupling of arrays of ODT/LEM domains, so as to obtain a self-contained 3D flow simulation (with the smallest scales resolved in each 1D-domain).

Decomposition for the dimensional-decomposition approach is described in e.g. [5], but the re-coupling needs to be treated with caution. In ODTLES, the re-coupling is done by two-way coupling through an average, while LBMS relies on the advection coupling illustrated in Figure 2. LEM3D is formulated with the same advection coupling as LBMS (Figure 2), in addition to an auxiliary coupling, see Figure 3. The novel LBMS model may sufficiently describe flows where the flow is non-uniform in the three directions, however, in the simple case of molecules A, B and C, with similar specific volume and density, flowing through the domain with equal velocity/mass-flux, LBMS will not observe mixing without the auxiliary coupling implemented into LEM3D, see eg. [6, 8]. This is a direct consequence

of the decoupling assumption.

A recent study addressing issues with the decoupling assumption for LEM3D [9] revealed some weaknesses of the dimensional-decomposition approach; specifically the over estimation of diffusion in areas strongly dominated by one direction, e.g. in regions near the nozzle exit of a turbulent reactive jet. This article aims to clarify the artifacts previously revealed and propose a strategy for compensating for these. Even though the previous studies of turbulent flames [8, 9] using LEM3D dealt with a quite complex flow situations, e.g. Berkeley's vitiated co-flow burner [10], we consider a simple flow configurations for demonstration purposes.

The paper is organized as follows. Section 2 gives a brief introduction to the LEM3D model, describing the re-coupling mechanisms in detail, Section 3 establishes the two flow configurations considered here; a numerical setup based on a freely propagating flame and one near field of a jet-nozzle, exemplified through the vitiated co-flow burner [10]. The results and a discussion of these are contained in Section 4, while Section 5 contains the conclusion and Section 4.3 points to future work.

2. The LEM3D Model

The LEM3D model has been described in previous work, see e.g. Sannan et al. [6] and Weydahl [5], and only the one-dimensional re-coupling is described here. LEM3D relies on the general Favre-averaged transport equations for turbulent flows and the structure of the 1D LEM [3]. The Linear Eddy Model includes a turbulent advection term for the triplet maps, describing the Reynold-fluxes, $TM_j = \partial(\widetilde{\overline{\rho u_j'' \phi''}})/\partial x_\alpha$, i.e.

$$\frac{\partial \rho \phi}{\partial t} + \frac{\partial \overline{\rho u_\alpha} \phi}{\partial x_\alpha} = \frac{\partial}{\partial x_j}\left[\rho D_M \frac{\partial \phi}{\partial x_j}\right] + TM_j + \rho \omega_\phi, \tag{1}$$

where $\partial/\partial x_j\left[\rho D_M \partial\phi/\partial x_j\right]$ is the molecular diffusion, $\rho\omega_\phi$ is the source term, and the index j indicates that the terms are implemented on 1D LEM domains in three directions. The average advection process $\partial \overline{\rho u_\alpha}\phi/\partial x_\alpha$ is governed by a velocity and mean density field $\overline{\rho}$ which is prescribed to the mixing model. Note that the conventional summation over the repeated index j is not implied for the right-hand side term.
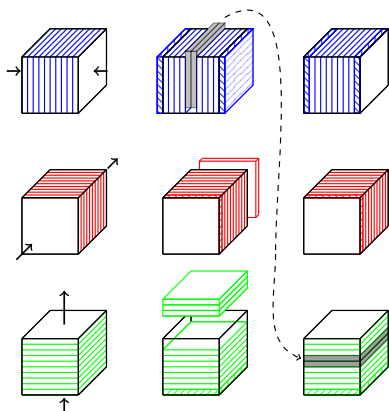
2

Figure 2: Illustration of the advective coupling. The blue, red and green cubes illustrate the three spatial directions, while the arrows indicates the fluxes into/out of the cubic control volumes (3DCVs). In the current example, a single wafer is advected into the 3DCV from each side of the blue-domain direction, a single wafer is advected into and out of the red domain direction, while a single wafer is advected into the green-domain direction and three are advected out. The middlemost three figures illustrate the need of advectional-flipping, where the green-domain lack two wafers, while the blue-domain have two in excess. These two are extracted from the center of the blue-domain, flipped and inserted directly downstream (based on the net green-directional flux) of the center of the 3DCV.

2.1. Re-coupling

The re-coupling processes are associated with the advective time step Δt and consists of two operations:

1. Advective coupling provided by the term $\partial(\overline{\rho u_\alpha}\phi)/\partial x_\alpha$ of Equation (1). The displacement of LEM wafers are based upon the prescribed mass-fluxes $\overline{\rho u}$, while accounting for dilatations from reactions due to the source term $\rho \omega_\phi$. Typically, this involves transfers of wafers among the differently oriented LEM domains intersecting each 3DCV. Conservation of volume is enforced by requiring the displacements of wafers into and out of each 3DCV to obey the equation

$$\sum_{l=1}^{N_{\text{faces}}} \delta_l = 0, \qquad (2)$$

where δ_l denotes the integer number of wafer displacements across the 3DCV faces. A 3D

illustration of the advection operation is shown in Figure 2.

2. An auxiliary coupling is implemented by stochastic rotations of the 3DCVs. The rotations give additional fluid exchanges between the LEM domains, and ensure that physical processes are consistently represented in all spatial directions. The rotation process is illustrated in Figure 3. Thus, for every advective time step Δt, the 3DCVs are rotated $\pm 90°$ about any of the three coordinate axes with a locally defined probability

$$p_{\text{rot}} = \frac{3}{2} C_{\text{rot}} \cdot \text{CFL}_{\text{3DCV}}, \qquad (3)$$

where CFL_{3DCV} is the local Courant-Friedrichs-Lewy number, and C_{rot} is a model constant. Since the rotations introduce diffusive transport, the induced diffusivity D_T^{rot} is deducted from the turbulent diffusivity D_T. D_T is prescribed experiments or calculated from the k-ε turbulence model by $C_\mu k^2/\sigma_T \varepsilon$, where $C_\mu = 0.09$ and σ_T is the turbulent Schmidt number. The effective triplet map diffusivity D_T^{TM} is then given by

$$D_T^{TM} = D_T - D_T^{\text{rot}} \qquad (4)$$

and used as input to the temporal distribution f_t of the triplet maps setting the average number of events per interval[5].

Due to the increase of volume through heat release from reactions, following the ideal gas law for constant pressure, there is an associated deviation Ξ_{flux} for each 3DCV between the prescribed mass-fluxes and the actual mass fluxed by LEM3D given by

$$\Xi_{\text{flux}} = \sum_{l=1}^{N_{\text{faces}}} \left(\Delta x_w \sum_{j=1}^{N_l} \rho_{lj} - \overline{\rho u}_l \Delta t \right), \qquad (5)$$

where N_l is the number of wafers fluxed over face l, and ρ_{lj} denotes the density of the wafer j fluxed into or out of the 3DCV at face l. The given deviation is an integral part of the current implementation in the variable density framework and in the presence of chemical reactions. This deviation was not present in previous formulations of the model [6] due to the assumption of constant density.
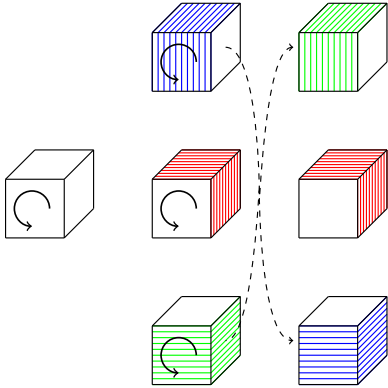
3

Figure 3: Auxiliary coupling between LEM domains illustrated by the rotation from blue domains to green domains. As seen the red domain is not affected by this particular rotation

In order to adapt the deviation Ξ_{flux} into the algorithm, an investigation of various iteration procedures, in combination with least-squares methods to minimize the deviations at each 3DCV cell face, was performed and presented in Grøvdal et al. [9].

2.2. The factor 3

In order to incorporate real physics properly in dimensional-decomposition models, the implemented flow components prescribed to the mixing model is multiplied by a factor 3 to compensate for the fact that the LEM wafers on average spend only one third of the time in any one of the coordinate directions [6].

3. Numerical Setup

This section describes the numerical setup for the required input to the model under investigation. For both the in-house LEM3D code and the commercially available LOGEresearch$^{(\text{TM})}$ code [11], the chemical reaction mechanism employed is the detailed H_2/O_2 mechanism of Li et al. [12].

3.1. Freely propagating flame

A simple laminar freely propagating flame is set up by use of LOGEresearch$^{(\text{TM})}$ with initial conditions given in Table 1. The resulting velocity is also found in Table 1. The velocity and mass-flux is prescribed to the in-house LEM3D code together with species profiles for initialization. All turbulent

parameters in LEM3D are set to zero as the flow is laminar.

Table 1: Flow boundary conditions for the freely propagating flame.

Boundary conditions for Laminar freely propagating flame	
Temperature [K]	300
Velocity [m/s]	2.265
Density [kg/m^3]	0.8495
Mass fraction, H_2	0.296
Mass fraction, O_2	0.148
Mass fraction, N_2	0.556

3.2. Vitiated Co-flow Burner

The vitiated co-flow burner used for validation in the present study, developed at UC Berkeley by Cabra et al. [10], is a lifted turbulent H_2/N_2 jet flame with a coaxial flow of hot combustion products from lean premixed H_2/Air flames. The coflow flames are stabilized on a perforated disk with 87% blockage and an outer diameter of 210 mm. The central jet exit diameter is 4.57 mm and extends 70 mm above the surface of the perforated disk.

The burner was simulated in a previously presented study for various LEM3D-configurations [9]. The input parameters for the required RANS simulation, which prescribes input to LEM3D, is given in e.g. [10, 13]. The RANS simulation was conducted with the modified k-ε model using the academic ANSYS Fluent package. A full description of the set-up can be found in [9].

4. Results and Discussion

4.1. Freely propagating flame

As validation of the chemical-diffusive implementation in the code, a simulation without any recouplings was conducted, looking at a single LEM-domain oriented in the flow direction. It should be noted that since the investigated flow is laminar, a key feature of the Linear Eddy Model, namely the triplet map, is disabled for this study. The flame position of a freely propagating premixed laminar flame is determined by the initialization alone if the inlet velocity is equal to the laminar flame speed. LEM3D is normally initialized using results from a preceding RANS simulation. Hence, the initialization is implemented on the coarse control volume level. With the LOGEresearch$^{(\text{TM})}$ simulation tool the solution for the simple freely propagating
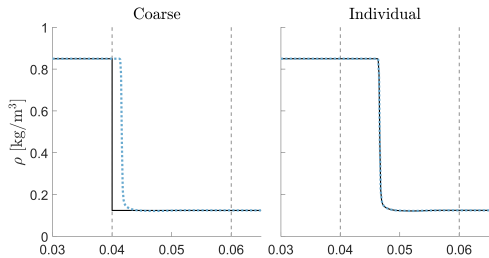
4

Figure 4: Freely propagating laminar flame position for two different initializations. The dashed light gray line indicates the control volume boundaries, while the black and blue dotted lines show the given initialization and the LEM3D solution, respectively. For the left plot the initialization is based on the coarse control volume, while for the right plot the initialization is based on a fine-scale solution from a LOGEresearch$^{(TM)}$ simulation of the laminar freely propagating flame.

flame can be obtained on a finer scale, and thus it is also possible to initialize LEM3D on the wafer level. Figure 4 shows the flame location for the two different initialization procedures. Each sub-plot is given with three different line-types; dashed light gray representing the control volume boundaries, and black and blue dotted showing the given initialization and the LEM3D solution, respectively. For the left sub-plot, the wafers are initialized on the control volume level, i.e. by a step function plotted as a black line. In this case, since the gradients are too sharp for an immediate stabilization, the flame is transported downstream a bit as the preheat zone is building up and reaches steady state once this zone is established. To the right, the wafers are initialized on the wafer level from the solution of a LOGEresearch$^{(TM)}$ simulation. The LEM3D profile now stabilizes, as expected, at the prescribed flame-front since both LEM3D and LOGEresearch$^{(TM)}$ account for the same physical initial conditions, chemical mechanism, and transport equations.

In addition, four simulations using both the re-couplings of LEM3D are conducted. The set-up for these are given in Table 2, where Δx denotes the size of the control volume and N_i the number of control volumes in the streamwise direction (denoted the I-direction). The simulation denoted Coarse refers to the use of coarse 3DCVs, step initialization, and the computational domain is given by the interval [0.020, 0.100] m. The second simulation, denoted Shifted, makes use of the same Δx and initialization as Coarse, but the domain is shifted 0.005 m downstream. This is

done to investigate the effect on the flame front location with respect to cell faces. The third simulation, denoted Individual, is similar to Coarse with respect to Δx and the domain, but here the wafers are initialized individually from the results given by the LOGEresearch$^{(TM)}$. Finally, the fourth simulation, denoted Fine, makes use of the same initialization and domain as Coarse, but the 3DCVs are refined 20 times. The wafer size Δx_w is kept constant for all four simulations, with 640 wafers in the computational domain, and 160 wafers within each 3DCV for the Coarse, Shifted, and Individual simulation, respectively, and 8 wafers for the Fine simulation, respectively.

Table 2: Simulation cases where either both LEM3D re-couplings (results shown in Figure 5) are used or just the advective coupling is used (results in Figure 6).

Case	Initialization	N_i	Δx [m]	Domain [m]
Coarse	Step	4	0.02	[0.020,0.100]
Shifted	Step	4	0.02	[0.025,0.105]
Individual	Wafer	4	0.02	[0.020,0.100]
Fine	Step	80	0.001	[0.020,0.100]

Figure 5 shows the initialized solution (black line) and the time-averaged LEM3D solution (dashed blue line) for each of the cases given in Table 2. The control volume boundaries are indicated by dashed light gray lines. The time-average is taken over a period of 5 sec after an initial relaxation time. We observe that the flame stabilizes close to the cell face of initialization for all four cases of Figure 5, and that there are some ripples downstream of the flame front for the time-averaged profiles. The stabilization of the flame front is due to the rotations being the dominating re-coupling mechanism between the I-oriented domain (streamwise direction), and the J- and K-oriented domains (lateral directions), in some cases shifting the flame front all the way to the cell faces. In the event that the flame front is rotated to the downstream cell face, however, unburned mixtures are moved to the upstream face. This creates unphysical gradients and pockets within the reaction zone, leading to the ripples seen in all the sub-plots. This is most clearly seen in the right-most sub-plot of Figure 5, as the plotted range here is smaller. The described effect could be beneficial in corrugated flames with pockets, but only if the rotations were introduced to act as some sort of turbulent mixing. But then there would be no
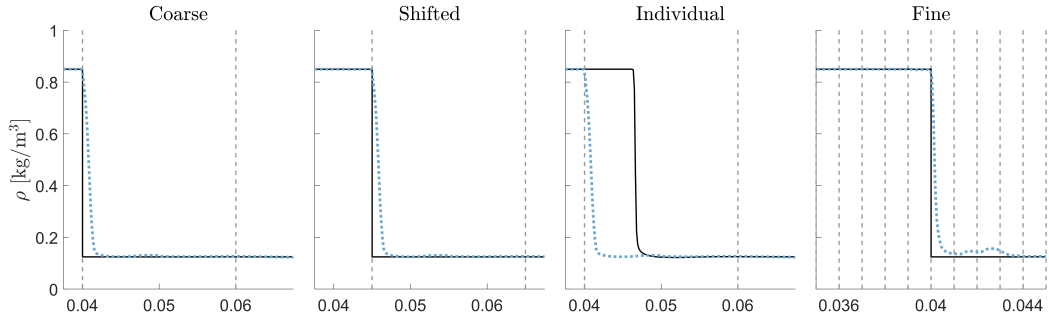
5

Figure 5: Time-averaged profiles of LEM3D with both the advective and the auxiliary coupling for the four cases of Table 2. The black and blue dotted lines show the given initialization and the LEM3D solution, respectively, while the dashed light gray line indicates the control volume boundaries. The course mesh contains 160 wafers and has a control volume width of $\Delta x = 0.02$ m, while the fine mesh control volume has a width of $\Delta x = 0.001$ m and contains 8 wafers.

rotations in the laminar case, since there is no turbulence. No rotations would lead to a less coupled solution, and result in no mixing in the simple case of molecules A, B and C, with similar specific volume and density, flowing through the domain with equal velocity/mass-flux, see eg. [6, 8]. As the rotations are intended only as a re-coupling of the domains and not to represent turbulence, these should ideally not create pockets. Within the framework of the model, pockets should result only from the triplet maps, which are non-present in the laminar case.

From the Coarse and Individual case simulation plots of Figure 5, we conclude that the flame front is independent of the initialization process. Based on all four sub-plots, we also observe that the flame stabilizes within the control volume where the flame front is initialized and close to the upstream face of that volume. Thus we deduce that no further information is gained from the dimensional-decomposition approach compared to a RANS simulation where the flame front is fully contained within one control volume for a laminar freely propagating flame.

Finally, we investigate the effect of the LEM3D advective coupling by flipping of wafers only, thereby switching off the auxiliary coupling by rotations. For this, four additional simulations are performed with set-ups as given for the cases of Table 2. Figure 6 shows the results of the LEM3D simulations without the rotational coupling. The additional red line of the sub-plots, compared to Figure 5, shows the instantaneous density profiles of the simulations. First of all, we observe that for

all four simulations the flame is shifted to its closest control-volume center, based on the initialization. Second, it is clear by the four sub-plots that the instantaneous profiles contain fluctuations in the form of spikes within the flame front, in comparison to the mean profile (dashed blue line). These spikes result from the instantaneous flipping of wafers where these are inserted into the middle of the flame location, splitting the flame front. As the progress variable from the J- and K-oriented domains will vary, the instantaneous profiles also vary when different values of the progress variable is flipped to the I-oriented domain. Finally, we observe that there is no difference in the result for the two initialization procedures within a control volume. Hence, LMBS and LEM3D will for laminar freely propagating flames neither provide nor lose any additional information by the dimensional-decomposition approach since the main feature, namely the triplet map, is disabled.

As an example of the ongoing processes in LEM3D, the instantaneous wafers for all three orientations in the flame-front control volume are shown in Figure 7 for three sequential advective time steps. Note that the K-oriented domain is supposed to be oriented perpendicular to the document plane, however, the wafers are here arranged in the same direction as the J-domain for illustration purposes since they both are lateral. The flame-front is located in the I-oriented domain as this is the flow direction. Note that physically this is a one-dimensional flow. Hence, the J- and K-domains have no physical interpretation. In between t and $t + \Delta t$, the wafers progress towards
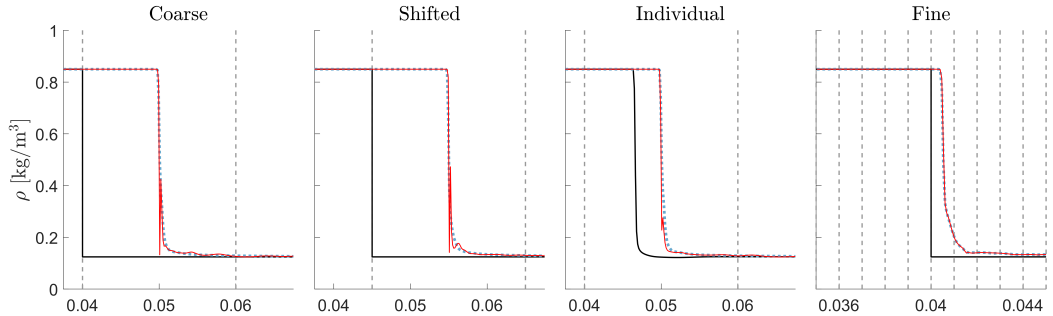
Figure 6: LEM3D without the auxiliary coupling, i.e., the LMBS model, simulated for the four cases in Table 2. Each sub-plot is given with four different line-types; dashed light gray, black red and blue dotted, describing the control volume boundaries, the given initialization, the LEM3D instantaneous simulation, and the LEM3D time-averaged solution, respectively. The course mesh contains 160 wafers and has a control volume with width $\Delta x = 0.02$ m, while the fine mesh control volume has a width of $\Delta x = 0.001$ m and contains 8 wafers.
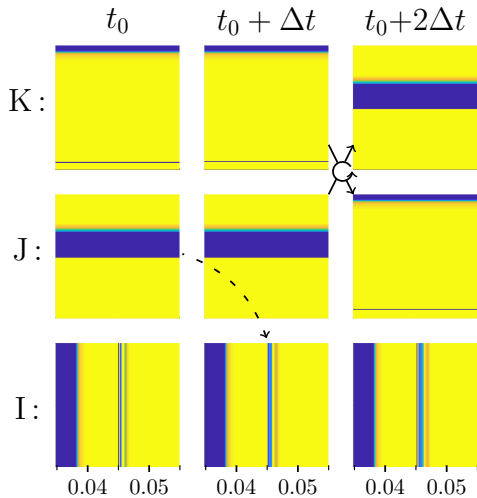

Figure 7: The rotation and flipping process demonstrated for the freely propagating flame configuration, plotting individual wafer values, ranging from blue (unburned) to yellow (fully combusted). At t_0 we see the instantaneous solution for the three different orientations within the control volume that contains the flame front. At $t_0 + \Delta t$, some of the wafers in the I-direction has reacted and the advectional flipping inserts an unreacted wafer from the center of direction J into the center of direction I. At $t_0 + 2\Delta t$, the J-oriented wafers are rotated into the K-direction and oppositely, the K-directional wafers are rotated into the J-direction.

fully combusted and gradients are smeared out by molecular diffusion. At $t + \Delta t$, some wafers are flipped from the center of the J-oriented domain into the I-oriented domain, right upstream of the center-point within the control volume. This advective flipping is illustrated by the dashed arrow in the figure and due to expanding products, this operation presses unburned gas out in the other directions and into the I-oriented domain. Again, in between $t + \Delta t$ and $t + 2\Delta t$, the wafers react and diffuse. At $t+2\Delta t$, the wafers oriented in the J- and K- direction are by the auxiliary coupling swapping orientation/domains. This process is illustrated by the two-arrow-cycle in between $t_0 + \Delta t$, $t_0 + 2\Delta t$, the J- and K-oriented domains. As adjacent control volumes are not shown in Figure 7, the effect of the rotation creating new and sharp gradients at the cell faces, are strictly speaking not highlighted in this illustration. One may imagine, however, that the wafers from either of the domains are rotated into the I-oriented domain with fully burnt wafers upstream and unburned wafers downstream. This would clearly create a sharp gradient stabilizing the flame at the cell face.

It is clear from the results presented in this sub-section that the flame position does not move out of the control volume where it is initialized for the freely propagating flame set-up. As observed, this depends on the re-coupling mechanisms at use, i.e., that the flame position stabilizes either at the center of the control-volume, or at the face or close to the face. The face stabilization of the flame is due to the strong effect of the rotations from the auxiliary coupling. When the auxiliary coupling is switched

7

off, however, the flame stabilizes in the center of the control volume as a consequence of the tripled mass within the control-volume, where the lack of mass-flux is taken into the center of the I-oriented domain from the J- and K-oriented domains. This solution also tends to fluctuate, as the number of wafers flipped from the other co-oriented domains alternates and vary in the value of the progress variable. These fluctuations, however, are shown to decrease with the wafer size as a more constant number of wafers are flipped into the center of the I-oriented domain.

4.2. Vitiated Co-flow burner

The LEM3D simulations have been conducted by Grøvdal et al. and are presented in [9]. The results are not re-printed here. However, a more detailed discussion is added, focusing on the effect of the auxiliary coupling on the flow field, especially on the region close to the nozzle.

The past study concluded that LEM3D showed good agreement with experimental data by Cabra et al. [10] in the far field, but that the current implementation did not yield a lift-off height in accordance with the experiments. The proposed reason in this regard was that the rotations caused an increased spread of H_2 in the near-field. However, this hypothesis was not validated by a thorough analysis of the near field scalar fields. This section aims to fill that gap.

The results presented in this section gives temperature profiles only. This is for simplicity, as it represents both mixing and reaction, in comparison to the mixture fraction which only reflects the mixing. The reader is kindly asked to recall that the vitiated co-flow burner has separate fuel and oxidizer inflows, so when the temperature varies in the range of 300-800 K roughly, the physical effect is often mixing and not reaction.

The jet inlet is approximated by a single cell, where the area of the jet is preserved, i.e., $(\Delta x)^2 = \pi(d/2)^2$, where d is the jet diameter and $\Delta x = 4.05 \cdot 10^{-3}$m is the mesh size. Figure 8 presents a cropped version of the LEM3D cube mesh, with the gray area denoting the jet nozzle inlet. The thick orange and blue lines are the LEM domains which will be displayed as radial profiles in Figure 9. The I-oriented domains are perpendicular to the document, intersecting the blue and orange lines at the control volume center, i.e. black dots, and hence no visualization is possible. In Figure 9 the I-oriented scalars will be given the color of
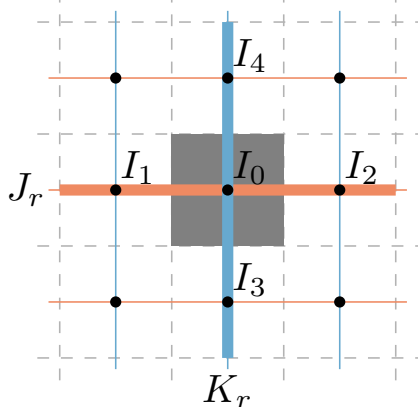

Figure 8: The figure illustrates the control volumes for which the species scalar profiles will be plotted in the next figure. The jet nozzle is represented by a single control volume, located in the gray middle control volume and the dashed light gray describing the control volume boundaries. Further, the orange and blue domain denotes the J- and K-oriented LEM-domains, respectively, and the black dots the control volume center, where the axial I-domain be oriented perpendicular to the document plane.

the thickly-colored-domain it is intersecting, as it in the jet-control-volume (center-control-volume) will be intersecting both the thickly-colored-domains it is given their average color. Hence, the I-oriented domains not intersected by a thick line (blue or orange) will not be presented in Figure 9.

In Figure 9, instantaneous temperature profiles are plotted for the control volumes and domains as described in relation with Figure 8. The black lines denote, as in Subsection 4.1, the initial profile, here prescribed from the ANSYS Fluent simulation. The bottom, long, plot gives the radial profiles for the J- and K-oriented LEM-domains for, $r/\Delta x \in [-1.5, 1.5]$. The sub-plots at the top of Figure 9 illustrate the I-directional (axial) LEM domain for $z/\Delta x \in [0, 1]$, these are rotated for easier understanding of the three domains. There are unphysical large gradients in the radial plots outside the jet nozzle (central) control volume. Hence, the gradients are created already in the first control volumes downstream of the co-flow inlet, where it should be none or small gradients. Furthermore, we also note that the temperature is significantly higher than the mean in parts of the domains adjacent to the jet-exit domain. This was also pointed out in the discussion of axial scatter-plots presented
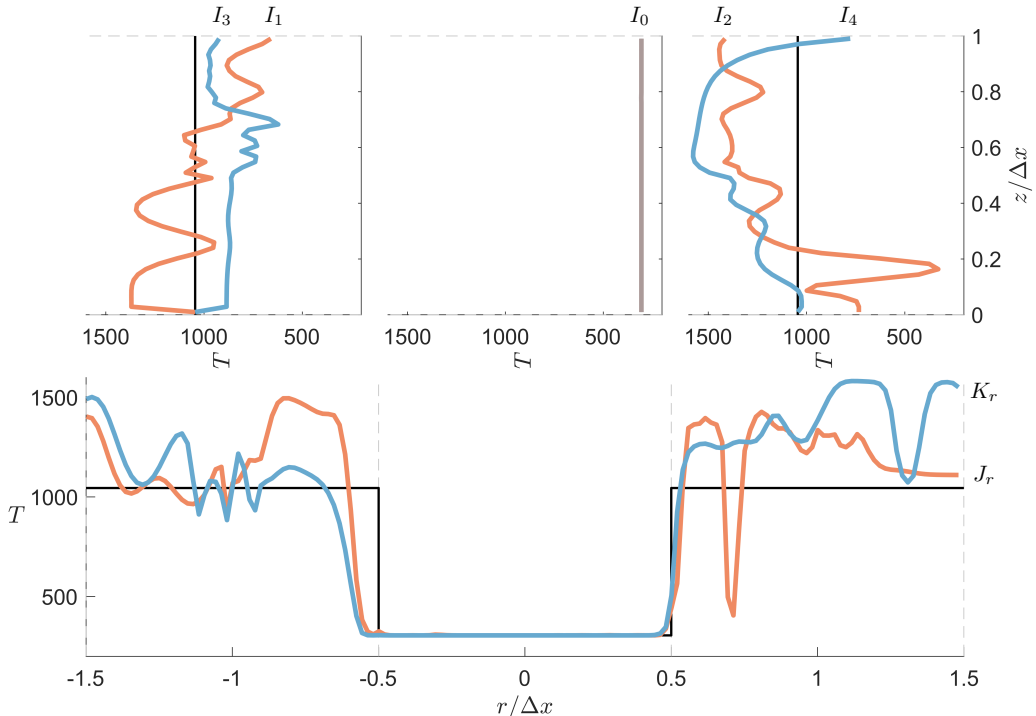
Figure 9: Instantaneous species profiles plotted for the three coordinate directions in the first layer of LEM3D control volumes (3DCVs) downstream of the jet exit for the vitiated co-flow burner. The domains are colored as illustrated in Figure 8 and explained in the text; the orange and blue lines in the bottom sub-plot denotes the J- and K-oriented LEM-domains, respectively. However, in the top three sub-plots the blue and orange color describe if the axial I-domain is plotted for a 3DCV where also a J-(orange) or K-oriented (blue) domain is plotted in the bottom sub-plot. As both the J- and K-domain are plotted for the central 3DCV, the control volume of the jet exit, the displayed color is the average RGB color of the orange and blue one. Therefore only one line is displayed.

in [9]. The discussion of these unphysical high gradients is based on a conceptual sketch in Figure 10 for the purpose of clarity and better understanding. This allows to filter a single group of wafers and to look at different mass transport phenomenas sequentially, even though they happen simultaneously. The conceptual sketches are based on transient results seen while analyzing transient scalar profiles, not included in this paper.

A conceptual illustration of the creation of gradients seen in Figure 9 is presented in Figure 10. Only the solution for wafers that are initially oriented in J-direction is shown, to simplify the illustration. The initial solution, prescribed from RANS, is shown in the top left (long) figure. To simplify the illustration further, we restrict our in-

terest to the area within the red box. Strictly speaking, only the control volume of which is fully contained in the red box is of interest but the remaining part contained within the red box is included for simplification when illustrating the radial profiles. Firstly, the area of interest is redrawn and given its own sub-figure, top left. Secondly, molecular diffusion smears out the gradients from the the sharp step-function, prescribed by RANS, resulting in the "smooth" profile in the top-mid figure. Thirdly, seen in the top-right sub-figure, the radial-oriented (J- or K-orientation) domain contained in the control volume, $r/\Delta x \in [0.5, 1.5]$, is rotated by the auxiliary coupling into the axial orientation (I-orientation). As the profile now is oriented in the axial direction, it is affected by the co-flow veloc-
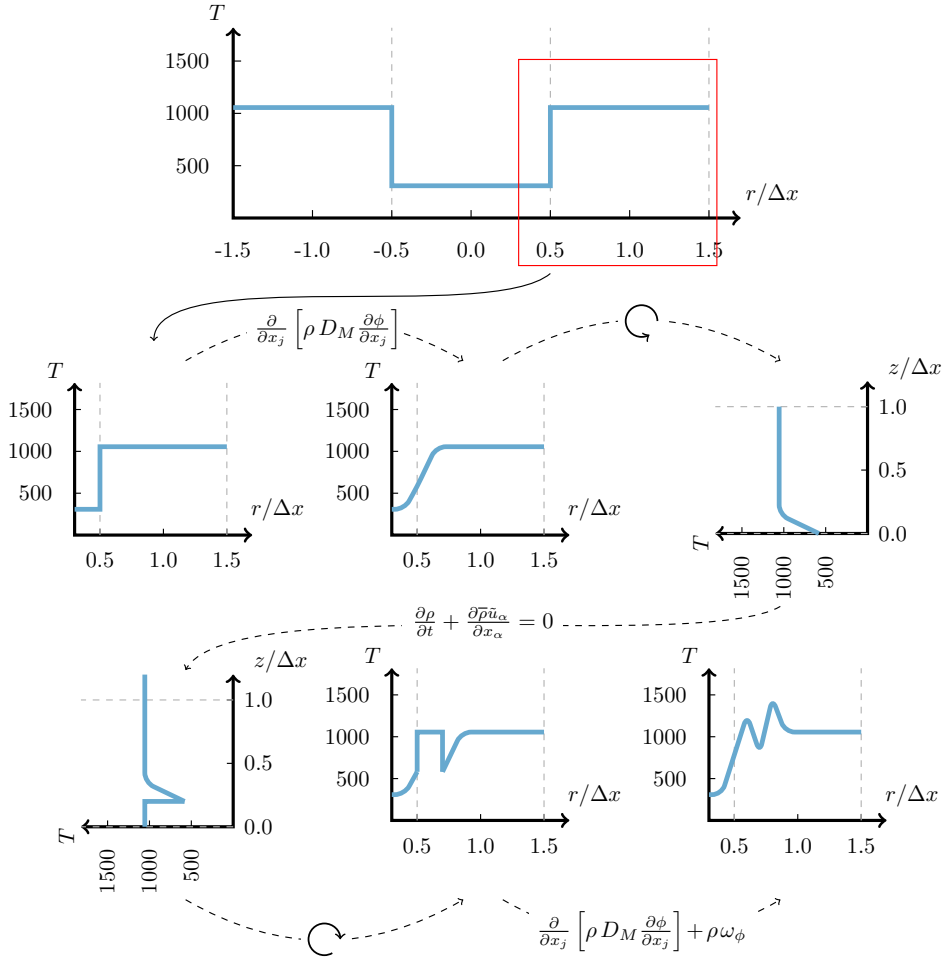
Figure 10: Conceptual illustration describing the creation of the gradients seen in Figure 9 in control volumes adjacent to the jet control volume.

ity, shifting the profile downstream and advecting *fresh* wafers in, seen in the bottom-left sub-figure. Now, illustrated in the bottom-mid sub-figure, the axial-oriented profile is rotated back into the radial-oriented domain (J- or K-orientation). Finally, the profile is affected by both molecular diffusion and reaction, resulting in local temperature maximum above and local minimum below the initial pre-scribed profile, seen in the bottom-right sub-figure.

As the above figure and description is conceptual, the actual simulations tend to deviate slightly from the above, e.g. by the diffusion and reacting rates being continuous processes, rather than the alter-nating/instantaneous one presented. The fact that the profile might not directly rotate back into the same direction (it might actually be mirrored into the old direction) or the fact that rotations are set to happen based on the local Courant-Friedrichs-Lewy condition, results in frequent rotations down-stream of the jet-nozzle and a more stable profile in the central control volume of the inflow temper-ature, as seen in Figure 9.

The artifacts from the re-coupling processes for the dimensional-decomposition approach seem to need special treatment depending on the physical conditions of the flow and different regions within the same flow would require different treatment. It is evident that such a treatment will require a great amount of effort in order to make it give reasonable results for generally complicated turbulent reacting flows, which would not be satisfactory for the purpose of formulating a multi-regime model. A possible solution to the above challenge connected to the auxiliary coupling of the dimensional-decomposition approach is to base it on matching the Péclet number, in the manner as suggested below.

In the freely propagating flame configuration the diffusion and chemistry implementation in the code was validated. Further, it was concluded in Subsection 4.2, that the total diffusion is too large already directly downstream of the jet nozzle. Diffusion requires two physical aspects, gradients and diffusive flux, and consequently, in order to reduce the total diffusion we need to reduce either of the two. As the molecular (and thermal) diffusivity is validated, they are not the cause of the observed enhancement in the diffusivity. The reason, however, results from the auxiliary coupling which constantly creates sharp gradients at the control volume faces, strongly enhancing the overall diffusion. In order to mitigate this issue, there exists two options; either reduce the gradients or reduce the molecular (and thermal) diffusivity. Of these two options, only the reduction of gradients would comply with solving chemistry directly by, e.g. CHEMKIN II. However, given that the gradients cannot be avoided by [5, 6], a correction term of the overall diffusion fluxes might be considered; adjusting the overall diffusion flux to be bounded to the RANS solution compensating for the model artifact of rotations.

The Péclet number (Pe) is defined to be the ratio of the rate of advection of a physical quantity by the flow to the rate of diffusion of the same quantity driven by an appropriate gradient:

$$\text{Pe} = \frac{\text{advective transport rate}}{\text{diffusive transport rate}} \qquad (6)$$

In the context of species or mass transfer, the Péclet number is the product of the Reynolds number and the Schmidt number, i.e. $\text{Pe}_D = Lu/D = \text{Re}_L\text{Sc}$, where D is the mass diffusion coefficient, L

the characteristic length and u the local flow velocity. In the context of the thermal fluids, the thermal Péclet number is equivalent to the product of the Reynolds number and the Prandtl number, i.e. $\text{Pe}_T = Lu/\alpha = \text{Re}_L\text{Pr}$, where α is the thermal diffusivity [14].

It should be noted that a reduction of the rotation frequency would not make a strong effect, as the consequence for each rotation would just be larger and the coupling between the directions weaker. In high turbulence regions, the Pe number is large since the advective transport is large compared to the diffusive transport. Hence, overprediction of molecular diffusion will not critically affect Pe. In these regions the overall gradients are reduced through subtracting the introduced diffusivity by rotations, D_T^{rot}, from the turbulent diffusivity, D_T. Hence the artificially introduced gradients take energy from turbulent mixing and might be considered as eddies of size Δx.

If the overall diffusion flux is to be bounded to either experiments or CFD, the Pe number needs to be prescribed together with other flow characteristics. Two alternative implementations of bounding the overall diffusion flux, i.e. matching the Pe number is transient optimization of a local-reduction factor, $f_{\text{Pe}} \in [0, 1]$ or by setting the factor f_{Pe} a priori based on local (mass-)flux-fractions. Such an approach would have certain similarities to adjustments of chemical/molecular timescales in order to keep a non-dimensional group (e.g. Da) within a given range [15].

5. Conclusions

The dimensional-decomposition approach has been investigated in this paper, with a further description of the currently used re-coupling processes, illumination of certain artifacts of the approach and validation of the chemical implementation of LEM3D based on a freely propagating laminar flame. Results from the freely propagating laminar flame is presented in order to analyze flame front stabilization for the model with different recoupling approaches. It is found that the LEM3D model with auxiliary and advectional coupling stabilizes at the cell face upstream of the control volume in which the flame is initialized, independent on control volume size and type of initialization. This is due to the strong effect of the auxiliary coupling. Further, the model for which the auxiliary re-coupling is turned off is investigated. This model

uses the advectional coupling only, still relying on the dimensional-decoupling approach, i.e. either LEM3D or LBMS, and stabilizes (time-averaged solution) in the center of the control volume for which the flame is initialized. It should be noted that the flame-front, however, is slightly unstable due to the wafer flipping. Finally, LEM3D results based on the vitiated co-flow burner are revisited and a detailed analyses is given to explain why the previous simulation stabilized directly downstream of the jet nozzle, i.e. with a low lift-off height. Both results and a conceptual description are given.

Within the LEM3D framework, the mass is tripled through the dimensional-decomposition approach, leading to the factor 3 on advection fluxes in order to keep a constant residence time within each control volume. Each LEM domain has the capability of representing species transport in one direction only, making re-coupling a necessity. To re-couple the three 1D-domains, making the combination of them represent *3D*, the rotations are introduced as one of the mechanisms, described at the end of Section 1. The artifacts of the rotations are thoroughly discussed and explained in Sub-section 4.2, and it is found that their artifacts for the current implementation is inevitable. Unfortunately, the auxiliary coupling (with rotations) was found a necessity for the LEM3D framework in order to ensure that physical processes are consistently represented in all spatial directions [5, 6]. Thereby, the conclusion reads that the dimensional-decomposition approach is, for the current configuration, unacceptable. However, a proposed solution for the issue is presented and discussed in Sub-section 4.3. It is recommended to be implemented if models relying on the dimensional-decomposition approach are to be further developed, such as LEM3D and LMBS. The exception might however be if frequent averaging is conducted, such as in ODTLES. For this particular model an additional study needs to be performed in order to conclude on the consequences of the dimensional-decomposition approach.

Acknowledgments

Compliance with Ethical Standards

Conflict of interests The authors declare that they have no conflict of interest.

References

[1] A. R. Kerstein, One-dimensional turbulence stochastic simulations of multi-scale dynamics, Lecture Notes in Physics 756 (1-6) (2009) 291–333.

[2] A. R. Kerstein, Linear-eddy modelling of turbulent transport. Part 6. Microstructure of diffusive scalar mixing fields, Journal of Fluid Mechanics 231 (1991) 361–394.

[3] A. R. Kerstein, Linear-eddy modelling of turbulent transport. Part 7. Finite-rate chemistry and multi-stream mixing, Journal of Fluid Mechanics 240 (1992) 289–313.

[4] R. C. Schmidt, A. R. Kerstein, R. McDermott, ODTLES: A multi-scale model for 3D turbulent flow based on one-dimensional turbulence modeling, Computer methods in applied mechanics and engineering 199 (13-16) (2010) 865–880.

[5] T. Weydahl, A Framework for Mixing-Reaction Closure with the Linear Eddy Model, Ph.D. thesis, NTNU Trondheim, 2010.

[6] S. Sannan, T. Weydahl, A. R. Kerstein, Stochastic simulation of scalar mixing capturing unsteadiness and small-scale structure based on mean-flow properties, Flow, Turbulence and Combustion 90 (2013) 189–216.

[7] J. C. Sutherland, A Novel Multi-scale Simulation Strategy for Turbulent Reacting Flows, Final Technical Report - DE-SC0008998, 2012-2017. URL https://www.osti.gov/servlets/purl/1432812

[8] F. Grøvdal, S. Sannan, J.-Y. Chen, A. R. Kerstein, T. Løvås, (in press), Three-dimensional Linear Eddy Modeling of a Turbulent Lifted Hydrogen Jet Flame in a Vitiated Co-flow, Flow, Turbulence and Combustion (2018), DOI: 10.1007/s10494–018–9963–x.

[9] F. Grøvdal, S. Sannan, J.-Y. Chen, T. Løvås, A parametric study of LEM3D based on validation with a Turbulent Lifted Hydrogen Jet Flame in a Vitiated Co-flow, *Manuscript submitted for publication* (04.07.18).

[10] R. Cabra, T. Myhrvold, J. Chen, R. Dibble, A. Karpetis, R. Barlow, Simultaneous laser Raman-Rayleigh-LIF measurements and numerical modeling results of a lifted turbulent H2/N2 jet flame in a coflow, Proceedings of the Combustion Institute 29 (2) (2002) 1881–1888.

[11] Loge AB, LOGEresearch v1.10. LOGEresearch - a combustion and chemical kinetics simulation tool, Lund, Sweden. Available online: http://logesoft.com/loge-software/ (2018).

[12] J. Li, Z. Zhao, A. Kazakov, F. L. Dryer, An updated comprehensive kinetic model of hydrogen combustion, International journal of chemical kinetics 36 (2004) 566–575.

[13] T. Myhrvold, I. Ertesvåg*, I. Gran, R. Cabra, J.-Y. Chen, A numerical investigation of a lifted H2/N2 turbulent jet flame in a vitiated coflow, Combustion science and technology 178 (6) (2006) 1001–1030.

[14] D. Spalding, H. Hottel, S. Bragg, A. Lefebvre, D. Shepherd, A. Scurlock, The art of partial modeling, in: Sym-

posium (International) on Combustion, Vol. 9, Elsevier, 1963, pp. 833–843.

[15] B. Farcy, L. Vervisch, P. Domingo, Large eddy simulation of selective non-catalytic reduction (SNCR): A downsizing procedure for simulating nitric-oxide reduction units, Chemical Engineering Science 139 (2016) 285–303.